UNIVERSITY OF MESSINA

DEPARTMENT OF ENGINEERING

PhD COURSE IN INDUSTRIAL AND INFORMATION ENGINEERING

XXXVIII CYCLE

SSD: IIND-03/A – Progettazione Meccanica e Costruzione di Macchine

GREEN AND LIGHTWEIGHT STRUCTURES PRODUCED BY INNOVATIVE TECHNOLOGIES

PhD candidate:
Daniele Rizzo

Supervisor:
Prof. Gabriella Epasto (IIND-03/A)

Co-supervisor:
Prof. Antonino Squillace (IIND-04/A)

PhD course coordinator:
Prof. Edoardo Proverbio

Academic Year 2024/2025

Abstract

The present PhD thesis investigates the potential of replacing conventional materials used in industrial applications with sustainable and lightweight alternatives, addressing the growing need to reduce environmental impact and improve resource efficiency. The research focuses on advanced materials and innovative technologies, including sandwich structures, bio-based materials, and additive manufacturing, with the aim of evaluating their applicability.

Lightweight design and material sustainability are increasingly critical factors across various sectors, particularly in transport, aerospace, and energy. Composite sandwich structures are widely adopted due to their excellent combination of low density and high mechanical performance. However, end-of-life management remains challenging, as the separation of components and limited recyclability of synthetic matrices hinder sustainable disposal and recovery. To overcome these limitations, this thesis explores sustainable sandwich structures incorporating bio-based polymers or recyclable metal alloys, offering a balance between mechanical performance, reduced weight, and environmental compatibility.

The first part of the research focuses on traditional and hybrid sandwich structures, exploring the use of metal and eco-friendly alternatives. An extensive experimental campaign was carried out to characterise their mechanical behaviour under various loading conditions, including quasi-static indentation and low-velocity impact. The effect of indenter geometry was investigated, and a predictive coefficient, the Dynamic Scaling Factor, was introduced to estimate the material's response to dynamic loading based on simpler and more cost-effective static tests. Comparative analyses were also performed between all-metal aluminium honeycomb structures and conventional materials with equivalent flexural stiffness.

Further investigations focused on hybrid sandwich structures, specifically Flax/AHS and Basalt/AHS configurations. The mechanical response of these structures was evaluated under different loading conditions, and failure mechanisms were systematically assessed using visual inspection, radiography, microscopy, and thermography.

The second part of the research focuses on additive manufacturing techniques, with particular attention to biodegradable polymeric materials such as PLA and foamed PLA. The study investigates the influence of process parameters on foam morphology, bending and impact behaviour, and failure mechanisms. Foam additive manufacturing is highlighted as a promising approach for producing lightweight, recyclable, and environmentally friendly structures, forming a bridge between theoretical investigations and practical applications for sustainable industrial components.

Overall, the results demonstrate that sustainable sandwich structures and PLA-based additive manufactured materials can effectively replace conventional solutions, integrating advanced design, green materials, and modern production technologies. By combining lightweight principles with high mechanical performance and improved end-of-life management, these approaches provide a promising strategy for enhancing industrial sustainability, reducing environmental impact, and supporting circular economy practices across multiple sectors.

Contents

1. Introduction

In recent years, the demand for sustainable and energy-efficient technologies has become increasingly relevant in a wide range of industries. Among the key strategies to meet environmental and regulatory targets, reducing structural weight is particularly effective. Lightweight design not only contributes to fuel savings and reduced operating costs, particularly in the transport sector, but also helps to reduce greenhouse gas emissions and minimise resource consumption.

At the same time, the increasing focus on sustainability drives industries to adopt material-based solutions that consider the full life cycle, from raw material extraction to end-of-life disposal. This trend highlights the need for recyclable, repairable or biobased alternatives to conventional composites. While traditional fibre-reinforced polymer (FRP) materials offer excellent mechanical properties, they still pose challenges in recyclability, multi-material separation, and overall environmental impact.

Additive manufacturing (AM) is emerging as a promising technology for design, manufacturing, and supply chains. Many industries are increasingly exploiting its potential to produce high-performance components through advanced digital manufacturing and greater design freedom. However, in some sectors, AM adoption remains limited due to the lack of standardised design methods, established workflows, and rigid regulations. Despite these limitations, AM offers substantial advantages in material efficiency and customization, making it particularly attractive for the development of lightweight structures and sustainable solutions. Its compatibility with biodegradable and low-impact materials further enhances its role in circular economy strategies, particularly in sectors such as packaging.

These technological and environmental challenges have motivated the development of innovative structural solutions that combine mechanical efficiency, durability, and ecological performance. In this context, aluminium honeycomb sandwich (AHS) structures are promising due to their high strength-to-weight ratio, energy absorption capacity, and recyclability. Nevertheless, their implementation in structural components requires a detailed understanding of dynamic behaviour, failure modes, and integration potential.

This PhD thesis investigates strategies and structural solutions to assess the potential of innovative and sustainable materials for industrial applications, focusing on two main directions:

- development and characterisation of full-metal and hybrid AHS structures for transport applications;
- evaluation of biodegradable polymer-based materials, including PLA and foamed PLA, produced via additive manufacturing for food and packaging applications.

The methodology combines experimental investigation, theoretical evaluation and critical interpretation of results to identify optimal solutions in terms of mechanical performance, sustainability and industrial applicability.

1.1 Objectives

This thesis aims to study and develop lightweight and sustainable structural solutions, focusing on the design, characterisation and improvement of advanced materials and configurations. Specifically, it addresses:

1. Aluminium honeycomb sandwich structures
    - Investigating the mechanical behaviour, damage mechanisms, and dynamic response of AHS under quasi-static perforation and low-velocity impact;

- Evaluating the potential benefits of hybridising AHS with natural fibres (e.g., flax) and mineral fibres (e.g., basalt) to improve performance and failure resistance;
- Developing methodologies and design guidelines, introducing a Dynamic Scaling Factor to predict dynamic behaviour from static test data, supporting efficient and safer design procedures.

2. Biodegradable PLA-based materials via additive manufacturing
   - Assessing the mechanical properties and environmental impact of PLA and foamed PLA, while analysing how process parameters influence foam morphology and performance, with the aim of optimising material properties and expanding potential industrial applications.
3. Comparative and sustainability assessment
   - Comparing the proposed solutions with conventional materials in terms of weight reduction, mechanical efficiency, and sustainability, while performing a comprehensive environmental impact assessment to support sustainable development.

The objectives are pursued through a systematic and multidisciplinary approach, which includes:

- A comprehensive literature review to identify current advances in manufacturing techniques, design strategies and optimisation methods applicable to sandwich structures and additive manufacturing;
- Experimental investigations for characterising the mechanical response and failure modes of the proposed materials and structures. The response of the analysed structures evaluated through quasi-static perforation tests, low-velocity impact tests, and three-point bending tests. The failure modes were assessed using non-destructive testing, specifically visual inspection, thermography, and radiography;

- Critical comparison with conventional materials and structural solutions, highlighting advantages in terms of mechanical performance, weight reduction, and sustainability;
- Assessment of environmental impacts related to the materials and considered processes, providing a comprehensive evaluation to support sustainable development.

This work aims to advance knowledge on innovative lightweight structures, providing both theoretical insight and practical guidance to facilitate their adoption across relevant industries.

1.2 Structure of the thesis

The thesis is organised into seven chapters, structured as follows:

- ***Chapter 1 – Introduction*** provides a brief introduction to the topic and presents the objectives and structure of the thesis.
- ***Chapter 2 – Sustainability, Lightweight Materials and Innovative Technologies*** provide an overview of the state of the art in lightweight and sustainable structural design. It examines how technological innovation, sustainability goals, and regulatory requirements are driving changes in modern mechanical design, focusing on weight reduction and the selection of sustainable materials, particularly in high-impact sectors such as transport. The chapter introduces and classifies composite and sandwich structures, explaining their design principles, mechanical response under bending and impact, and typical failure modes. It also presents a literature review on the applications of full-metal, composite, and hybrid sandwich structures. Furthermore, an introduction to additive manufacturing is provided, highlighting its applications in modern engineering.

- ***Chapter 3 – Quasi-static and impact behaviour of sandwich structures*** deal the investigation on the mechanical performance of aluminium honeycomb sandwich panels compared to conventional composite sandwiches, such as GFRP skins with polymeric or balsa cores. Quasi-static indentation and low-velocity impact tests were carried out to evaluate energy absorption and damage mechanisms under localised loading. The chapter highlights the potential of AHS as lightweight, high-performance, and sustainable alternatives to conventional composites.
- ***Chapter 4 – Mechanical behaviour of hybrid sandwich structures*** provides an analysis of the mechanical performance of aluminium honeycomb panels hybridised with natural fibre skins. Two configurations were considered: panels with flax fibre reinforced skins and panels with basalt fibre reinforced skins. Flexural tests and low-velocity impact experiments were carried out to assess the influence of hybridisation on stiffness, energy absorption, and failure mechanisms. The chapter focuses on the role of different fibre reinforcements in hybrid sandwich panels and their implications for sustainable and high-performance design.
- ***Chapter 5 – Mono-material sandwich structures produced by innovative additive manufacturing process*** focuses on the characterization of biodegradable PLA sandwich panels produced by Foam Additive Manufacturing. The chapter presents the design of PLA specimens with different core configurations and their evaluation under bending and low-velocity impact loading. The chapter focuses on the influence of core morphology and printing parameters on the design of lightweight, sustainable, and high-performance sandwich structures for applications ranging from structural components to eco-friendly packaging.

- ***Chapter 6 – Discussion*** addresses the interpretation of the results from the experimental chapters. It presents comparisons between different sandwich configurations and examines energy absorption behaviour to provide an understanding of the mechanical performance of the investigated specimens under various loading conditions.
- ***Chapter 7 – Conclusions*** summarise the main findings of the thesis, underlining the potential of metallic, hybrid, and polymer-based sandwich structures for the development of lightweight and sustainable solutions.

2. Sustainability, lightweight materials and innovative technologies

The evolution of structural design in recent years has been deeply influenced by material innovation, optimisation of production processes and the increasing focus on economic and environmental sustainability. In this context, the focus on lightweight and sustainable materials has become a strategic priority for several industrial sectors, particularly those characterised by high-energy consumption and significant environmental impact, such as transport, logistics and aerospace. Reducing structural weight is a key strategy for reducing fuel consumption and emissions, thus contributing concretely to global climate neutrality goals. However, the concept of lightweighting must be integrated with that of sustainability, directing development towards materials and structural solutions that are not only mechanically efficient, but also recyclable, renewable or biodegradable. In this scenario, there are two main lines of research and innovation: the use of advanced composite materials, such as sandwich structures, which offer high mechanical performance with low mass; and the use of innovative manufacturing technologies, such as additive manufacturing, which allows for the design and production of geometrically, functionally and environmentally optimised components. This chapter analyses the state of the art on the use of innovative materials and technologies in sustainable design.

The first part outlines the environmental and industrial context motivating the need for lightweight and low-impact solutions, with a focus on transport sector emissions and global decarbonisation goals.

This is followed by an analysis of composite materials and sandwich structures, exploring their potential in terms of specific strength and structural optimisation.

Particular attention is paid to the hybridisation of sandwiches, with the aim of improving their mechanical behaviour and sustainability throughout their life cycle.

The last section of the chapter is dedicated to the opportunities offered by additive manufacturing, with a focus on biodegradable materials and variable density configurations, evaluating their potential for lightweight and circular applications, such as packaging and components with low environmental impact.

2.1 Background

In recent decades, mechanical and structural design has undergone significant transformations, driven by technological progress in manufacturing processes, advances in materials science and increasing regulatory, economic and environmental demands. Two of the main challenges that influence modern mechanical design are the weight reduction of structures and the introduction and use of environmentally sustainable materials, especially in sectors with high energy consumption and environmental impact such as transport.

Recent data from the Global Carbon Budget 2024 indicate that fossil fuel-related carbon dioxide (CO_2) emissions reached approximately 37.4 ± 2 gigatonnes (Gt) globally in 2024, an increase of 0.8% [-0.3% to +1.9%] compared to 2023 [1] (Figure 1).

This trend reflects the persistent difficulty in decarbonising the key sectors of the global economy. This trend reflects the persistent difficulty in decarbonising the key sectors of the global economy. In particular, the transport industry remains one of the largest contributors, with about 8.24 $GtCO_2$ released in 2023 (≈21% of global CO_2 emissions), making it the world's second largest emitting sector after energy [2]. Despite increasing efforts towards electrification and the spread of alternative fuels, emissions continue to grow due to the continuous increase in demand for mobility, logistics and international trade.

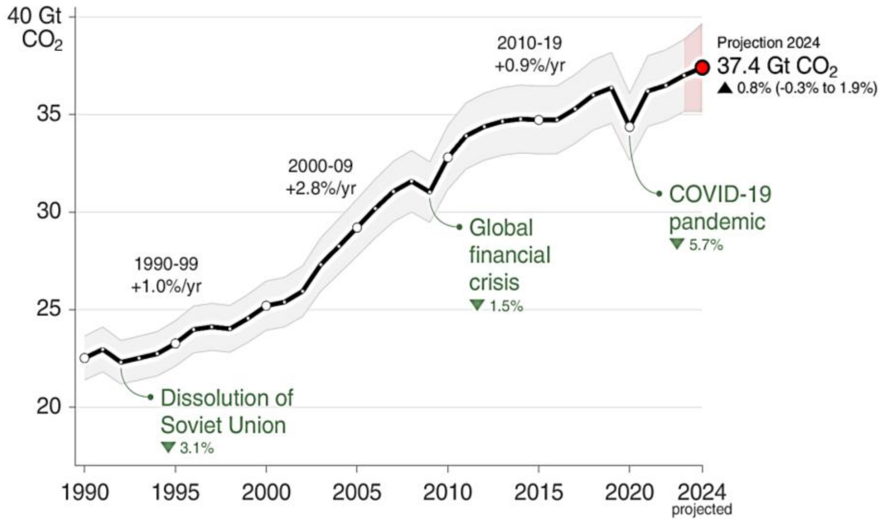

Figure 1: Global fossil CO2 emissions [1].

To remain on track to achieve Net Zero Emissions (NZE) by 2050, the transport sector must reduce emissions by more than 3% per year until 2030. Achieving this goal will require not only cleaner energy sources and electrification, but also a radical shift in design philosophy, where lightweighting and material innovation play a central role. Lightweight design is a strategic driver to simultaneously reduce fuel consumption, limit greenhouse gas emissions and improve system efficiency. A lighter vehicle requires less propulsion energy, improves dynamic performance and allows the downsizing of other subsystems (e.g. engines and braking systems), with consequent benefits on the entire design architecture. These advantages explain why an increasing number of industries, automotive, aerospace, rail and marine, are investing in multi-material design, hybridisation and lightweight solutions: in the maritime sector this translates into lower fuel consumption, greater payload capacity and reduced emissions on long trips [3], [4], while in aerospace it results in lower operating costs and greater fuel economy, both key to reducing aviation's environmental footprint [5], [6].
At the same time, environmental sustainability is no longer a secondary constraint but a design requirement. This evolution is also driven by increasingly stringent

international regulations, such as the European Green Deal and the International Maritime Organization (IMO) decarbonisation targets for shipping, which push industries toward a transition to circular and low-impact models. As a result, structural designers must increasingly balance performance, cost and environmental impact in an integrated, systemic approach.

The adoption of advanced lightweight materials, such as fibre-reinforced composites, metal alloys with a high strength-to-weight ratio and new bio-based materials, has become increasingly important in the automotive, aerospace and maritime sectors. These materials make it possible to reduce structural mass without compromising safety or performance, thus improving energy efficiency and helping to reduce environmental impact throughout the product life cycle.

The growing complexity of material selection and structural optimisation has also driven the integration of advanced digital tools into the design process. Techniques such as generative design and topology optimisation enable the creation of geometrically efficient structures that maximise performance while minimising material usage. In parallel, Life Cycle Assessment (LCA) provides a global view of the environmental impacts associated with materials and manufacturing choices, supporting the development of sustainable solutions that consider recyclability, resource efficiency, and end-of-life strategies.

2.2 Composite materials

The rising interest in composite materials reflects the growing demand for lightweight, high-performance structures for reducing fuel consumption and emissions. In the transport industry where structural mass has a direct impact on energy efficiency and environmental footprint, composite materials offer a good alternative to traditional metal solutions [7].

Composite materials are heterogeneous systems consisting of the combination of two or more distinct phases (Figure 2), typically known as matrix and reinforcement, with the aim of achieving superior mechanical and physical properties compared to the individual constituents [8], [9].

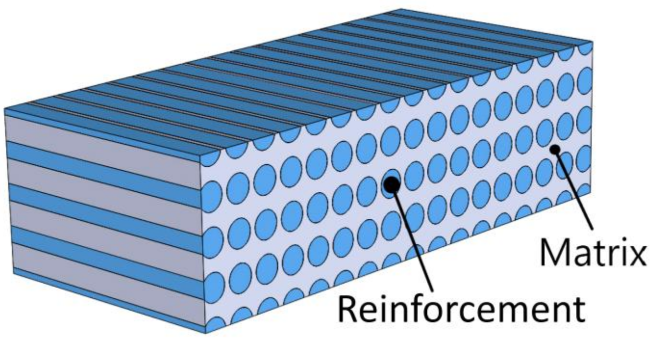

Figure 2: Composite schematic representation.

The interaction between these phases allows the final material to exhibit better characteristics, such as increased stiffness, strength, durability and a superior strength-to-weight ratio, which are crucial in advanced structural applications. Over time, this growing demand has led to a sharp increase in the production and use of composite materials in all industries, thus intensifying their environmental impact [10], [11], [12].

Composite materials can be classified according to the nature of their constituents, i.e. base material and filler material [13]. The matrix (or base material), consisting of a homogenous continuous phase, ensures the cohesion of the composite material by enclosing the reinforcing material. Depending on the type of matrix, composites are mainly divided into three categories:

- Polymer-matrix composites (PMC).
- Metal-matrix composites (MMC).
- Ceramic-matrix composites (CMC).

The reinforcement material consists of a dispersed phase embedded in the matrix, which provides stiffness and mechanical strength to the final material. The arrangement and orientation of the fibres define the properties and structural behaviour of the composite material [14]. Depending on the type of fibre reinforcement, composites can be classified into:

- *Particle-reinforced composites*: containing particle reinforcements dispersed in the matrix.
- *Fibre-reinforced composites*: characterised by the presence of fibres, which can be:
    - Continuous fibres: long fibres that can be unidirectional (aligned along a single axis) or bidirectional (twisted or arranged in two perpendicular directions).
    - Discontinuous fibres: short fibres that can be aligned in a specific direction or randomly oriented.
- *Structural composites*: such as laminated composites, metal matrix composites with reinforcement and sandwich panels.

A comprehensive classification of composite structures based on reinforcement type is illustrated in Figure 3.

Among the various categories, continuous-fibre composites, particularly unidirectional ones, are widely used in high-performance applications due to their excellent ability to bear loads along the fibre axis. Discontinuous -fibre composites, while generally exhibiting lower mechanical properties, offer better formability and are often easier to manufacture. This makes them suitable for complex geometries or low-cost applications.

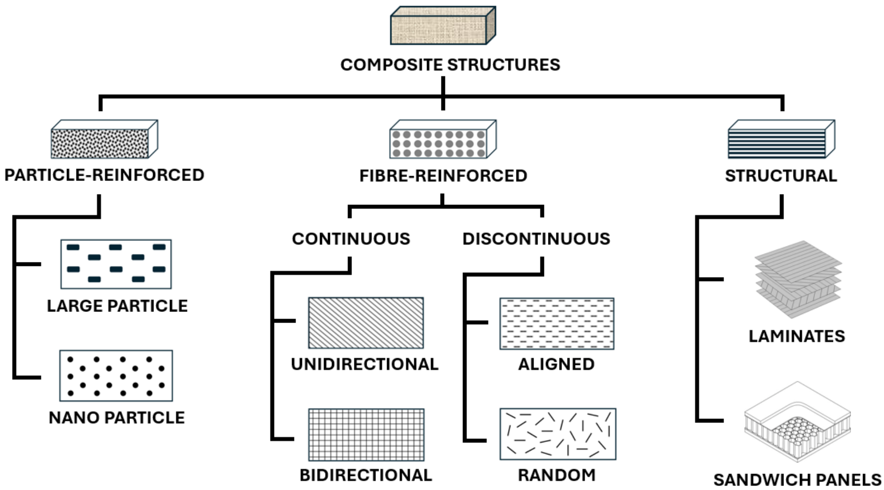

Figure 3: Composite structures classification.

In addition to fibre morphology, an important classification is based on the origin of the fibres, which plays a significant role not only in terms of performance but also in the overall environmental impact of the final composite [15]. Fibres can be grouped into three main categories:

- *Synthetic fibres*: including glass, carbon and aramid fibres, are the most common for structural applications.
    - Glass fibres (GFRP) are valued for their low cost, good mechanical strength and corrosion resistance. These characteristics making them suitable for large-scale industrial applications, including wind turbine blades, marine structures and construction components.
    - Carbon fibres (CFRP) offer high strength-to-weight and stiffness-to-weight ratios, making them the favourite choice in aerospace, motorsport, and high-performance applications. However, their

production is energy-intensive, and their recyclability remains limited.
    - Aramid fibres (AFRP), such as Kevlar, are known for their toughness and impact resistance, and are often used in ballistic protection and dynamic loading environments.
- *Natural fibres*, which are sourced from renewable resources, can be broadly classified into cellulosic fibres, such as flax, hemp, jute, sisal, and cotton, and mineral fibres, such as basalt. Cellulosic fibres are biodegradable, lightweight, and require significantly less energy to produce compared to synthetic reinforcements [16]. Although their mechanical performance is lower than that of synthetic fibres, they are increasingly used in applications such as automotive and ship interiors, packaging, and low-load structural components. Their relevance is particularly notable in eco-design and circular economy strategies, where material sustainability and end-of-life considerations are crucial. Mineral fibres are extracted from natural volcanic rocks and represent an intermediate solution in terms of performance and sustainability between synthetic and cellulosic fibres. Basalt fibres offer good mechanical strength, high thermal resistance, chemical durability, and a lower environmental impact compared to glass or carbon fibres. These properties make them attractive for marine, automotive, and construction applications.

Figure 4 shows a summary of the classification of synthetic and natural fibres.

Synthetic FRPs are not biodegradable and can persist in the environment for hundreds of years. Despite their environmental drawbacks, they are widely used in the transportation sector due to advantageous properties such as corrosion resistance and a high strength-to-density ratio [17], though they remain vulnerable to impact damage [18]. Managing the end-of-life (EoL) of these composites remains a critical challenge, as fibre-reinforced polymers are difficult to recycle, hazardous and costly to dispose of, and require significant energy during production.

Figure 4: Classification of synthetic and natural fibres [15].

These issues underscore the importance of incorporating sustainable considerations in a product's life cycle assessment (LCA), from raw material extraction to EoL strategies, and highlight the need for alternatives such as reuse, recycling, and safe disposal. Therefore, to minimize environmental impact and promote sustainable development, the introduction of environmentally friendly

materials and innovative technologies is necessary.
In this context, bio-composites emerge as a promising eco-sustainable alternative. Made with natural fibres as reinforcement and bio-based polymers as the matrix, they offer environmental advantages over synthetic composites, including lower impact and greater availability [19]. Nevertheless, natural fibres have certain limitations as they are sensitive to moisture, which can lead to swelling, and often exhibit weaker adhesion to polymer matrices. Although their mechanical properties are generally inferior to those of synthetic fibres, their lower density can provide advantages for weight reduction in composite applications, particularly in non-structural automotive components.
Beyond natural fibre composites, another sustainable approach involves structural composites such as laminates and sandwich panels, which combine layers or components to optimise performance under specific loading conditions. These configurations are especially beneficial in aerospace, automotive, and marine engineering, where a high performance-to-weight ratio is essential. Owing to their mechanical efficiency and design flexibility, these types of composites will be further analysed in the following section.

2.3 Sandwich structures

Sandwich structures are an advanced form of structural composites widely used in engineering fields such as aerospace, automotive, marine and civil engineering, where weight reduction and high mechanical performance are critical requirements. The American Society for Testing and Materials (ASTM) defines a sandwich structure as follows:

"A structural sandwich is a special form of a laminated composite comprising of a combination of different materials that are bonded to each other so as to utilise the properties of each separate component to the structural advantage of the whole assembly."

Sandwich structures consist of two rigid and strong outer faces bonded to a lightweight core. This configuration increases the overall thickness and moment of inertia without significantly increasing mass, thus improving the structure's stiffness and flexural strength, following the same principle as I-beams [20], [21]. Figure 5 shows a schematic representation of a typical sandwich structure and its components: faces, core material and adhesive joints.

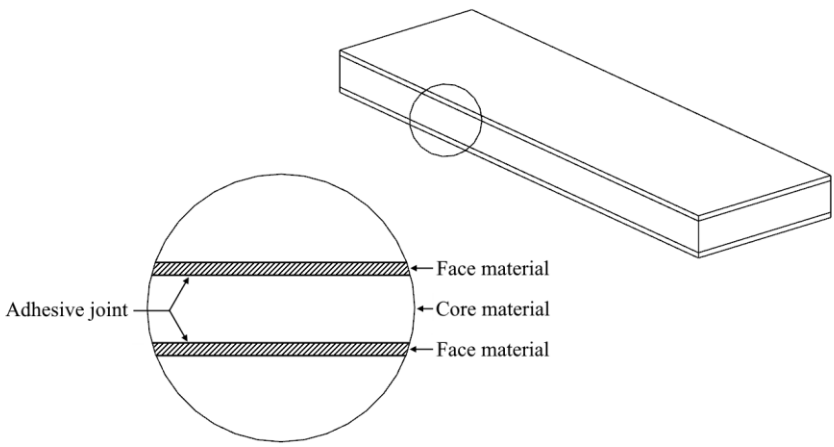

Figure 5: Schematic of a sandwich structure.

The face sheets, typically made of high-strength materials such as metals or fibre-reinforced composites, are mainly responsible for in-plane load transfer and flexural rigidity, like the flanges of an I-beam.
The core, usually a lightweight material such as foam, honeycomb or lattice structures, increases the panel thickness, thereby maximizing the area moment of inertia (*I*) and section modulus (*W*), with minimal weight contribution, thus improving its strength-to-weight ratio and flexural rigidity [22]. Figure 6 illustrates the so-called "sandwich effect", assuming a scenario where the density of the skins is 20 times greater than that of the core.

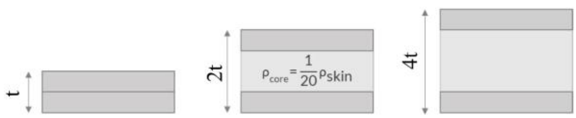

	Solid material	Sandwich structure	
Area moment of Inertia I (facings)	1	7	37
Section modulus W ($I/d_{max\ neutral\ axis}$)	1	3.5	9.2
Total weight	1	1.05	1.15

Figure 6: "Sandwich effect".

Several researchers have extensively studied the mechanical efficiency, manufacturing challenges, and failure mechanisms of sandwich structures in various engineering fields [23], [24], [25]. Despite the wide variety of possible sandwich configurations, it is possible to identify some common advantages and limitations. Table 1 summarises the main advantages and disadvantages reported in the literature for sandwich structures.
Sandwich structures can be classified according to the nature of the materials used for the surfaces and core, as well as the geometric configuration of the core. These classifications are essential to understanding the design flexibility and application-specific customization that sandwich systems offer.

Table 1: Advantages and limitations of sandwich structures

Advantages	Limitations
High strength-to-weight and stiffness-to-weight ratios	Complex design due to diverse material combinations and failure modes
Ability to combine different material properties in one structure	Challenging design and implementation of joining systems
Excellent crashworthiness and good damping properties	Sensitivity to core damage and face-core debonding
Reduction in number of parts and assembly time	Possible manufacturing difficulties and strict quality control
Improved component quality through prefabrication	Limited fire resistance depending on materials
Simplification of structural architecture	Higher initial costs for design and materials
Time and cost savings during assembly	Maintenance and repair are often more complex

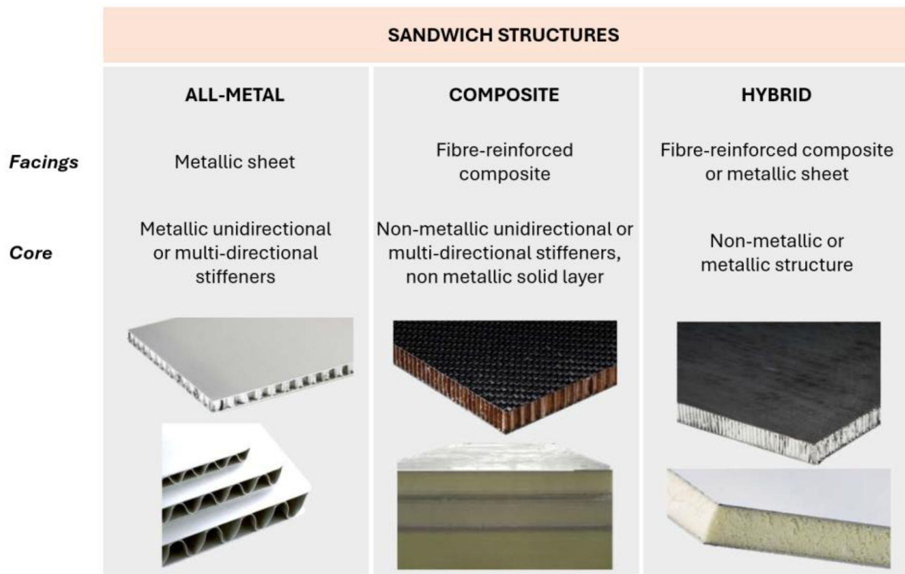

Figure 7: Material-based classification of sandwich structures.

Figure 7 illustrates the classification of sandwich structures based on material composition.

- *All-metal sandwich structures* employ metallic face sheets combined with cores made of metallic unidirectional or multidirectional stiffeners. Materials such as aluminium, steel, or titanium alloys are typically used. This configuration provides excellent fire resistance, thermal conductivity and structural integrity, and is often chosen when high mechanical performance under extreme conditions is required. The use of similar materials for both facings and core also facilitate manufacturing and bonding compatibility. Common applications include aerospace, defence, and civil structures exposed to high thermal or mechanical loads.
- *Composite sandwich structures* feature fibre-reinforced polymer (FRP) face sheets such as CFRP or GFRP, bonded to non-metallic cores including unidirectional or multidirectional stiffeners, solid layers, or foams. They provide superior strength-to-weight ratios, corrosion resistance, and fatigue life. These structures are widely used in the aerospace, automotive, and marine industries, especially where lightweight construction is critical.
- *Hybrid sandwich structures* combine different classes of materials in the surfaces and core to exploit the specific benefits of each component. For example, lightweight composite skins can be combined with metal cores to improve mechanical strength and thermal stability, or metal surfaces can be combined with polymer or bio-based cores to reduce weight and improve environmental performance. This configuration enables the development of structures that are simultaneously lightweight, strong, and tailored to the functional and environmental requirements of the intended application.

The core material in sandwich structures plays a crucial role in defining the mechanical behaviour, weight, and overall performance. Depending on the geometry and distribution of the core material, sandwich structures can be classified into three main categories:

- *Unidirectional stiffeners*: the core consists of beams, bars, profiles, corrugations, or extrusions aligned predominantly in one direction. These reinforcements provide good bending stiffness and strength primarily along the alignment direction. Some examples include corrugated cardboard or corrugated sheets.
- *Multi-directional stiffeners*: the core features geometries that provide stiffness and support along several axes, allowing loads to be distributed more evenly throughout the structure. Examples include honeycomb cores, foam cores, and lattice structures. These configurations provide enhanced performance in terms of shear strength and indentation resistance, making them highly versatile for a variety of engineering applications.
- *Solid core*: the core consists of a continuous, homogeneous material layer without internal voids or cellular geometry. This configuration provides uniform mechanical support and high compressive strength. Solid cores are particularly suitable for applications requiring high load capacity and impact resistance, where weight is a secondary concern.

Figure 8 provides a visual summary of the three main core types, with representative examples that highlight the wide range of geometries and materials available for sandwich structure design. Selecting the most appropriate core configuration is critical for tailoring the panel's performance to specific requirements such as stiffness, strength, weight, and environmental response.

Adhesive joints ensure effective stress transfer between the core and face plates, playing a crucial role in maintaining structural integrity under load. Various types of structural adhesives can be used depending on the materials involved and the performance requirements. Common examples include epoxy resins, which offer high strength and excellent thermal and chemical resistance; polyurethane adhesives, valued for their flexibility and versatility; and phenolic resins, typically used in high-temperature or fire-resistant applications.

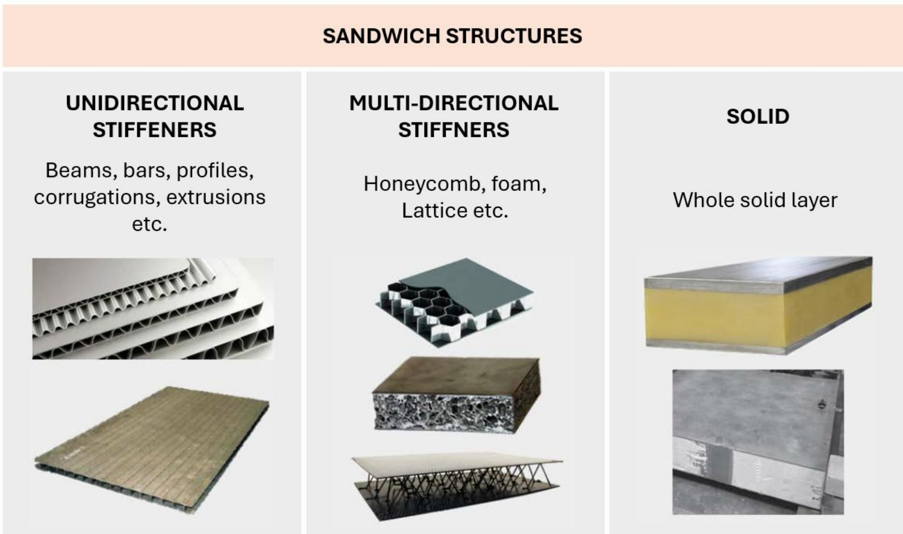

Figure 8: Core classification of sandwich structures.

The selection of adhesive affects not only the bonding quality but also the long-term mechanical and environmental durability of the structure. The bonding can also be achieved through alternative techniques such as welding, blending or other techniques, although structural adhesives remain the most common solution. The mechanical performance of sandwich composites is highly dependent on the intrinsic properties of their constituent materials and the manufacturing processes employed, which critically influence interfacial bonding, defect formation and overall structural response [26]. The versatility of sandwich structures derives from the wide range of possible combinations of core geometries and face materials, which allow mechanical performance to be tailored to specific application requirements.

2.4 Design methodologies for sandwich structures

Based on the general description provided in the previous section, this part examines the mechanical response of sandwich structures under different loading conditions, with particular attention to their flexural and impact behaviour. The discussion concludes with a classification and analysis of the main failure modes typically observed in these structures.

2.4.1 Three-point bending response of sandwich beams

Flexural behaviour is of relevance, as it represents a dominant loading scenario for sandwich components in most structural applications. The theoretical analysis of sandwich beams is based on Timoshenko beam theory, first adapted to sandwich structures by Plantema [27] and Allen [28], and later refined by several researchers, including Zenkert [29]. Figure 9 illustrates a representative sandwich beam and the characteristic geometric parameters, loading configuration and boundary conditions, which form the basis for subsequent analytical formulations.

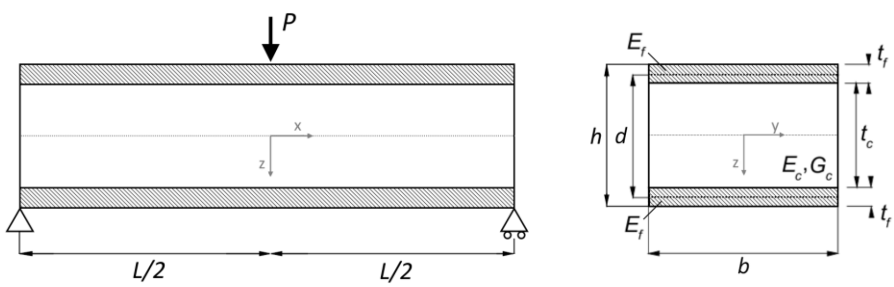

Figure 9: Sandwich beam under three-point bending.

The analysis is based on the following assumptions:

- the load configuration is static;
- deformations remain within the elastic range;
- the surface sheets adhere perfectly to the core;
- both the surfaces and the core are composed of isotropic materials;

- the stiffness of the surface materials is significantly higher than that of the core;
- the beam is narrow, allowing stresses in the y-direction to be neglected.

Under these assumptions, when the beam is subjected to bending due to a concentrated load, the curvature ($1/R_c$) is directly proportional to the bending moment (M) as expressed by Eq. (1):

$$\frac{M}{EI_x} = -\frac{1}{R_c} \tag{1}$$

In a conventional beam, the product EI_x represents the bending stiffness *(D)*, where E is the Young's modulus and I_x is the second moment of area about the bending axis.

As shown in Figure 9, denoting E_f and E_c as the Young's moduli of the face sheets and the core, respectively, the following equation expresses the bending stiffness of a sandwich beam:

$$D = E_f\frac{bt_f^3}{6} + E_f\frac{bt_f d^2}{2} + E_c\frac{bt_c^3}{12} \tag{2}$$

Where:

- b = beam width
- t_f = skin thickness
- t_c = core thickness
- d = distance between the centroids of the face sheets

The first two terms correspond to the bending stiffness contributions of the face sheets, whereas the third term represents the bending stiffness of the core, evaluated relative to the neutral axis. For conventional sandwich panels, the second term predominates. Specifically, when the conditions outlined in Eqs. (3) and (4) are satisfied, the contributions of the first and third terms become negligible, as their values are less than 1% of that of the second term.

$$3\left(\frac{d}{t_f}\right)^2 > 100 \tag{3}$$

$$6\frac{E_f}{E_c}\frac{t_f}{t_c}\left(\frac{d}{t_c}\right)^2 > 100 \tag{4}$$

The maximum bending moment and transverse force occurring in the beam under these loading conditions are:

$$M_{max} = \frac{PL}{4} \tag{5}$$

$$T_{max} = \frac{P}{2} \tag{6}$$

The resulting deformations and stresses in the surface plates (ε_f, σ_f) and in the core (ε_c, σ_c) are respectively:

$$\epsilon_f = \frac{M_z}{D}; \qquad \sigma_f = \frac{M_z}{D}E_f \tag{7}$$

$$\epsilon_c = \frac{M_z}{D}; \qquad \sigma_c = \frac{M_z}{D}E_c \tag{8}$$

where z is the coordinate measured respectively within the facing and the core. The maximum stresses in the face sheets and in the core occur at the sections furthest from the neutral axis.

$$\sigma_f = \pm\frac{M}{D}\frac{h}{2}E_f \tag{9}$$

$$\sigma_c = \pm\frac{M}{D}\frac{t_c}{2}E_c \tag{10}$$

For a sandwich structure with a weak core ($E_c \ll E_f$), the core's elastic modulus can be neglected (i.e., $E_c = 0$), resulting in zero normal stress within the core.

Furthermore, if the face sheets are sufficiently thin ($t_f \ll t_c$), the conditions (3) and (4) are satisfied and the normal stress distribution in the face sheets can be approximated as constant.

$$\sigma_f = \pm \frac{M}{bt_f d} \tag{11}$$

In a homogenous beam, the shear stress τ in a section produced by a shear force T_z in that section is expressed as follow:

$$\tau_{xz} = \frac{T_z S_x(z)}{I_x b(z)} \tag{12}$$

where $S_x(z)$ denotes the first moment of area with respect to the neutral axis as a function of the z-coordinate, and $b(z)$ represents the section width as a function of the z-coordinate. However, for a sandwich beam, it is necessary to consider the presence of different components and materials. Therefore, Eq. (12) is modified accordingly, resulting in Eq. (13).

$$\tau_{xz} = \frac{T_z}{D\, b(z)} \sum S_x(z)_i\, E_i \tag{13}$$

where D is the bending stiffness of the entire section and $\Sigma\, S_x(z)_i\, E_i$ is the sum of the products of the first moment of area and the Young's modulus of all components of the sandwich structure.
The shear stress in the core $\tau_{xz\,c}$ is equal to:

$$\tau_{xz_c} = \frac{T_z}{D(z)} \left[E_f \frac{t_f d}{2} + \frac{E_c}{2} \left(\frac{t_c^2}{4} - z^2 \right) \right] \tag{14}$$

Therefore, the maximum shear stress in the core occurs at the neutral axis, where $z = 0$, while the minimum shear stress in the core is found at the interface with the face sheets, where $z = \frac{t_c}{2}$. This point also corresponds to the maximum shear stress in the face sheets. The ratio between the maximum and minimum shear stresses is approximately equal to one. This implies that the shear stress within the core can be reasonably assumed to be uniform. Given that, in sandwich structures, the ratio between the distance separating the centroids of the face sheets and the core thickness is close to unity, the assumptions commonly adopted for simplifying the stress analysis become nearly equivalent. Thus, when the core is much weaker than the face sheets, its contribution to the overall bending stiffness can be considered negligible, and the shear stress within the core can be approximated as constant. Consequently, by assuming the core's elastic modulus as zero, the shear stress in the core can be expressed as:

$$\tau_c = \frac{T_z}{D}\frac{E_f t_f d}{2} \tag{15}$$

Furthermore, if the bending stiffness of the end plates about their centres of gravity is negligible, i.e. if condition (3) is satisfied because the thickness of the core is significantly greater than that of the end plates, the expression for the shear stress in the core can be further simplified as:

$$\tau = \frac{T_z}{bd} \tag{16}$$

The corresponding shear strain for this condition is:

$$\gamma = \frac{T_z}{G_c bd} \tag{17}$$

where G_c is the core shear modulus. The normal and shear stress distribution in a sandwich beam is represented in Figure 10, where different levels of approximations are compared.

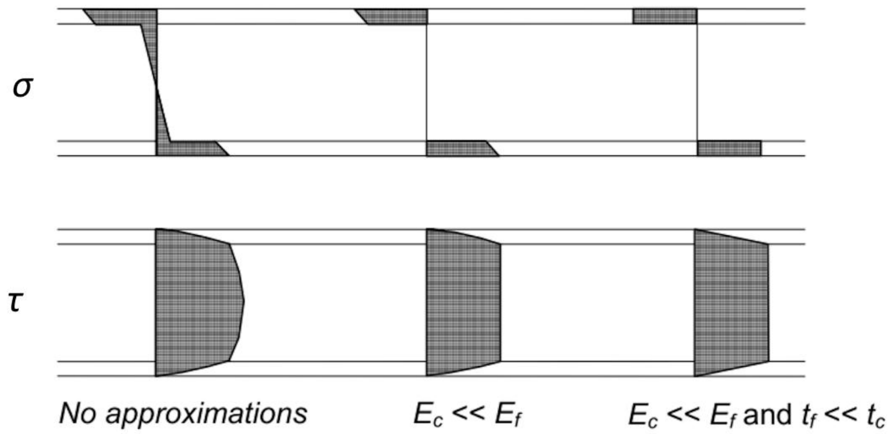

Figure 10: Normal and shear stress in a sandwich beam under three-point bending [29].

The total deflection δ of a sandwich beam arises from the combined effects of bending (δ_b) and shear deformation (δ_s), according to Eq. (18).

$$\delta = \delta_b + \delta_s = \frac{k_b P l^3}{D} + \frac{k_s P l}{A G_c} \tag{18}$$

where, k_b and k_s are deflection coefficients associated with bending and shear, respectively, and depend on the boundary and loading conditions. The product AG_c represents the shear stiffness of the sandwich beam. A is defined as:

$$A = \frac{b d^2}{t_c} \tag{19}$$

For a simply supported beam subjected to three-point bending, the deflection coefficients are k_b = 1/48 and k_s = 1/4. The bending component induces rotation of the beam sections, maintaining their perpendicular to the neutral axis. In contrast, the shear component causes an additional vertical displacement of the sections. The deflection behaviour of a simply supported sandwich beam under three-point bending is shown in Figure 11.

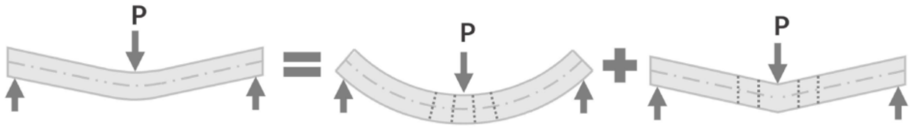

Figure 11: Deflection of a simply supported sandwich beam under three-point bending.

In addition to their flexural behaviour under static or quasi-static loading, sandwich structures are often subjected to dynamic loads such as impacts. These dynamic events introduce different response characteristics, including localized damage mechanisms and energy absorption phenomena, which complement the deformation modes observed during bending. Understanding both static and dynamic responses is therefore essential to fully characterize the mechanical performance of sandwich beams. The following discussion focuses on the impact behaviour, highlighting typical damage modes and relevant experimental observations.

2.4.2 Impact Response of sandwich structures

Impact refers to a dynamic interaction between a mass, which can assume various geometric configurations, and a target body. According to Cantwell and Morton [30], a low-velocity impact occurs when the speed does not exceed 10 m/s, whereas events exceeding this threshold are classified as high-velocity impacts. This type of dynamic event typically induces nonlinear responses in the target element. Various analytical models have been developed to describe the behaviour during impact, differing in terms of complexity and accuracy. A comprehensive review of modelling methodologies was presented by Abrate [31], which serves as the primary reference for the present discussion.

The following description focuses on two fundamental models widely adopted in the literature, recognized for their effectiveness in predicting the response of sandwich structures:

- The mass-spring model;

- The energy-balance model.

One of the most common and effective approaches for modelling structural response to impact is to represent the structure as an equivalent mass-spring system, as first proposed by [32]. Originally, this model accurately describes the impact phenomenon in small-scale laboratory tests, where deformations remain limited. More recent developments extend it to account for large structural deformations by introducing geometric nonlinearities and membrane-stiffening effects. The equivalent system is illustrated in Figure 12.

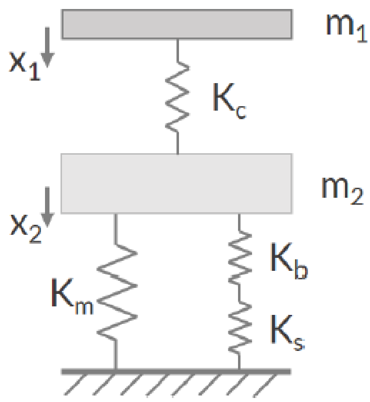

Figure 12: Mass-spring model

In its most general configuration, the model is defined as a two-degree-of-freedom system composed of:

- m_1 representing the projectile mass;
- m_2 corresponding to the equivalent mass of the sandwich structure;
- The spring K_c simulates the non-linear contact stiffness;
- The linear springs K_b and K_s, arranged in series, represent the linear stiffness of the structure due to bending and shear deformations, respectively. This series arrangement can be replaced by a single equivalent spring (K_{bs}) accounting for both effects;
- a spring for the non-linear membrane stiffness (K_m);

The motion equations for this two-degree-of-freedom system are expressed by:

$$\begin{cases} m_1\ddot{x_1} + P = 0 \\ m_2\ddot{x_2} + K_{bs}x_2 + K_m x_2^3 - P = 0 \end{cases} \tag{20}$$

where P is the contact force. For small geometric deformations, the system can be simplified to a single-degree-of-freedom model, assuming the structure moves together with the impact. In this case, the dynamics are reduced to the equation.

$$m_1\ddot{x_1} + K_b x = 0 \tag{21}$$

The general solution for Eq. (21) is:

$$x = Asin\omega t + Bcos\omega t \tag{22}$$

where:

$$\omega = \sqrt{\frac{K_b}{m}} \tag{23}$$

The constants A and B are determined by the initial conditions of the motion, including the impact velocity. For the simplified single-degree-of-freedom formulation given in Eq. (21), the motion can be solved by introducing the initial conditions:

$$\begin{cases} x(t = 0) = 0 \\ \dot{x}(t = 0) = v \end{cases} \tag{24}$$

where *v* is the initial impact velocity. The resulting displacement is:

$$x = \frac{v}{\omega}\sin(\omega t) \tag{25}$$

Under these assumptions, the contact force equals the force in the linear spring:

$$P = K_{bs}x(t) = v\sqrt{(K_{bs}m_1)}\sin(\omega t) \tag{26}$$

From the Eq. (26), it is evident that the maximum contact force is directly proportional to the impact velocity and to the square root of the impact mass and the structure stiffness K_{bs}. The use of spring-mass models in impact analysis makes it possible to predict the contact force history, provided that the structural stiffness is known.

An alternative approach for describing impact events is based on the principle of energy conservation. Here, the initial kinetic energy of the impacting mass is spent to deform the target structure. If the structural response can be reasonably approximated as quasi-static, when the maximum deflection of the structure is achieved, the velocity of the impacting mass becomes zero and the entire kinetic energy was used to deform the structure. Neglecting damage-related energy dissipation, the balance can be expressed as:

$$\frac{1}{2}mv^2 = E_b + E_{sh} + E_m + E_{cn} \tag{27}$$

Where:

- m_1 = projectile mass;
- v = impact velocity;
- E_b = bending deformation energy;
- E_{sh} = shear deformation energy;
- E_m = membrane deformation energy;
- E_{cn} = local indentation energy in the contact zone.

According to mass-spring model, the relation between contact force and deflection at impact point (w_b) is equals to:

$$P = K_{bs}w_b + K_m w_b^3 \tag{28}$$

The elastic energy due to bending, shear and membrane effects is therefore:

$$E_b + E_{sh} + E_m = \frac{1}{2} K_b w_{b,max}^2 + \frac{1}{4} K_m w_{b,max}^4 \tag{29}$$

To evaluate E_{cn}, a contact law is required to relate the contact force (P) to the indentation (α), defined as the relative displacement between indenter and target. A common choice is Meyer's law:

$$P = K_c \alpha^n \tag{30}$$

where K_c is the contact stiffness coefficient and n is a dimensionless exponent. Although Eq. (30) describes static contact conditions, it provides accurate predictions in many low-velocity impact scenarios. The corresponding contact energy is:

$$E_{cn} = \int_0^{\alpha_{max}} P \, d\alpha = \frac{P_{max}^{1+\frac{1}{n}}}{(n+1) \, K_c^{\frac{1}{n}}} \tag{31}$$

If membrane effects are neglected ($K_m = 0$), combining Eqs. (28), (29) and (31), the initial kinetic energy in Eq. (27) can be expressed as:

$$\frac{1}{2} m v^2 = \frac{P_{max}^2}{K_{bs}} + \frac{P_{max}^{1+\frac{1}{n}}}{(n+1) \, K_c^{\frac{1}{n}}} \tag{32}$$

Eq. (32) allows the determination of the maximum contact force from known structural and contact parameters, linking measurable quantities, such as mass and velocity, to the structural response.

The impact behaviour of sandwich structures involves various damage mechanisms, such as core crushing, face-core debonding, and delamination, which directly affect structural integrity and performance. Understanding these mechanisms is crucial for predicting structural response and optimizing design.

2.4.3 Failure modes of sandwich structures

The failure modes of a beam or sandwich panel depend on various factors, including loading conditions, material properties, core geometry, and the quality of the interface bond. Figure 13 schematically illustrates the main failure modes under bending or compressive loads.

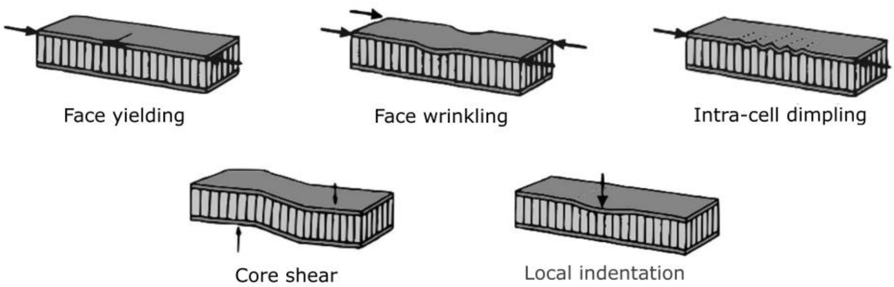

Figure 13: Failure modes in sandwich beams.

To effectively design sandwich structures, it is essential to understand these failure modes to accurately estimate load-bearing capacity and select appropriate materials. Several scientific studies have been published in the literature analysing the collapse modes of sandwich structures [33], [34], [35]. The primary failure modes affecting the skins and core of sandwich panels include:

- *Face yielding*: occurs when the axial stress on one face reaches the in-plane yield strength of the material. Under bending, the upper surface typically experiences compression, while the lower surface undergoes tension. Depending on the material, one stress state may be more critical; for example, metals are generally more susceptible to tensile failure, whereas composites are more sensitive to compressive stresses. The yield condition can be expressed as:

$$\sigma_x = \sigma_{fy} \tag{33}$$

  where σ_x is the axial stress on the surface and σ_{fy} is the yield strength of the surface material.

- *Face wrinkling*: can be interpreted as the axial buckling of the face sheet, supported by the core [36]. When the compressive face sheet of a sandwich panel with a cellular core is subjected to in-plane compressive loads, it may experience local buckling with a wavelength greater than the core cell size. This deformation, known as face wrinkling, can be directed both in towards the core or outwards, depending on the core's compressive stiffness and the strength of the adhesive bond between face and core. In bending, wrinkling typically appears on the compressed (upper) face near the load application point. Allen modelled the facing as an infinitely long strut on an elastic foundation extending to infinity on one side [37]. The critical compressive stress that initiates wrinkling is given by:

$$\sigma_{fw} = \frac{3}{[12(3-\nu_{cxz})^2(1+\nu_{cxz})^2]^{\frac{1}{3}}} E_f^{\frac{1}{3}} E_3^{\frac{2}{3}} \qquad (34)$$

  where E_f is the in-plane Young's modulus of the face sheet, E_3 is the out-of-plane Young's modulus of the core and ν_{cxz} is the out-of-plane Poisson's ratio of the core

  Eq. (34) shows that wrinkling can be mitigated by increasing the stiffness of both the face sheet and core, especially in the out-of-plane direction.

- *Intra-cell dimpling*: In sandwich panels with cellular cores (e.g., honeycomb), local buckling of the compressed face sheet may occur between adjacent core walls where the skin is unsupported. This phenomenon, known as intra-cell dimpling, is critical when the cell size is relatively large or the face sheet is thin. Under in-plane compressive loads, the critical stress σ_{fi} at which dimpling initiates can be estimated using the following expression:

$$\sigma_{fi} = \frac{2E_{fx}}{1 - \nu_{fxy}^2}\left(\frac{2t}{s}\right)^2 \tag{35}$$

Where ν_{fxy} is the Poisson's ratio of the face sheet in the axial direction, t is the face sheet thickness and s is the core cell size. Reducing cell size or increasing face thickness raises the dimpling critical stress. The ratio t/s is therefore a key design parameter for suppressing this failure mode.

- *Core shear*: One of the most common failure modes in sandwich structures is associated with shear deformation within the core. When perfect contact is assumed between the skin and the core, the part of the structure with the lowest shear strength will fail first [38]. As previously discussed in Section 2.4.1, in a sandwich beam under three-point bending, and assuming that the face sheets are considerably stiffer and thinner than the core, the shear stress across the core thickness can be considered approximately uniform. In such conditions, the average shear stress τ_{cxz} in the core is given by equation (16). Core shear failure takes place when the applied stress reaches the shear strength of the core material τ_{cs}:

$$\tau_{cxz} = \tau_{cs} \tag{36}$$

- *Local indentation*: occurs when a concentrated load, applied over a contact area much smaller than the core thickness, causes localized crushing of the core material directly beneath the point of application. An empirical approach used to predict the failure for local indentation, assumes that, when the indenter is a cylinder, such as during a three-point bending test, the compressive stress in the core σ_z is the ratio between the applied load P and the contact length l. Failure is predicted when this compressive stress equals the out-of-plane compressive strength of the core σ_{cc}:

$$\sigma_z = \sigma_{cc} \tag{37}$$

2.5 Applications of sandwich structures

The demand for lightweight, high-performance materials has increased significantly in a wide range of engineering sectors. Among these, sandwich structures have emerged as a key solution to meet the growing requirements for structural efficiency, fuel economy and sustainability [39]. Their characteristics and design flexibility favoured widespread adoption across aerospace, shipbuilding, automotive, railway, civil engineering, and renewable energy sectors. In each of these sectors, sandwich structures are customised to meet specific functional and environmental requirements. Scientific research contributes to the development of new materials and configurations, and provides experimental data, theoretical models, and design criteria that enable safer, more efficient, and more quantitatively based design. This knowledge is essential for addressing the specific needs of different application sectors, in terms of mechanical loads, operating conditions, regulatory constraints, and performance objectives such as impact resistance, energy absorption, or weight minimization [40], [41].

The concept of sandwich construction dates to the mid-19th century, but its practical engineering application began during World War II, particularly with the British De Havilland DH.98 Mosquito bomber (Figure 14), which featured a plywood sandwich structure.

Figure 14: De Havilland DH.98 Mosquito.

Subsequent decades saw fundamental theoretical contributions by researchers such as Marguerre, Hoff, Libove, Batdorf, and Allen, laying the foundations for structural modelling of sandwich configurations. Meanwhile, institutions such as the U.S. Forest Products Laboratory and pioneering companies like Hexcel Corporation supported industrial development, initially in wood and later in composite materials [42].

Sandwich structures adoption reflects ongoing efforts to optimise performance, address sector-specific challenges, and explore innovative configurations. In the transportation sector a key design challenge is reducing structural weight while maintaining high mechanical performance.

The use of lightweight materials across numerous automotive components, including dashboards, bumpers, engines, body panels, wheels, suspensions, brakes, steering systems, batteries, seats, and gearboxes (Figure 15) enables enhanced energy efficiency, increased payload capacity, improved operational performance, and, in certain cases, greater safety and stability [43], [44].

Figure 15: Representative lightweight materials used in automotive components [45].

In the shipbuilding industry, sandwich panels serve structural roles (decks, hulls, bulkheads, and superstructures) while meeting stringent functional and environmental requirements, including impact and fatigue resistance, corrosion prevention, and fire safety compliance [17]. They are also widely employed in interior outfitting, such as floors, partitions, and furniture, for their acoustic and vibration damping capabilities combined with ease of installation. Beyond their structural contribution, sandwich panels can improve vessel performance and operational efficiency by increasing available volume, simplifying the structural architecture, and reducing material costs and construction time (Figure 16). Nevertheless, broader adoption is still limited by challenges related to design complexity, joining systems, and the standardization of testing and certification procedures. European initiatives such as the SANDWICH and SAND.CORe projects, as well as the MARSTRUCT network, have contributed to advancing knowledge and reliable design methodologies for marine sandwich structures [44].

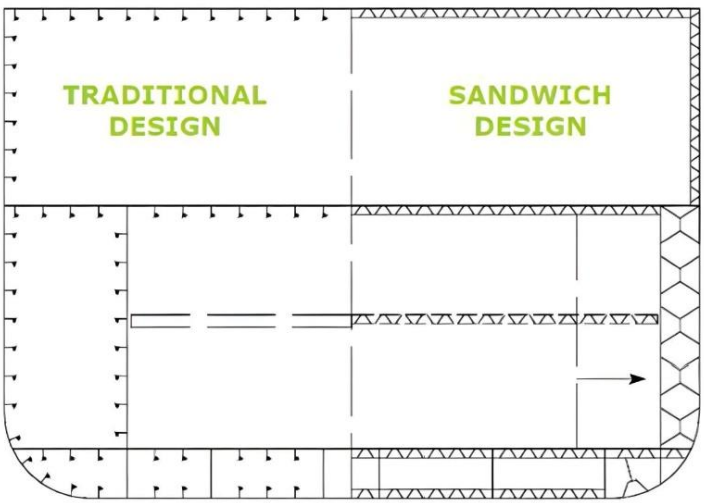

Figure 16: Comparison of traditional design and sandwich design for a ship [44].

Sandwich structures are widely employed in the aerospace sector, serving structural functions in fuselage skins, floors, and control surfaces. Their use in commercial aircraft has increased significantly over time: for instance, they covered only about 8% of the wet surface area of the Boeing 707, while in the Boeing 757 and 767 this proportion rose to approximately 46%, mainly due to the adoption of Nomex honeycomb cores [46]. A key milestone was the “Beech Starship”, the first aircraft built almost entirely with sandwich panels combining Nomex cores with graphite and Kevlar skins. Honeycomb sandwich structures are furthermore employed in spacecraft, including satellites (Figure 17) and shuttles, due to their excellent stiffness-to-weight ratio. In addition, panels for aerospace applications must resist the mechanical and thermal loads encountered during flight, including dynamic pressures, thermal cycling, and vibration [47].

Figure 17: Example of a satellite sandwich structure (Image from www.beyondgravity.com).

In the railway industry, sandwich structures are extensively used to optimize vehicle interiors while enhancing safety and operational efficiency. These applications include panels for floors, walls, ceilings, seats, tables, and storage units, which are designed to reduce overall vehicle weight without compromising structural strength, while meeting key functional requirements such as energy absorption, crashworthiness, acoustic insulation, and modular integration [48]. Moreover, sandwich structures are employed in critical components such as compartment walls and doors, as well as in access systems like ramps and sliding steps, owing to their resistance to corrosion and mechanical stresses.

As discussed in Section 2.3, the mechanical and functional performance of sandwich panels is strongly influenced by the choice of core and skin materials, production methods, and bonding techniques. Advances in composite materials, hybrid configurations, and bonding technologies have significantly expanded design possibilities and performance capabilities.

2.5.1 Composite sandwich structures

Composite sandwich panels, particularly those composed of fibre-reinforced polymer (FRP) skins and lightweight cores, have been widely adopted since the mid-20th century, initially in aerospace applications for weight reduction. Their success in this sector later led to widespread use in marine, automotive, and railway industries, where performance, durability, and reliability are essential. The appeal of these panels lies in their distinctive combination of features, including high specific stiffness and strength, long service life, low maintenance requirements, ease of forming complex geometries, and excellent impact-absorbing capabilities [49], [50], [51]. Together with their design flexibility, these properties make sandwich panels highly suitable for lightweight, durable engineering applications.

In transportation and industrial sectors, panels can be tailored with composite laminated skins and different types of cores to meet specific operational requirements. For instance, in marine applications, panels must withstand both large collision events and localized low-speed impacts to ensure high standards of safety and reliability. Such impacts may occur during normal service due to collisions with floating or submerged objects, accidental tool drops, or contact with docks and other vessels. Their frequency is amplified in marine and offshore environments because of unpredictable sea states and dense traffic. The susceptibility to impact damage is a significant issue, particularly for sandwich laminates [18]. Damage in the form of delamination or internal defects may compromise structural integrity, limiting the reliability of composite materials in critical applications. Despite advances in design and manufacturing, the risk of such damage remains, and research continues to explore ways to enhance strength and durability under various loading conditions. Experimental analyses, such as Low-Velocity Impact (LVI) testing, provide direct insight into these events, which are often difficult to capture theoretically or numerically due to the complex nonlinear behaviour of multi-material sandwich structures. However, LVI experiments typically require specialised, expensive equipment, and standard machines are often limited to small-scale specimens; while results can be scaled to predict first failure on larger structures, post-failure responses are less easily generalized [52].

Glass fibre reinforced polymer (GFRP) skins combined with lightweight cores, such as polyurethane foam (PU), polyvinyl chloride (PVC), or balsa wood, remain widely used due to their excellent strength-to-weight and stiffness-to-weight ratios. Studies have analysed the behaviour of GFRP panels with these traditional cores [53], [54], [55], [56], [57], [58], showing that core type and panel geometry strongly influence out-of-plane performance. GFRP/PVC panels provide high corrosion resistance and durability under environmental exposure, making them suitable for marine applications, whereas GFRP/balsa panels offer a favourable balance of mechanical performance and low weight but are more sensitive to moisture and localized impact damage [59], [60]. The mechanical properties of the core, including shear and compressive strength as well as shear modulus, directly affect bending behaviour and overall panel performance [35], [61], [62]. Studies have shown that glass fibre face sheets generally exhibit better resistance to damage than carbon fibre under such extreme conditions, while polymer foam cores outperform balsa wood in terms of energy absorption and impact mitigation [63]. Beyond their mechanical performance, these structures provide multifunctional benefits, including thermal insulation, vibration damping, and the potential integration of additional functionalities such as energy storage.

Extensive research has been carried out to relate quasi-static perforation tests to LVI tests, aiming to develop predictive parameters that estimate the dynamic behaviour of materials from simpler and more economical experiments. Among these, the Dynamic Scaling Factor (DSF) provides a quantitative means to translate responses observed under quasi-static loading to those expected under dynamic impact scenarios [64], [65], [66].

The use of quasi-static testing as a cost-effective approach is highly attractive, potentially reducing experimental costs and facilitating scaling of results from the laboratory to full-scale [52], [67]. Studies by Dr Sutherland and co-authors on pultruded GFRP multicellular hollow deck panels, with or without polyurethane foam filling and epoxy-polyurethane coatings, demonstrated that correlations between quasi-static and impact tests can be established [68].

However, the knowledge gained in these studies has made it clear that for each different material system, the correlation between quasi-static and low-velocity impact results should be investigated and understood, as it may vary significantly depending on the specific composite or other material combination, panel architecture, core configuration, and impact geometry. By establishing reliable correlations, such as those provided by the DSF, engineers can anticipate potential damage, optimise material selection, and guide the design of sandwich structures without extensive dynamic testing.

Despite the well-known and numerous advantages of composite sandwich structures, there are critical aspects that limit their use in specific application areas. These include susceptibility to impact and delamination, reduced fire resistance, polymeric moisture absorption and difficulties in repair, recycling and end-of-life management. The susceptibility of laminated composite materials to out-of-plane impacts has been widely reported in the literature, highlighting the risk of internal damage such as delamination, matrix cracking, and core shear failure under low-velocity impact scenarios [30], [69], [70], [71], [72]. These limitations are particularly relevant in sectors requiring high durability, thermal resistance and environmental sustainability. To answer these demands, research is moving towards the development of metal and hybrid sandwich structures that can overcome these limitations without sacrificing the advantages of the sandwich concept.

2.5.2 Full-metal sandwich structures

Full-metal configurations, particularly those in aluminium alloys, offer high structural strength, fire resistance, recyclability, and a superior strength-to-weight ratio. With a density of only 2.69 g/cm^3 (approximately one-third that of conventional steel), aluminium provides excellent weight efficiency, directly translating into reduced fuel consumption, improved acceleration, and enhanced crashworthiness in transport applications. From an environmental standpoint, replacing conventional steel or cast iron with aluminium in the transport sector can lead to substantial life-cycle reductions in greenhouse gas emissions, with reported savings on the order of several tens of tons of CO_2 per ton of aluminium employed [45]. Aluminium is widely considered a sustainable and adaptable material due to its high recyclability and almost infinite reusability [4]. Recycling aluminium significantly reduces greenhouse gas emissions and energy consumption compared to primary production, thus minimising environmental impact. Although aluminium alloys are generally more expensive than steel and scrap recycling may introduce impurities, continuous advances in alloy design, manufacturing technologies, and recycling processes are progressively mitigating these issues. Emerging solutions such as scrap dilution with primary aluminium, improved refining methods, and selective reuse strategies are enhancing the cost-effectiveness and reliability of recycled aluminium, further consolidating its role as a key material for lightweight and sustainable sandwich structures [73].

Within this context, aluminium sandwich panels have been identified as particularly promising for transport applications, combining lightweight properties with environmental sustainability. In literature, aluminium sandwich structures have been studied with a variety of core types, including honeycomb, foam, and corrugated metal, each offering distinct trade-offs between weight, stiffness, energy absorption, and manufacturability. The wide variety of aluminium alloys, ranging from 2000 to 6000 series, further broadens the design possibilities, enabling tailored combinations of corrosion resistance, strength, and formability. For instance, 2000 series alloys are often used in high-strength automotive components such as pistons and suspension parts, while 6000 series alloys combine good formability with excellent corrosion resistance, suitable for structural and crash-relevant elements [45].

Building on these material advantages, numerous experimental and numerical studies have investigated the static and dynamic behaviour of aluminium sandwich structures, with particular focus on energy absorption, failure mechanisms, and fatigue performance. Among the most representative contributions, Crupi et al. [74] investigated the static and impact response of aluminium sandwiches with both foam and honeycomb cores, demonstrating that these structures are lightweight and capable of significant energy absorption. The research highlighted the influence of parameters such as indenter geometry, cell size, and skin-core adhesion on the distinct collapse mechanisms of honeycomb (progressive cell wall buckling) versus foam cores (foam crushing).

Furthermore, Palomba et al. [75] analysed the fatigue behaviour under bending conditions, focusing on failure mechanisms and the effect of support span on fatigue life, showing that shorter spans lead to core shear-dominated failure, while longer spans result in skin failure. Their study also demonstrated that the bending response is independent of strain rate, and they developed an analytical model capable of predicting collapse mechanisms and fatigue limit loads.

Zhang et al. [76] considered the mechanical behaviour and energy absorption characteristics of aluminium foam sandwich panels under repeated impact, comparing experimental results with numerical FE simulations. Tillman et al. [77] focused on quasi-static mechanical performance, examining the role of parameters such as core density, defects, and load direction. Palomba et al. [4] developed a novel and practical methodology for the preliminary design and optimisation of aluminium honeycomb panels. By employing materials charts and failure maps, they provided an effective tool to guide the selection of design variables while simultaneously emphasising the dual advantage of mechanical performance and life-cycle sustainability.

2.5.3 Hybrid sandwich structures

Parallel to full-metal sandwich structures, hybrid solutions have attracted increasing attention, as they allow combining the strengths of composite and metal materials, thus adapting performance to specific application requirements. As widely reported in the literature [78], [79], [80], [81], [82], [83], the core of sandwich structures can be designed in at least three ways: foam, lattice, and honeycomb. In these hybrid sandwiches, both the core and the skins can be made of different materials, provided proper interfacial bonding is ensured [49], [84]. The performance and failure mechanisms of hybrid sandwiches strongly depend on the quality of the interface, mainly controlled by the type and viscosity of the adhesive. For example, Avila de Oliveira et al. [85] explored the use of two epoxy adhesives with different viscosities on flax fibre-bamboo core panels, demonstrating that higher-viscosity adhesives increase indentation modulus, whereas lower-viscosity adhesives ensure better penetration into the interface pores and consequently higher shear strength. Similarly, Merum et al. [86] investigated aluminium honeycomb sandwiches using five different polyurethane adhesives, highlighting the close correlation between interfacial bonding strength and failure mechanisms under low-velocity impact.

Hybrid sandwiches with CFRP, Kevlar, or flax fibre reinforced polymer (FFRP) skins combined with aluminium honeycomb or corrugated cores exhibit complex mechanical behaviour, influenced by material properties, skin and core thickness, core architecture, adhesive type, and impactor geometry [87], [88]. In this scenario, a growing interest is increasingly directed towards sandwich structures involving metal cores and composite skins (or vice versa), which can simultaneously ensure lightness and advanced performance [41], [89], [90], [91], [92]. Among the already tested technological solutions, noteworthy are aluminium sandwich structures reinforced with carbon fibre skins [93], [94], Kevlar fibre skins [95], and so on.

These materials are susceptible to impact damage showing complex failure modes. Even small or barely visible damages can reduce mechanical properties, potentially leading to structural failure during service [96]. Impact resistance depends on the impact conditions and the response in terms of deflection, force, and energy absorption [18]. For this reason, before applying them in the transportation industry, it is necessary to provide detailed information about LVI damage characterization and post-impact failure modes.

The response of hybrid sandwiches to impact loading is of critical importance, as accidental events such as tool drops, hail, or bird strikes can induce interlaminar delamination, local fracture of the face sheets, or crushing of the metallic core, ultimately reducing the structure's load-carrying capacity [91].

For this reason, many studies focus on impact damage characterization and failure mechanisms of composite sandwich structures [70], [97], [98], [99], [100]. Using drop-weight impact experiments and microscopic X-ray computed tomography, Sun et al. [101] investigated the impact deformation and damage characteristics of sandwich panels in relation to their structural parameters. The images obtained from the impact tests revealed a positive correlation between impact energy and the extent of damage. The perforation resistance and energy absorption capacity of the specimens increased significantly with the thickness of the CFRP face sheets. Liu et al. [102], [103] studied the low-velocity impact and blast load deformations, as well as the energy absorption capacity, of sandwich panels with various types of tube-filled honeycomb cores. Additionally, some researchers have examined the effect of temperature on the impact response to broaden the potential applications of sandwich structures [104], [105]. Bending tests studies are less common compared to tensile and compression tests. Li et al. [106] highlighted the necessity to improve the bending strength of conventional honeycomb and studied the mechanical behaviour of sandwich beams with tailored hierarchical honeycomb cores, allowing improved bending performance. Moreover, many structural components, for example in the ship hull in naval industry or in the automotive field [107], are subjected to bending loads. It is therefore important to evaluate also the response of hybrid sandwiches in terms of the load, energy absorption and the failure mechanism [108], [109], [110]. Wang et al. [111] analysed the bending performance and the failure modes of conventional honeycombs hybridised with ceramic face-sheets, highlighting positive effects on strength and stiffness. Bending behaviour of sustainable sandwich structures is attracting high attention among researchers. Indeed, novel recyclable wood sandwiches are currently being studied [112], [113], showing promising mechanical performance.

In conclusion, sandwich structures are versatile and high-performing solutions, offering an optimal balance of lightweight design, mechanical strength, and energy absorption. Their adaptability, ranging from composite panels or natural fibre skins to metal and hybrid configurations, allows tailoring to diverse applications across aerospace, marine, automotive, and railway sectors. Performance depends on material selection, core architecture, interface quality, and loading conditions, with experimental and numerical studies providing critical insights into impact behaviour, failure mechanisms, and design optimization. Despite persistent challenges, including delamination, moisture sensitivity, and limited repairability, ongoing advances in hybrid and metallic sandwich structures are progressively overcoming these limitations, enhancing applicability and enabling safer, more efficient, and sustainable engineering designs.

2.6 Additive manufacturing

Additive manufacturing (AM), as defined by International Standard EN ISO/ASTM 52900, refers to technologies capable of joining materials to create objects directly from 3D model data, usually layer upon layer, as opposed to subtractive manufacturing and formative processes [114]. This approach facilitates the manufacturing of complex geometries, including internal lattice structures and topologically optimized components, while simultaneously minimizing material waste and enhancing resource efficiency. As a result, AM emerges as a pivotal technology within the framework of Industry 4.0 [115], and more recently Industry 5.0, which emphasizes sustainability, resilience, and human-centric innovation.

Despite these numerous advantages, the technology still faces significant challenges that hinder its widespread industrial adoption. These include anisotropic mechanical properties, process-induced defects, limited build volumes, the need for support structures, relatively high costs in some applications, and the absence of fully validated design and certification methodologies tailored for AM parts.

The development of AM can be divided into five major periods:

- The first phase (late 1970s-early 1980s) was characterized by isolated examples of early prototypes or “proto-AM” technologies.
- The second phase (mid-1980s-around 1990) saw the invention and commercialization of three fundamental 3D printing methods, together with the foundation of pioneering companies.
- The third phase (1990-2005) marked a stage of technological maturation, with the introduction of new processes and improvements in computational design and 3D imaging.
- The fourth phase (2005-2012) followed the expiration of key patents, which broadened access to 3D printing. The rise of social media and the

"maker movement" further opened the technology to hobbyists and small users.

- Finally, the fifth phase (2012-present) is defined by rapid growth, diversification of methods and materials, and increasing support from governments and research institutions, including innovations such as bioprinting.

AM processes can be classified according to the methodology employed to construct layers. The ASTM taxonomy identifies seven primary categories [116], which are reported in Figure 18 and Table 2.

Figure 18: Classification of additive manufacturing (Figure adapted from the EN ISO/ASTM 52900 (2015) standard).

Table 2: ASTM taxonomy for Additive Manufacturing processes

Category	Definition (ASTM-based)
Binder jetting (BJ)	A liquid bonding agent is selectively deposited to join powder materials
Directed energy deposition (DED)	Focused thermal energy is used to melt material during deposition
Material extrusion (ME)	Continuous extrusion of a material through a nozzle or orifice
Material jetting (MJ)	Selective deposition of droplets of build material, which solidify to form the object
Powder bed fusion (PBF)	Thermal energy selectively fuses regions of a powder bed
Sheet lamination (SL)	Sheets of material are bonded together to form an object
Vat photopolymerization (VP)	A liquid photopolymer in a vat is selectively cured by light-activated polymerization

Each category encompasses different processes sharing the same deposition principle but differing in process parameters, materials, and achievable properties. AM employs a wide selection of materials tailored to specific applications. Common polymers include thermoplastics such as PLA, ABS, and nylon, as well as photopolymers used in vat photopolymerization. Metals range from stainless steels and titanium alloys to nickel-based superalloys, aluminium, and cobalt-chromium alloys [117], [118], [119], [120]. Ceramics are mainly applied in high-performance and biomedical contexts. Composite materials, combining polymer matrices with fibre or particle reinforcements, are also utilized to enhance performance. This broad material variety enables the technology to meet diverse industrial demands but requires careful control of processing conditions and post-processing.

A typical AM workflow begins with the design of the component using 3D CAD modelling, followed by conversion to a suitable format (e.g. high-resolution "Standard Triangulation Language" (STL)) and slicing to generate machine code (e.g. G-code). The process continues with machine setup, manufacturing, and post-processing operations such as heat treatments, machining, or coatings, which are essential to achieve the desired final properties [121]. This approach transforms the traditional paradigm of "design for manufacturing" to "manufacturing for design" [122], offering greater design freedom and enabling highly optimised geometries. Furthermore, by reducing conventional design constraints, AM fosters innovation in the design phase and revolutionizes supply chains through on-demand, localized production that reduces inventory costs and lead times [123], [124].

2.7 Applications of additive manufacturing

Despite the challenges outlined, additive manufacturing has demonstrated its versatility and strategic value in several high-impact sectors, including aerospace, biomedical, and automotive. Its characteristics, particularly in the design of complex structures such as lightweight components with optimized cores, open new frontiers in creating high-performance parts. The requirement for specific mechanical properties, coupled with production flexibility, has driven the adoption of additive manufacturing in a variety of industrial applications.

In biomedical industries, AM enables the fabrication of patient-specific implants, surgical tools [125], and customized patient-specific solutions, while also reducing surgical times. Furthermore, 3D printed models derived from magnetic resonance imaging (MRI) and computed tomography (CT) scans allow surgeons to practice complex procedures, enhancing precision and reducing risks [126].

In the aerospace sector, additive manufacturing plays an important role in reducing structural weight while maintaining or even enhancing mechanical performance. This is achieved through topology optimization and the production of intricate internal geometries, such as conformal cooling channels and lightweight lattice structures, which are extremely difficult or impossible to produce with traditional methods [127], [128]. These design capabilities translate directly into improved thermal management, reduced fuel consumption, and extended service life of critical components [129]. AM also facilitates the use of high-performance materials like nickel-based superalloys, titanium alloys, and custom-developed alloys optimized specifically for AM processes. These materials are essential for manufacturing engine parts, heat exchangers, and load-bearing structures that operate under extreme thermal and mechanical conditions. Moreover, AM enables reducing the number of components, and thus potential failure points, improving reliability, and simplifying the supply chain. Despite these advantages, challenges remain such as process certification, material limitations, post-processing requirements, and fatigue performance under complex loading conditions.

Similarly, in the automotive sector, AM is emerging as a key technology for producing end-use components, specialized tooling, and customized parts. Weight reduction is particularly critical for electric vehicles, as lowering mass directly impacts battery range and overall efficiency. Moreover, additive manufacturing allows the integration of complex geometries and advanced functionalities in a single component, enabling intricate housings for sensors, antennas, and electronic devices, and meeting the growing demand for smart and connected vehicles.

In the architecture and construction sector, additive manufacturing allows for reduced manufacturing times and costs, while increasing design flexibility. Robotic systems and 3D concrete printers enable the production of complex building components, such as structural elements, walls, and bridges [130], [131]. However, due to limited experimental data and validated models, further research is required to ensure the safety and reliability of AM structures [132].

Among the various industries, packaging has recently benefited from AM's ability to create foamed or cellular structures directly during the printing process, offering lightweight, protective solutions that can be tailored to the product’s geometry and mechanical requirements, enhancing impact resistance and reducing material usage. The development of Foam Additive Manufacturing (FAM) technique, introduced by Tammaro et al. [133], [134], has further expanded these possibilities. FAM combines the design freedom of additive manufacturing with the intrinsic advantages of foam materials, such as low density and energy absorption, and allows precise local control of foam morphology during printing. The process typically involves pre-treating the filament with a physical blowing agent (PBA) [135], which expands during extrusion to create bubbles within the polymer while preserving its chemical properties. This extrusion process is illustrated in Figure 19, showing how the filament is transformed into foamed structures during printing. Unlike chemical blowing agents, PBA preserves recyclability and lifecycle advantages of the polymer, making it particularly suitable for sustainable manufacturing [121], [136]. Nofar et al. [137] investigated how key FAM parameters affect foam properties.

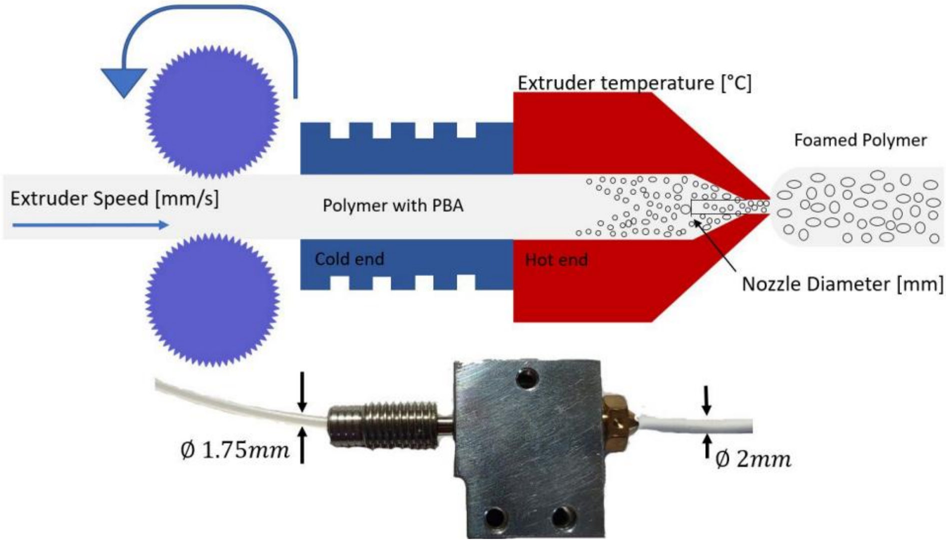

Figure 19: Extrusion process outline: sketch (top) and real picture (bottom)[134].

In addition to filament-based FAM, lithographic 3D printing also enables the production of foamed parts using a resin with a chemical blowing agent (CBA) that degrades with heat, producing a uniform foam morphology [138], [139].

Recent studies underline FAM's potential to create mono-material components with finely tuned mechanical properties by controlling local density and cellular architecture. This capability enables the fabrication of lightweight structures with tailored stiffness, strength, and energy absorption, making FAM particularly attractive for sustainable packaging and applications where core optimization is essential, such as sandwich panels or composite structures. Polylactic acid (PLA), a bio-based and biodegradable thermoplastic, is a promising candidate for eco-friendly sandwich structures [113] thanks to its favourable mechanical properties and widespread applicability in 3D printing [140]. Niu et al. [141] investigated the influence of different reinforcement types and process parameters on the mechanical properties of PLA, with an emphasis on tensile toughness, identifying specific reinforcement mechanisms for each type of interlayer.

PLA stands out as a benchmark material in the field of sustainable polymers due to its renewable origin and inherent biodegradable properties. Derived from biobased sources such as corn, sugarcane, or beet, PLA significantly reduces reliance on fossil resources, contributing to lower greenhouse gas emissions during its production process [142], [143]. Unlike traditional petroleum-based plastics, the end-of-life phase of PLA showcases its sustainability. Under industrial composting conditions, PLA can decompose into water, carbon dioxide, and biomass, leaving no persistent or toxic residues in the environment [144]. Furthermore, advancements in its mechanical and thermal properties, combined with its competitive cost, make PLA a viable alternative for diverse applications while supporting the principles of a circular economy.

Moreover, PLA foams produced via CO_2 foaming have been extensively studied for packaging applications thanks to their biodegradability [145], [146] , aligning with the growing demand for ecological packaging based on biodegradable materials [147]. These foams are fully biodegradable, which has attracted attention in the field of intelligent packaging. Potential applications include nano-foods [148], bio membranes for wastewater treatment, pharmaceuticals, and composting [149]. The monomer LA is recognized as a safe food preservative, and migration from PLA packaging containers to food is considered negligible. Additionally, PLA is resistant to oils, fats, and chemical agents, making it suitable for food packaging [150].

The development of sandwich structures with polymeric cores has been mostly limited to polypropylene (PP) or polyethylene terephthalate (PET) foams.

Although there are promising applications, the use of additive manufacturing techniques to create sandwich structures with homogeneous polymeric cores has been relatively underexplored. Grünewald et al. [151] discussed the challenges and opportunities of using PP and PET foams in manufacturing such structures, suggesting the need for innovation in using PLA for similar purposes. Fully polymer-based sandwich structures, in which skins and core are made from the same material, remain uncommon. Some studies have investigated all-polypropylene composites [152], while Brischetto and Torre [153] evaluated the mechanical performance of fully PLA honeycomb sandwiches, showing promising results. G. Palomba et al. [154] performed LVI tests on bamboo samples to assess the relationship between structure and mechanical response, which facilitated the design of multilayer corrugated sandwich structures made of PLA for subsequent compression testing. Similarly, Svatik et al. [155] leveraged PLA in Fused Deposition Modelling (FDM) 3D printing to create complex, porous gradient structures inspired by bamboo. These structures exhibited higher maximum strain values compared to solid structures and demonstrated a transition from brittle to quasi-ductile behaviour, avoiding sudden catastrophic failure.

The growing interest in PLA is also motivated by its combination of high workability and environmental sustainability, as the material is biodegradable and processable with conventional techniques such as extrusion, compression moulding, and injection moulding [113], [137], [156], [157]. Traditional processing often requires pre-treatments or finishing steps, which increase time, cost, and waste. Additive manufacturing can mitigate these issues by reducing additional steps and allowing more balanced use of the material [158]. FAM further enhances these possibilities, allowing precise local customization of foam morphology, facilitating optimized mechanical performance across different zones of a single part [137]. Moreover, FAM supports integrated manufacturing approaches, reducing the need for assembly or additional processing steps, simplifying production workflows, and minimizing environmental impact. Its benefits recall principles observed in natural cellular materials, such as honeycombs and echinoids, which achieve high performance with minimal material use through optimized porosity and internal structuring [159], [160], [161]. FAM similarly enables complex internal geometries skin to lattice structures, leveraging the advantages of foam while overcoming the limits of conventional foaming or standard lattice-based AM techniques [162], [163], [164].

3. Quasi-static and impact behaviour of sandwich structures

In the previous chapter, an overview of composite materials and sandwich structures was provided, with particular attention to their classification, main applications, and the growing interest in hybrid and full-metal solutions. Building on this background, the present section introduces the experimental activity carried out to investigate the mechanical performance of aluminium honeycomb sandwich structures in comparison with more conventional composite sandwich configurations.

Sandwich panels constitute a key class of lightweight structural materials, extensively used in transportation and marine applications, where the demand for reduced weight, improved fuel efficiency, and environmental sustainability is steadily increasing. Despite their widespread adoption, conventional composite sandwiches such as GFRP skins with polymeric or natural cores remain vulnerable to localised loading conditions, including quasi-static concentrated loads and low-velocity impacts. These conditions can significantly affect the structural integrity and energy absorption capability of the panels, highlighting the need for alternative solutions (Section 2.5.1).

Aluminium honeycomb sandwich panels are promising candidates in this context. Aluminium alloys offer low density, high versatility, complete recyclability and favourable mechanical properties, making them particularly attractive in terms of both performance and sustainability (section 2.5.2). By considering AHS panels with equivalent flexural stiffness to traditional composite sandwiches, it is possible to assess their effectiveness as replacements in applications where crashworthiness and impact resistance are of primary concern.

The experimental programme presented in this chapter addresses this challenge through quasi-static (QS) perforation and LVI tests. These tests allow a systematic evaluation of the crashworthiness of AHS and composite sandwiches under localised loading.

The chapter is organised into two main sections. The first introduces the materials under investigation and the experimental procedures adopted for quasi-static perforation and low-velocity impact tests. The second presents a comparative study of the energy absorption capacity of AHS panels and conventional sandwich structures, highlighting the potential of aluminium-based solutions as lightweight crashworthy alternatives.

Two material categories were investigated:

- Aluminium honeycomb sandwich panels, representing the full metal alternative;
- Glass fibre reinforced polymer faced sandwich laminates with either PVC foam or end-grain balsa wood cores, representing conventional composite solutions.

For each category, two sub-types of panels were selected: a lighter and thinner configuration, representative of typical hull or superstructure laminates, and a heavier and thicker configuration, representative of structural components requiring higher stiffness and load-bearing capacity.

To enable meaningful comparisons between the two categories of sandwich structures, it was necessary to establish a clear equivalence criterion. Several parameters could in principle be adopted for this purpose, such as overall weight, total thickness, or ultimate strength. However, in marine composite structures, bending stiffness typically governs the design process, making it the most relevant equivalence parameter for the present study. Moreover, bending stiffness can be reliably calculated using well-established analytical formulations, allowing for the straightforward design of equivalent composite and metallic structures. The bending stiffness D was evaluated according to the Eq. (2) reported in Section 2.4.1.

3.1 Materials and methods

This section describes the materials selected for the experimental campaign and their relevant mechanical and geometrical properties. The four representative sandwich configurations were chosen to have comparable bending stiffness. The selected configurations include two conventional GFRP-based laminates and two aluminium honeycomb panels, enabling a systematic comparison between metallic and composite solutions.

Two aluminium honeycomb sandwich panels were used in this study: AHS h11 and AHS h32. AHS h11 consists of AA5754 skins with a thickness of 1 mm and an AA5052 core of 9 mm, while AHS h32 has AA5754 skins of 1 mm and an AA3003 core of 30 mm. In both cases, the honeycomb cell diameter is 6 mm, and the faces are bonded to the core with an epoxy adhesive. The bending stiffnesses of these panels were calculated according to Eq. (2) using a nominal beam width of 1 m, resulting in 3.36×10^9 N·mm²/m for AHS h11 and $3.23 \cdot 10^{10}$ N·mm²/m for AHS h32.

Based on these stiffness values, two types of GFRP composite sandwiches were designed to achieve comparable flexural stiffness:

- GFRP/PVC laminate (lighter and thinner): The biaxial E-glass fabric (ETL 800-1270, 0/90°) was impregnated with Scott Bader VE 679 PA vinylester resin and laminated onto a 15 mm thick Airex PVC foam core (80 kg/m³). Each face consisted of two layers, with a nominal thickness of 0.62 mm per layer, for a total face thickness of 1.24 mm and an overall sandwich thickness of approximately 17.5 mm.
- GFRP/balsa laminate (heavier and thicker): The biaxially stitched E-glass fabric (813 g/m², METYX Composites 5200.002.240) was impregnated

with Scott Bader CRYSTIC VE679PA vinylester resin and laminated onto a 30 mm thick DIAB ProBalsa core (155 kg/m^3). Each face was reinforced with four layers of fabric, giving a total face thickness of 2.5 mm and an overall sandwich thickness of approximately 35 mm.

The bending stiffnesses of GFRP/PVC and GFRP/balsa panels are $3.28 \cdot 10^9$ N·mm^2/m and $3.48 \cdot 10^{10}$ N·mm^2/m, respectively. The main geometrical and mechanical features of the two composite laminates and the two equivalent AHS structures are summarised in Table 3 and Table 4, respectively. Exact equivalence could not be achieved, considering the necessity to use commercially available materials only available in certain configurations (mainly fibre reinforcement areal weights and core densities and thicknesses), but as can be seen in these tables, very close equivalence was obtained, allowing meaningful comparisons between metallic and composite configurations. Both the GFRP/PVC and GFRP/balsa panels were fabricated using vacuum-assisted hand layup. All panels were then cut into 100 × 100 mm specimens using a diamond-surrounded circular saw.

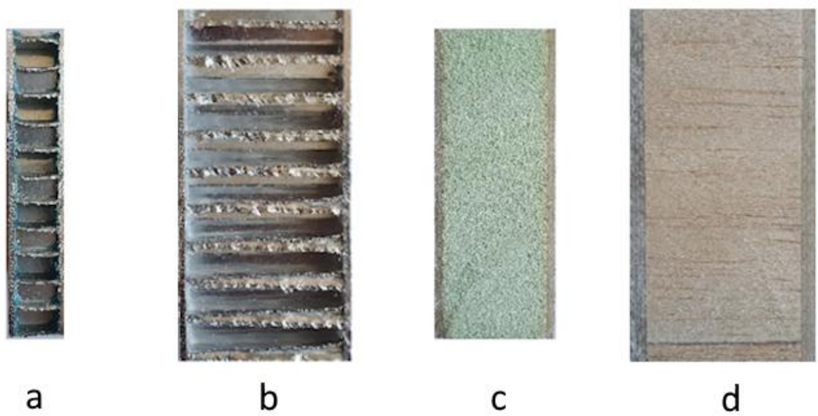

Figure 20: Cross-sectional view of the four sandwich panels: a=AHSh11, b=AHSh32, c= GFRP/PVC, d=GFRP/balsa.

Table 3: Aluminium honeycomb sandwich properties [165].

	AHS h11	AHS h32
Skin material	AA5754	AA5754
Core material	AA5052	AA3003
Skin thickness *t* [mm]	1	1
Core thickness *c* [mm]	9	30
Sandwich thickness [mm]	11	32
Honeycomb cell diameter *Ø* [mm]	6	6
Core density [kg/m^3]	80	54
Skin to core adhesive	Epoxy resin	Epoxy resin
Skin Young's Modulus E_f [MPa]	67000	
Core Young's Modulus E_c [MPa]	2.74	
Bending stiffness [Nmm^2/m]	$3.36 \cdot 10^9$	$3.23 \cdot 10^{10}$

Table 4: Composite sandwich laminate properties [165].

	GFRP / PVC	GFRP / balsa
Skin fibres	2 plies 813 g/m^2 E-glass biaxial 0/90° fabric	2 plies 827 g/m^2 E-glass biaxial 0/90° fabric
Skin matrix	Vinylester resin	Vinylester resin
Core material	Cross-linked PVC foam	End-grain Balsa
Skin thickness *t* [mm]	1.24	2.5
Core thickness *c* [mm]	15	30
Sandwich thickness [mm]	17.5	35
Core density [kg/m^3]	80	155
Skin Young's Modulus E_f [MPa]	24044	26400 [166]
Core Young's Modulus E_c [MPa]	84	4100 [166]
Beam bending stiffness [Nmm^2/m]	$3.28 \cdot 10^9$	$3.48 \cdot 10^{10}$

Figure 20 shows the cross-sections of the four sandwich structures, highlighting the skin and core configurations of both aluminium honeycomb and GFRP-based panels.

Since the QS perforation and LVI tests were to be compared, it was important that the test setups were identical except for the load application. Two different indenters were employed: in all cases, a hemispherical indenter (H10, ISO 6630) with a diameter of 10 mm was used (Figure 21(a)), while a conical indenter (ASTM D5628 Method FB) with a nose radius of 6.35 mm, a base radius of 12.7 mm, and a flare angle of 130° was employed to investigate the influence of indenter geometry on damage modes (Figure 21(b)). Similarly, in all cases, specimens were placed on a rigid hollow cylindrical metal support of 40 and 95 mm internal and external diameters, respectively. No clamping was used, mainly to eliminate inconsistencies between QS and LVI clamping levels.

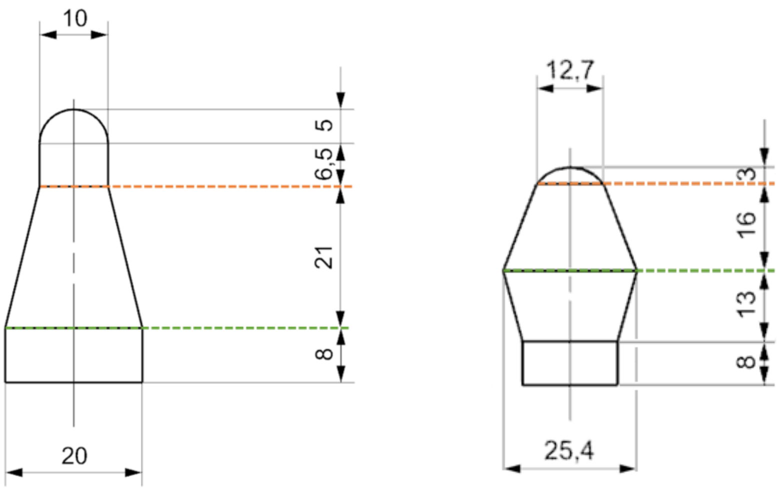

(a) (b)

Figure 21: (a) 10 mm Ø hemispherical tup (ISO 6630)[165] , (b) Conical indenter (ASTM D5628 Method FB). Orange and green lines indicate start and end of conical shaft section, respectively.

QS perforation tests were performed with an ITALSIGMA servo-hydraulic universal testing machine, shown schematically in Figure 22, equipped with a 25 kN load cell and calibrated according to ISO 7500-1 in class 1 [167].

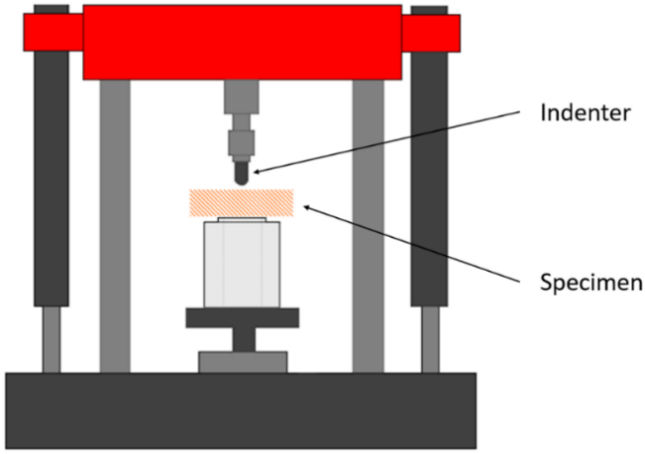

Figure 22: Experimental setup for QS perforation tests [165].

Tests were conducted at room temperature in displacement control mode at a speed of 10 mm/min and were video-recorded to allow correlation between visible failure mechanisms and force-displacement curves. Testing continued until full perforation of the lower face occurred.

LVI tests were carried out using a CEAST Fractovis Plus falling weight impact testing machine (Figure 23). The striker mass and drop height were adjustable to achieve different impact energies, with a sufficiently high Incident Kinetic Energy (IKE) to ensure full perforation of the lower face. The machine is equipped with a multiple impact elimination system that prevents rebound of the impact mass on the specimen, and a spring system can be activated for high-energy tests. The impactor allows interchangeable tups via a threaded connection, and a strain gauge enables precise measurement of the applied force. The specimens were supported by a cylindrical support with internal and external diameter of 40 mm and 90 mm, respectively.

Figure 23: CEAST FRACTOVIS drop test machine [168].

To quantify the energy absorption behaviour of the investigated materials, the following parameters were evaluated for both QS and LVI tests:

- Total Energy Absorption (TEA)

$$TEA = \int_0^{\delta_{max}} F d\delta \tag{38}$$

- Mass and density Specific Energy Absorption (SEA)

$$SEA_m = \frac{EA}{m} \tag{39}$$

$$SEA_\rho = \frac{TEA}{\rho} \tag{40}$$

where F is the force, δ the displacement, m the mass and ρ the density.

The damage modes under QS and LVI loading were evaluated using non-destructive testing (NDT). Radiographic inspections were performed using a BOSELLO SRE m@x system (Figure 24), equipped with a high-power X-ray source (maximum 1800 W, 320 kV) with a variable focal spot size of 0.4-1 mm. The system also includes a manipulator with automatic 4-axis motion control and a flat panel detector with a resolution of 1024 × 1024 pixels.

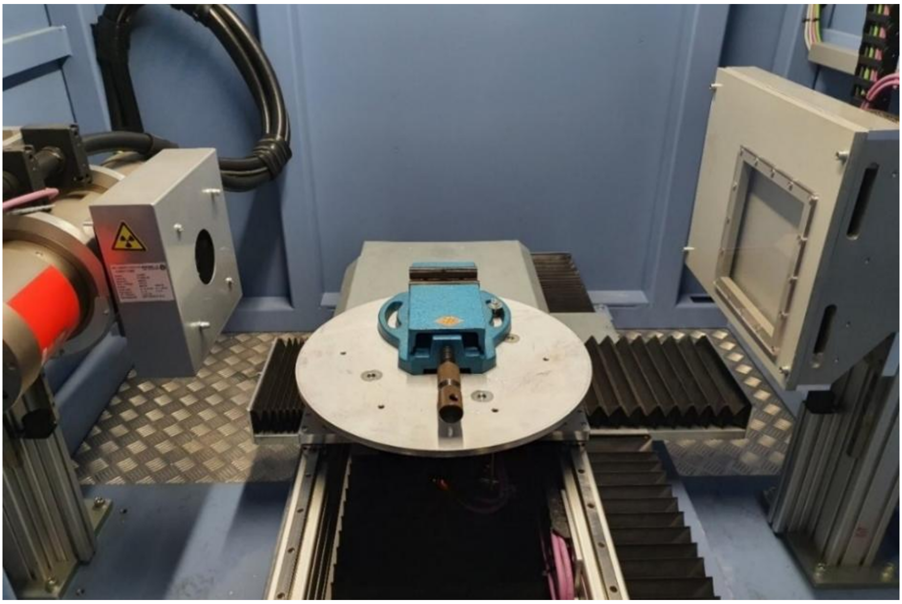

Figure 24: Interior of the BOSELLO SRE m@x X-ray inspection cabinet.

3.2 Mechanical response of sandwich structures under quasi-static and low-velocity impact tests

The first stage of the experimental programme consisted of QS perforation and LVI tests. These provided crucial insight into the energy absorption capability of each sandwich configuration, as well as a preliminary understanding of the sequence of failure events. For each structure, two to three repetitions of both QS and LVI tests were performed up to complete perforation of the lower face. The results proved sufficiently repeatable, allowing representative force-displacement curves to be presented and average values reported in the following discussion.

As described in Section 3.1, both H10 hemispherical and conical indenters were employed, to assess the role of contact geometry on the perforation behaviour of the sandwich panels. The following subsections present the results obtained with the two indenter configurations, highlighting similarities and differences in force-displacement response, damage evolution and energy absorption.

3.2.1 Results obtained by hemispherical indenter

When considering the H10 hemispherical indenter, the force-displacement curves obtained for the four sandwich structures (AHS h11, GFRP/PVC, AHS h32 and GFRP/balsa) under QS and LVI loadings are shown in Figure 25-Figure 28. Video recordings of the QS tests made it possible to correlate specific points on the curves with distinct damage events, which are denoted as points A-E in the figures. Also indicated are the points at which (assuming negligible top face deflection) the start and end of the conical section of the shaft of the H10 hemispherical tup (Figure 21a) would reach the top face (orange and green lines for start and end, respectively). If the overall bending deformation of the specimens was negligible, it would be reasonable to expect an increase in force due to the conical part of the hemispherical indenter shaft at a displacement of approximately 11.5 mm, i.e., when the contact between the conical part above the hemispherical tup and the specimens starts and the top face perforation begins to expand. Another predictable event is the increase in force due to the tip hitting the bottom face at a displacement equal to the total panel thickness minus one skin thickness (10 mm for AHS h11, 16 mm for GFRP/PVC, 31 mm for AHS h32, and 32 mm for GFRP/balsa). Only in the case of AHS h11 would bottom face contact be expected before cone engagement. These considerations would be valid if no deformation occurred; however, the experimental tests revealed slightly more complex mechanisms, as discussed below for each panel.

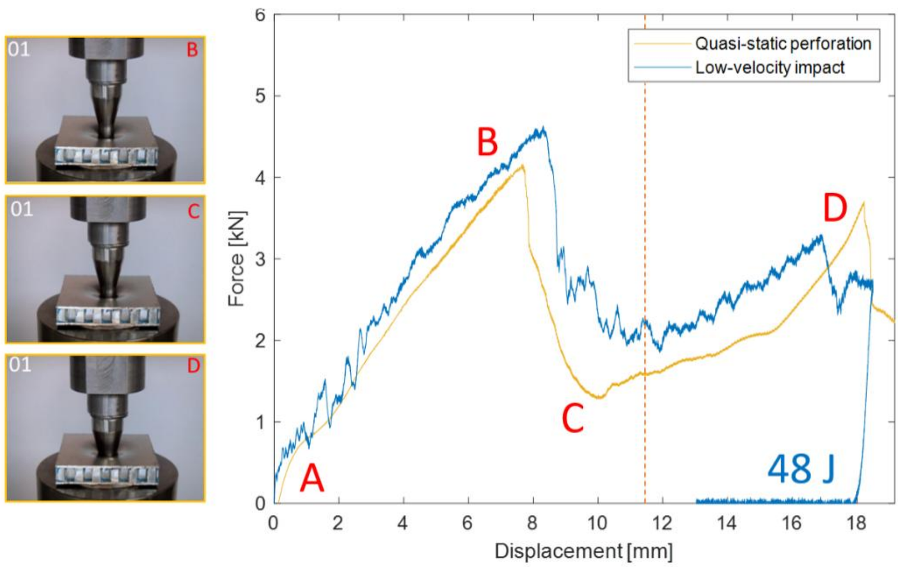

Figure 25: AHS h11 QS and LVI force-displacement responses with H10 hemispherical indenter [165].

The force-displacement curves recorded on the AHS h11 specimens (Figure 25) show two load peaks in both QS and dynamic conditions. After an initial linear elastic response, the load reaches a first peak associated with the failure of the upper skin (point B). Subsequently, core crushing and perforation occur up to point C where load starts to increase. It is challenging to distinguish between the increase in force due to cone expansion of the top face perforation, starting after 11.5 mm of displacement (see orange line in Figure 25), and the force increase attributable to contact with the back face, initiating at around 10 mm. This overlap in mechanisms complicates the interpretation of the observed trends. At point D, failure of the lower skin is observed. The LVI test mirrors the quasi-static behaviour, recording higher value of maximum forces at the first peak, with a perforation energy of 48 J.

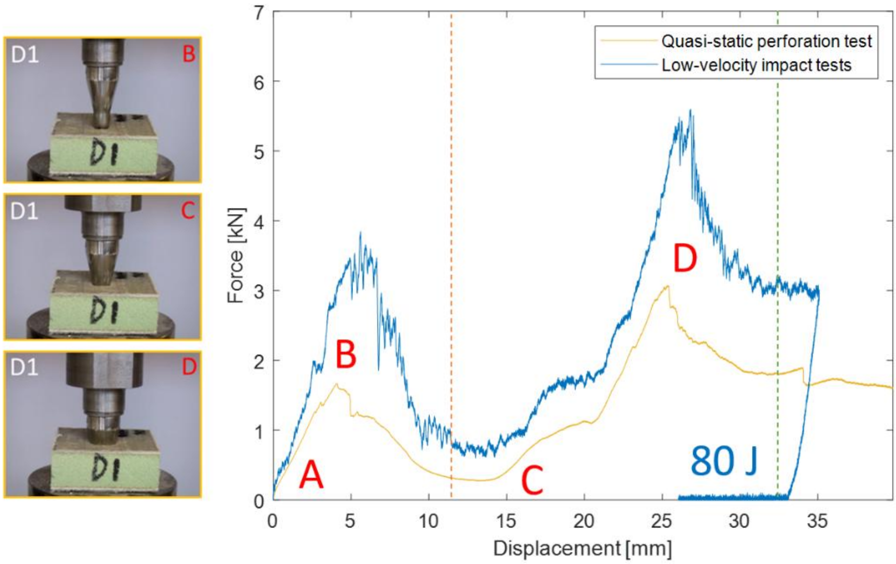

Figure 26: GFRP/PVC QS and LVI force-displacement responses with H10 hemispherical indenter [165].

For GFRP/PVC specimens (Figure 26), the QS perforation test shows a smooth and continuous increase in force up to point B, marking the onset of top face perforation. This is followed by a short plateau, before a significant increase up to point D, corresponding to failure of the lower skin. In this case, the increase in force due to cone expansion of the top face perforation, beginning after 11.5 mm (see orange line in Figure 26), is minimal compared to the increase resulting from back face contact, which starts at approximately 16 mm. During the LVI test, the load peaks at points B and D are noticeably higher, indicating the enhanced energy absorption capability under dynamic conditions.

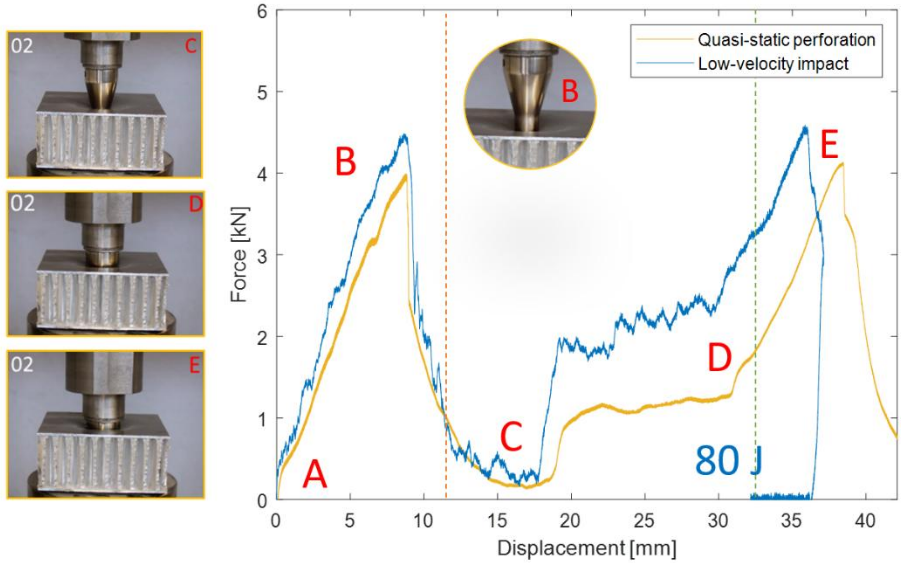

Figure 27: AHS h32 QS and LVI force-displacement responses with H10 hemispherical indenter [165].

Quasi-static tests results for AHS h32 specimens (Figure 27) shows that the force rises to point B (top skin perforation), drops at C, and then increases again until bottom skin failure (point D). during core penetration until point D, and then rises to point E, when lower skin failure occurs. Notably, the force increase due to cone expansion of the top face perforation, starting after 11.5 mm (see orange line in Figure 27), is significantly smaller compared to the increase associated with back face contact, which begins around 31 mm. Additionally, a sharp rise in force is observed at approximately 17 mm, between points C and D, potentially corresponding to the cone entering the material, as the upper aluminium face undergoes significant deformation. For the LVI test, the curve exhibits a more dynamic profile, with multiple peaks and troughs, but the general trend is the same as the QS test and the values of the peak forces are only slightly higher than quasi-static conditions.

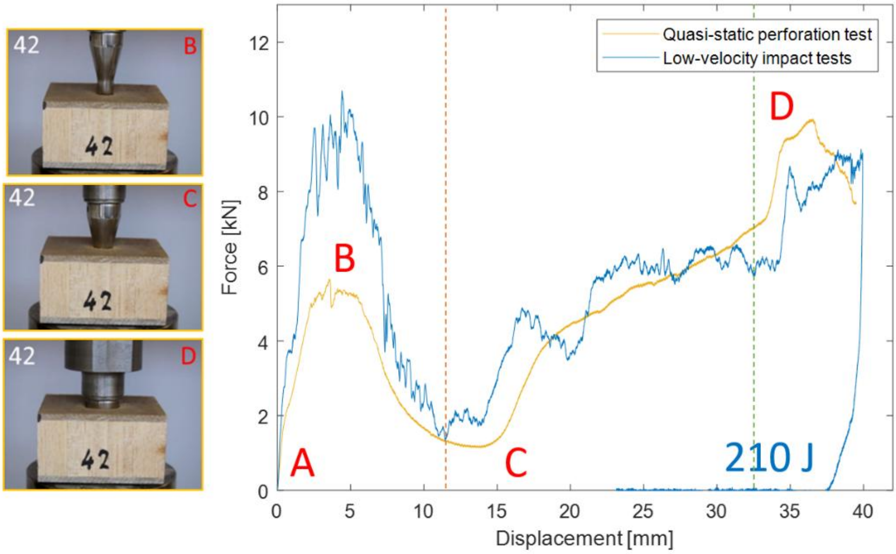

Figure 28: GFRP/Balsa QS and LVI force-displacement responses with H10 hemispherical indenter [165].

In the QS test of GFRP/balsa specimens (Figure 28), force gradually rises to point B, followed by a sharp drop at point C, indicating the initiation of upper skin failure. Subsequently, the force stabilises with minor fluctuations until the lower skin perforation at point D. In this case, the cone significantly contributes to the force increase as it progresses through the top face and rigid balsa core, after 11.5 mm displacement (see orange line in Figure 28), until contact with the back face at around 32 mm. At this stage, there is a pronounced increase in force, corresponding to the onset of back face contact. The LVI test shows a more dynamic response, with multiple peaks and valleys in the force curve. The initial peak at point B, higher than the QS one, is followed by a series of force drops and recoveries, indicating complex failure mechanisms and progressive damage.

The energy absorption parameters corresponding to the quasi-static perforation and LVI tests are reported in Table 5 and Table 6, respectively. For each sandwich structure, the maximum displacement (δ_{max}) used for the calculation of total energy absorbed was taken as the point at which visual inspection confirmed perforation or failure of the lower skin, supported by auditory cues and analysis of the experimental data. This approach ensures that the TEA values represent the energy absorbed up to the complete loss of structural integrity of the lower face.

Table 5: Quasi-static full perforation results with H10 hemispherical indenter [165].

Test	***F_{max} [kN]***	***TEA [J]***	***SEA_m [J/kg]***	***SEA_ρ [Jm^3/kg]***
QS_{avg} AHS h11	4.09	43	1870	0.07
QS_{avg} GFRP/PVC	3.07	54	2324	0.19
QS_{avg} AHS h32	4.27	70	1865	0.29
QS_{avg} GFRP/Balsa	9.95	191	2399	0.42

Comparing test specimens with the same stiffness, the AHS h11 has higher maximum force values but lower energy absorption values than the GFRP/PVC. The comparison between AHS h32 and GFRP/Balsa shows that the maximum load values and energy absorption values are higher in the composite structure.

Table 6: Low-velocity impact full perforation results with H10 hemispherical indenter[165].

Test	***IKE_{test} [J]***	***F_{max} [kN]***	***TEA [J]***	***SEA_m [J/kg]***	***SEA_ρ [Jm^3/kg]***
LVI_{avg} AHS h11	48	4.63	48	2142	0.09
LVI_{avg} GFRP/PVC	80	5.60	80	3220	0.27
LVI_{avg} AHS h32	80	4.59	80	2127	0.33
LVI_{avg} GFRP/Balsa	210	10.7	210	2709	0.48

The total energy absorbed, along with SEA_m and SEA_ρ values at perforation, reported for quasi-static (Table 5) and low-velocity impact conditions (Table 6), indicates that all the sandwich structures exhibit higher energy absorption under dynamic loading than in static conditions.

3.2.2 Results obtained by conical indenter

When considering the conical indenter, the perforation behaviour of the sandwich structures shows some differences compared to the H10 hemispherical case. Figure 29-Figure 32 report the force-displacement curves obtained under QS and LVI loading.

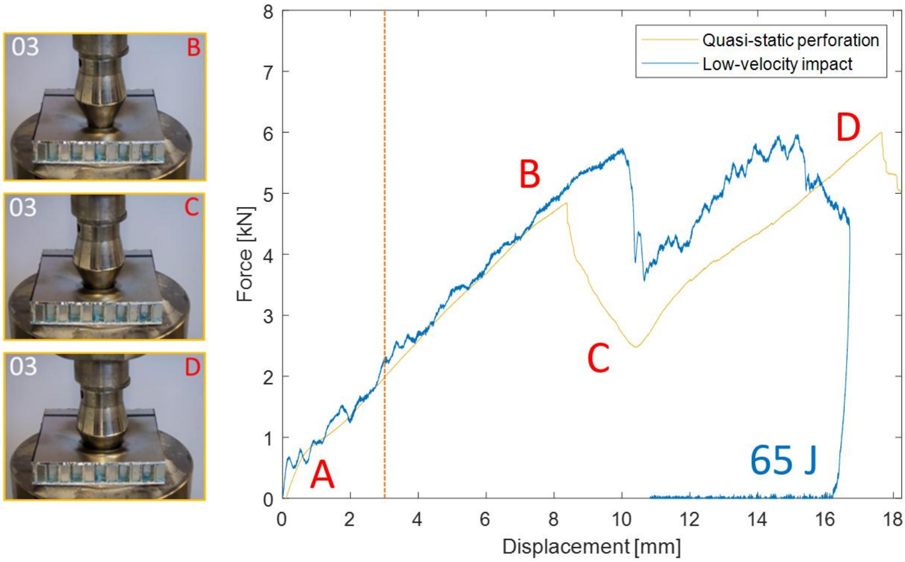

Figure 29: AHS h11 QS and LVI force-displacement responses with conical indenter [169].

For the AHS h11 specimens (Figure 29), the force-displacement curve under QS loading shows an initial linear rise to point B, corresponding to the peak load associated with top skin failure. This event is followed by a load drop, as the core undergoes crushing and perforation up to point C. A second peak is then recorded at point D, when the indenter contacts and eventually perforates the bottom skin. Under low-velocity impact, the trend is similar, with slightly higher peak forces, reaching a perforation energy of 65 J.

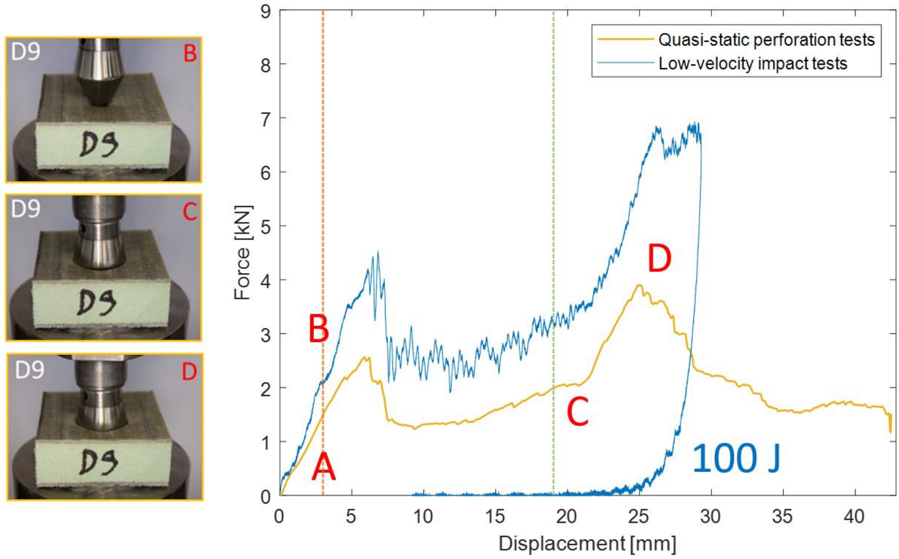

Figure 30: GFRP/PVC QS and LVI force-displacement responses with conical indenter [169].

For the GFRP/PVC specimens (Figure 30) under quasi-static loading, the force increases as displacement increases up to point B, marking the onset of top skin perforation. This is followed by a short plateau, corresponding to complete core crushing and perforation, before a second load peak at point D, corresponding to bottom skin failure. Under low-velocity impact, the overall trend mirrors the QS response, but the load peaks at points B and D are higher, with a perforation energy of 100 J.

Figure 31 and Figure 32 show the response of AHS h32 and GFRP/Balsa specimens. In this case, the force-displacement curves show three peak loads. The main difference, compared with the curves recorded on the AHS h11 and GFRP PVC specimens, is observed between the top and bottom skin failure (points B and F, respectively), where the conical tup produces a local peak, due to the core crushing and the increase of contact area between the conical indenter and the specimen (Figure 31 and Figure 32, point D).

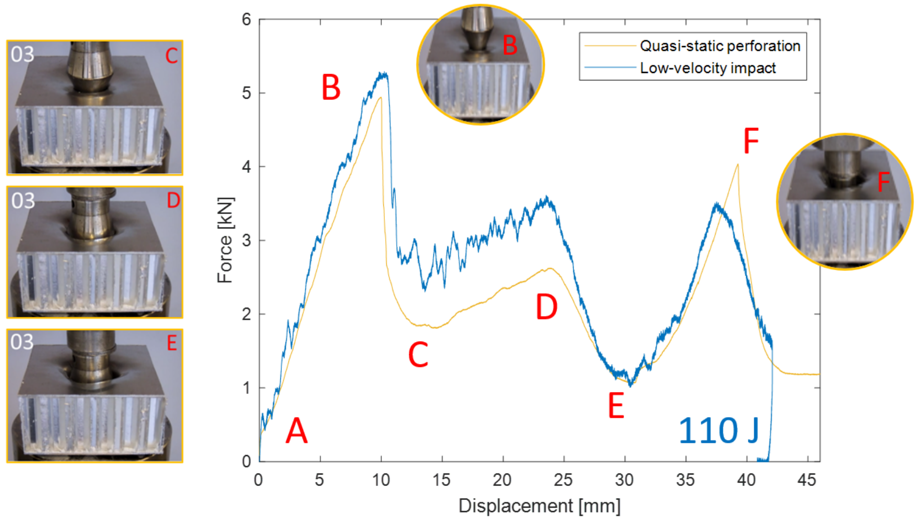

Figure 31: AHS h32 QS and LVI force-displacement responses with conical indenter [169].

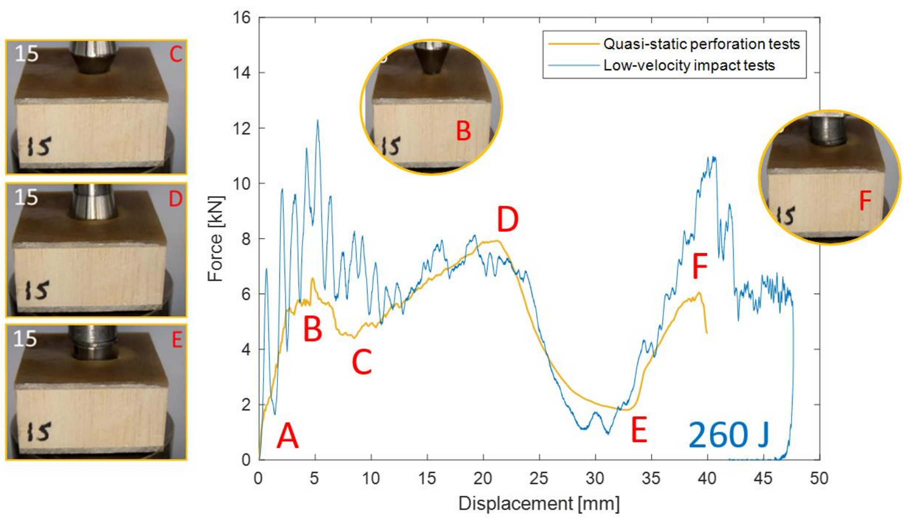

Figure 32: GFRP/Balsa QS and LVI force-displacement responses with conical indenter [169].

Under low-velocity impact, the AHS h32 response is very similar to the quasi-static trend. For GFRP/Balsa, the load trend is strongly influenced by the interaction between the indenter and the skin. Perforation energies are 110 J for AHS h32 and 260 J for GFRP/Balsa. Also in this case, the energy absorption parameters corresponding to the QS perforation and LVI tests with conical indenter are reported in Table 7 and Table 8.

Table 7: Quasi-static full perforation results with conical indenter[169].

Test	***F_{max} [kN]***	***TEA [J]***	***SEA_m [J/kg]***	***SEA_ρ [Jm^3/kg]***
QS_{avg} AHS h11	5.59	61	2541.5	0.10
QS_{avg} GFRP/PVC	4.04	85	3168.1	0.27
QS_{avg} AHS h32	4.83	99	2413.6	0.38
QS_{avg} GFRP/Balsa	8.02	198	2422.5	0.43

Comparing the test specimens with the same stiffness, it can be observed that the AHS h11 compared to the GFRP/PVC shows higher maximum load values, but 27% lower total energy absorption values. The specific energy absorption relative to mass and density are also higher in the case of the composite structure. The comparison of AHS h32 and GFRP/Balsa core shows that the values of maximum load and TEA are higher in the case of the composite structure, while SEA values are similar.

Table 8: Low-velocity impact full perforation results with H10 hemispherical indenter [169].

Test	***IKE_{test} [J]***	***F_{max} [kN]***	***TEA [J]***	***SEA_m [J/kg]***	***SEA_ρ [Jm^3/kg]***
LVI_{avg} AHS h11	65	5.97	65	2927.5	0.12
LVI_{avg} GFRP/PVC	100	6.93	100	3969	0.33
LVI_{avg} AHS h32	110	5.29	110	3000.3	0.47
LVI_{avg} GFRP/Balsa	260	12.30	260	3573.5	0.64

Comparing the TEA, SEA_m, and SEA_ρ values up to perforation under QS (Table 7) and LVI conditions (Table 8), it is evident that the dynamic values are higher than those obtained from the quasi-static tests.

3.2.3 Failure mode evaluation

The QS X-ray images of fully perforated specimens (Figure 33) reveal all the failure mechanisms observed during testing.

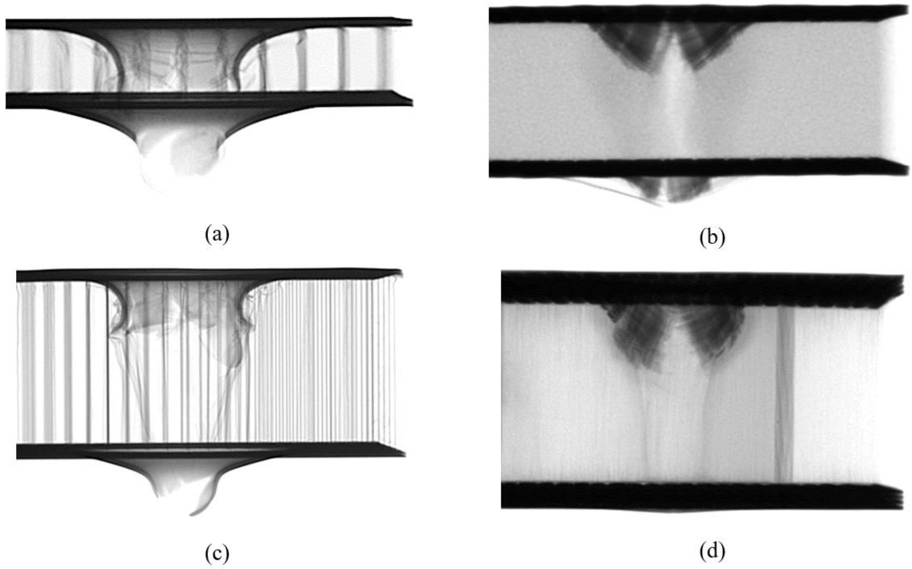

Figure 33: Radiographic results of QS tests performed at complete perforation using H10 indenter. (a) = AHS h11, (b) = GFRP PVC, (c) = AHS h32, (d) = GFRP balsa. [165]

For the thinner AHS structure (Figure 33(a)), the deformation of the top skin in the direction of load application and its subsequent perforation leads to the collapse of the honeycomb core cells due to buckling. Subsequently, deformation and perforation of the bottom skin occur. Visual inspection of GFRP/PVC specimens shows skin delamination and indentation marks on both faces, with the face failure exhibiting the characteristic cross shape typical of 0-90° fibre composites. Radiographic analysis (Figure 33(b)) confirms skin delamination and shows core perforation, densification, and breakage. Radiographic image of the thicker AHS structure (Figure 33(c)) shows very similar failure mechanisms to those previously seen for the thinner AHS, again, deformation occurs in the direction of load application and subsequent perforation of the upper skin and buckling and shear cell failure are observed in the core. GFRP/balsa specimens (Figure 33(d)) display skin delamination, core densification and subsequent failure.

Failure progression under LVI with a H10 hemispherical tup (Figure 34) closely mirrors that observed in the corresponding QS tests (Figure 33).

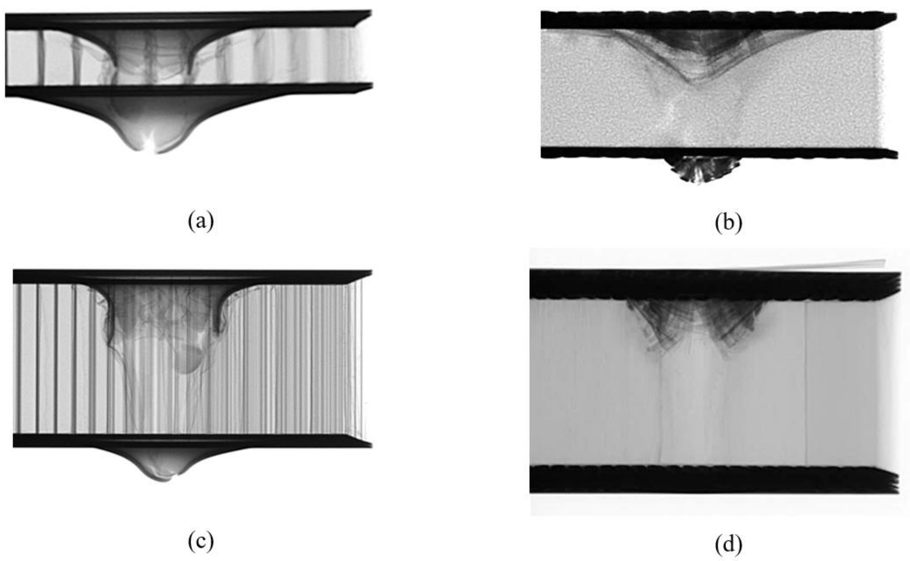

Figure 34: Radiographic results of LVI tests performed at complete perforation using H10 indenter. (a) = AHS h11, (b) = GFRP PVC, (c) = AHS h32, (d) = GFRP balsa. [165]

Radiographic investigations conducted on specimens perforated quasi-statically with the conical indenter (Figure 35) show the same damage progression as identified for those perforated with the H10 hemispherical tup (Figure 33).

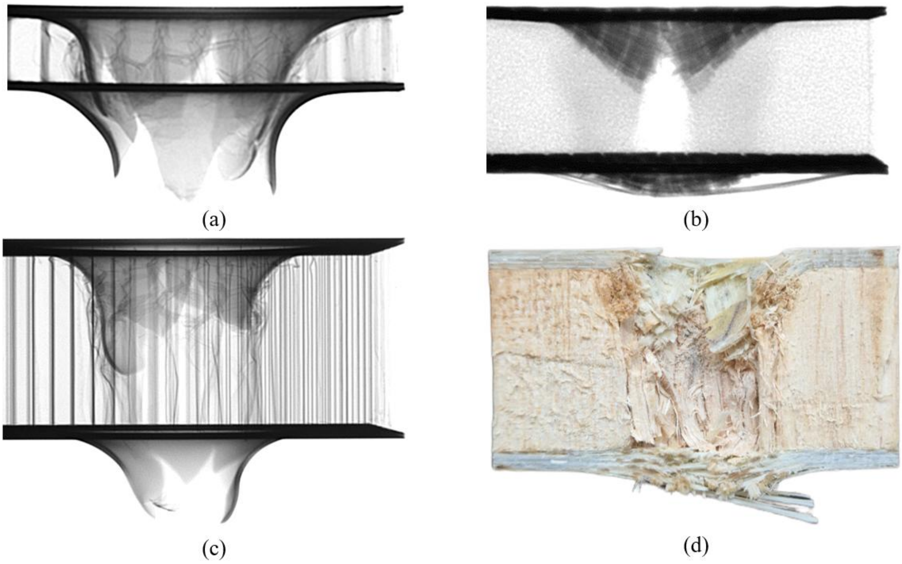

Figure 35: Radiographic and visual inspection results of QS tests performed at complete perforation using conical indenter. (a) = AHS h11, (b) = GFRP PVC, (c) = AHS h32, (d) = GFRP balsa. [165]

However, a larger damage area is suffered by the AHS h11 in Figure 35(a) and AHS h32 in Figure 35(b) specimens compared with the corresponding specimens tested with the hemispherical tup, simply due to the greater size of the conical indenter. GFRP/PVC specimens (Figure 35(c)) show skin delamination, absence of foam in the core in the direction of load application (more extensive than with the hemispherical tup), and core densification. Also, the face-ply detachment exhibits a classic cross shape. Face ply delamination was also seen via inspection of negative X-ray images. Figure 35(d) shows a simple visual inspection of the GFRP balsa specimen since radiographic inspection was not conducted in this case since the specimens had to be cut to free from the indenter. Again, the failure modes observed under LVI loading with the conical tup (Figure 36) were seen to be very similar in progression to those for the corresponding QS tests (Figure 35).

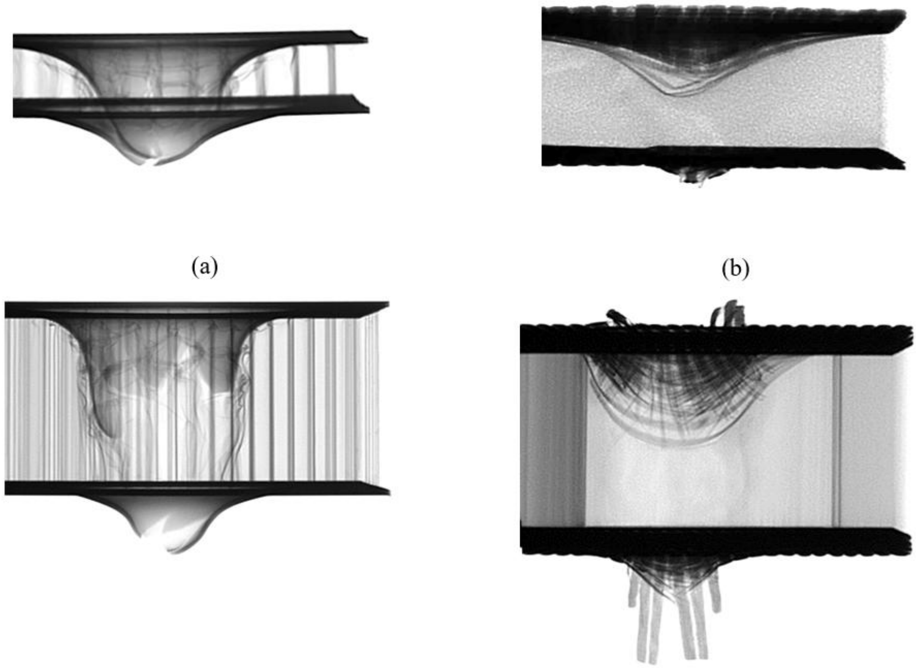

(a) (b) (c) (d)

Figure 36: Radiographic results of LVI tests performed at complete perforation using conical indenter. (a) = AHS h11, (b) = GFRP PVC, (c) = AHS h32, (d) = GFRP balsa. [165]

4. Mechanical behaviour of hybrid sandwich structures

Sandwich structures with aluminium honeycomb cores are widely used in several engineering fields, particularly in the transportation industry, due to their excellent stiffness-to-weight ratio and high energy absorption capacity. However, the use of conventional composite skins, such as GFRP, raises concerns related to disposal and environmental sustainability. Therefore, current research increasingly focuses on the development of hybrid and "green" alternatives, aiming to combine mechanical efficiency with reduced environmental impact.

In this framework, the hybridisation of aluminium honeycomb sandwich panels by introducing skins reinforced with natural or alternative fibres represents a promising strategy. This study investigates the mechanical behaviour of two hybrid configurations: the first obtained by adding two skins reinforced with flax fibres, and the second by adding skins reinforced with basalt fibres. The objective is to assess the influence of hybridisation on the flexural performance and on the low-velocity impact response of these structures, with particular attention to the mechanical properties and failure mechanisms associated with the different types of reinforcement. The results are compared with the literature, providing useful insights for the design of sustainable and high-performance composite structures.

4.1 FFRP/AHS hybrid sandwich structures

Among the sustainable alternatives to conventional composite skins, flax fibre reinforced polymers have emerged as promising candidates for hybrid sandwich structures. Flax fibres are natural, renewable, and biodegradable, offering a substantially lower environmental footprint compared to synthetic fibres, while still providing satisfactory mechanical performance. Their incorporation into aluminium honeycomb sandwich panels allows the exploration of hybrid configurations that balance structural efficiency and sustainability, in line with the growing interest in “green composites” within the transportation and engineering sectors.

This section presents the experimental investigation of FFRP/AHS panels, organized into three parts: materials and manufacturing methods, low-velocity impact tests, and three-point bending tests.

4.1.1 Materials and methods

To investigate the effect of natural fibre reinforcement on the mechanical behaviour of aluminium honeycomb sandwiches, flax fibre reinforced polymer skins were manufactured and bonded onto the surfaces of AHS panels with aluminium face sheets.

The lateral skins of the hybrid sandwich panels were made of a polylactic acid/polybutylene (adipate-co-terephthalate) PLA/PBAT blend in a 20/80 weight ratio as the matrix, reinforced with a flax fibre fabric. The matrix (*A500*, Enyax s.r.l., Buccino, Italy) contains approximately 12% by weight of micro-sized calcium carbonate particles and was originally developed for the food packaging sector. The reinforcing fabric (Composites Evolution Ltd, Chesterfield, UK) has a 2×2 Twill architecture and a surface density of 200 g/m².

Thin laminates used as skins were obtained by alternately superimposing polymer matrix films with layers of flax fabric and, finally, subjecting the stacked materials to a hot compaction process at 180 °C, applying a pre-selected pressure cycle based on previous experiences. Considering four overlapping layers of fabric, sheets approximately 1.6 mm thick were obtained.

The FFRP skins were bonded to the AHS using two commercial adhesives: a polyurethane adhesive (PU) (*SIGILL Politenace 779*, ρ_{PU} = 1130 kg/m³) and a bicomponent epoxy adhesive (ER) (*Fischer*, ρ_{ER} = 1150 kg/m³). The adhesive layer had an average thickness of 0.65 ± 0.05 mm, and curing was performed for 72 hours at room temperature.

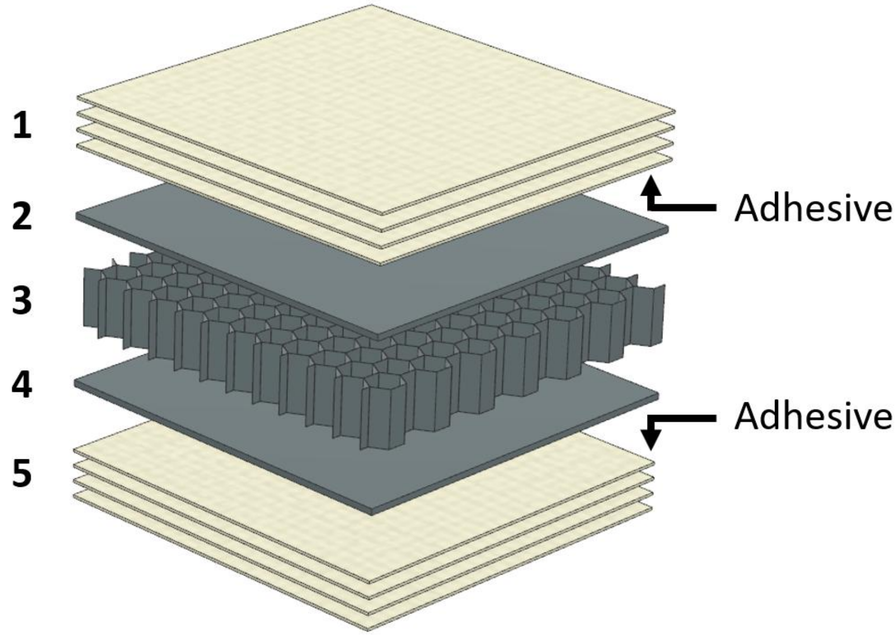

Figure 37: Lay-up of FFRP/AHS panels [170]. The numbered labels indicate the sequence of the panel constituents: (1) A500/FFRP upper skin, (2) aluminium upper skin, (3) aluminium honeycomb core, (4) aluminium lower skin, and (5) A500/FFRP lower skin.

Figure 37 shows the lay-up of FFRP/AHS panels, and Table 9 summarizes the main physical and geometrical properties.

For the LVI tests, FFRP/AHS specimens were prepared with nominal in-plane dimensions of 60 × 60 mm². The overall thickness depended on the adhesive: PU-bonded specimens were 15.67 ± 0.10 mm thick and weighed 41.72 ± 0.71 g, while ER-bonded specimens were 14.89 ± 0.07 mm thick and weighed 41.19 ± 0.45 g.

LVI tests were conducted using the impact testing machine described in Section 3.1. Two hemispherical tups were employed to investigate the effect of tup geometry: (i) a 10 mm diameter tup (Figure 21(a)) and (ii) a 20 mm diameter tup (H20), according to ISO 6630 (Figure 38). The tests were conducted using impact energies varying from 40 to 180 J, with two repetitions performed at each energy level.

Table 9: Physical and geometrical properties of the FFRP/AHS panels [170].

	Numbers of layers	**Material**	**Fibre orientation/ diameter (d) and thickness (t_c) of honeycomb cell**	**Density [kg/m^3]**	**Thickness [mm]**
Upper skins	4	A500/2x2 Twill flax	[0°/90°]	1290	1.6
	1	AA5754 H32	-	2730	1.0
Core	1	AA5052	d=6 mm t_c=0.06 mm	80	9.0
Lower skins	1	AA5754 H32	-	2730	1.0
	4	A500/2x2 Twill flax	[0°/90°]	1290	1.6

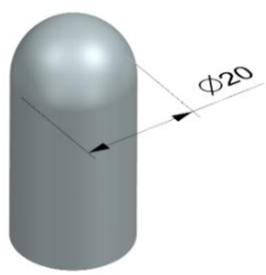

Figure 38: Hemispherical tup Ø20 (ISO 6630) [170].

Additional three-point bending tests were performed only on PU-bonded FFRP/AHS panels. The tests were carried out using the same ITALSIGMA servo-hydraulic universal testing machine employed for the QS perforation tests, equipped with a 25 kN load cell.

The flexural tests were not performed according to a specific standard, as the main objective was to investigate the damage mechanisms as a function of the support span. Therefore, the test parameters were defined to enable the observation and correlation of the different failure modes of the sandwich structure.

Supports were positioned at L = 55, 70, 80, and 125 mm, with a preload of 10 N and displacement applied at 2 mm/min. Figure 39 shows the experimental setup.

Figure 39: Three-point bending test setup for FFRP/AHS panels [170].

To quantify the energy absorption properties, the following parameters were evaluated:

- Absorbed energy [J]

$$E = \int_0^{\delta_{max}} F d\delta \tag{41}$$

- Energy absorption of the ideal absorber [J]

$$E_i = F_{max} \cdot \delta_{max} \tag{42}$$

- Energy efficiency

$$\eta = \frac{E}{E_i} \tag{43}$$

The failure modes of the FFRP/AHS panels were investigated through visual inspection, optical microscopy, digital radiography, and flash thermography.
The radiographic inspections were performed using the equipment described in Section 3.1.
The use of flash thermography for damage detection and material characterization is a well-established approach within the framework of active infrared thermography. In this technique, an external energy source, typically an intense and short optical pulse, is applied to generate a transient thermal wave that propagates through the specimen. The surface temperature evolution, recorded by an infrared camera, is subsequently analysed to evaluate local variations in thermal diffusivity associated with internal discontinuities. Since the heat diffusion rate differs between damaged and sound regions, the resulting transient temperature contrast enables the detection and quantification of subsurface defects such as delamination, debonding, cracks, or corrosion-induced damages [171]. Active infrared thermography techniques employ external excitation sources, such as optical radiation (e.g., halogen heat lamps and lasers), electromagnetic stimulation (induced eddy currents and microwaves), mechanical ultrasonic waves, or material-enabled features in composites, to generate heat in the component under inspection [172]. Techniques using optical excitation sources provide fast, contactless, and cost-effective inspection capabilities compared with more complex non-destructive evaluation systems, such as phased-array ultrasonics or X-ray computed tomography. Pulsed thermography has been successfully applied to a wide range of materials, including composites, metals, and polymers, demonstrating high efficiency and reliability in structural integrity assessment [173], [174], [175], [176].
Accordingly, a FLIR X8400sc thermal camera (Figure 40(a)) was employed, with the thermal excitation provided by a 4800 W Elinchrom Twin X4 flash unit

(Figure 40(b)) mounted on an adjustable tripod. The main specifications of the thermal camera are summarized in Table 10.

(a) (b)

Figure 40: (a) Thermal camera FLIR X8400sc; (b) Elinchrom Twin X4 flash unit.

Table 10: FLIR X8400 specifications

IR resolution	1280 x 1024 pixels
Sensor	Indium antimonide (InSb)
HD Lens	IR, focal length 28 mm IR, focal length 100 mm
Accuracy	± 1 °C
Thermal sensitivity	20mK @ 30 °C
Spectral range	1.5 - 5.1 µm
Image frequency	106 Hz (full frame)
Sensor cooling	Stirling cycle

4.1.2 Low-velocity impact test results

Low-velocity impacts are a critical loading condition for sandwich structures, as they can cause extensive internal damage while often producing only limited visible signs on the external surfaces. This hidden damage can significantly compromise the structural integrity of the panels, making early detection and analysis essential. For this reason, evaluating the impact response of FFRP/AHS panels is essential for assessing their structural reliability. This section presents the results of the experimental campaign, highlighting the effects of the adhesive type and impactor geometry on the mechanical behaviour. The force-displacement and energy-displacement curves for the specimens bonded with polyurethane and epoxy adhesives are shown in Figure 41 and Figure 42.

Specifically, Figure 41(a) and Figure 42(a) illustrate the force-displacement curves for specimens impacted at different energy levels, up to the complete perforation energy, which was equal to 180 J for both sandwich configurations (bonded with PU and epoxy adhesive) when tested with the H20 impactor. By contrast, with the H10 impactor, the perforation energy was lower, that is 125 J for the PU-bonded specimens and 100 J for the epoxy-bonded ones.

The curves exhibit the typical trend, with an initial elastic part followed by a load peak caused by contact with the first skin. After this peak, a drop of the load is usually recorded, which is followed by a second peak at higher energy levels, corresponding to contact with the second skin after the failure of the first one and of the core.

Figure 41(b) and Figure 42(b) show the energy-displacement curves obtained from impact tests at different energy levels, covering both adhesive families and impactor geometries, demonstrating that energy absorption increases progressively until total perforation occurs.

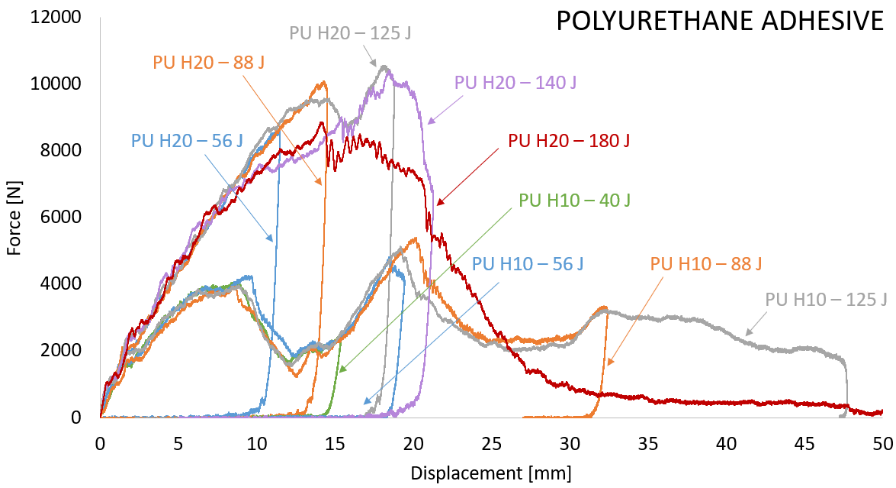

(a)

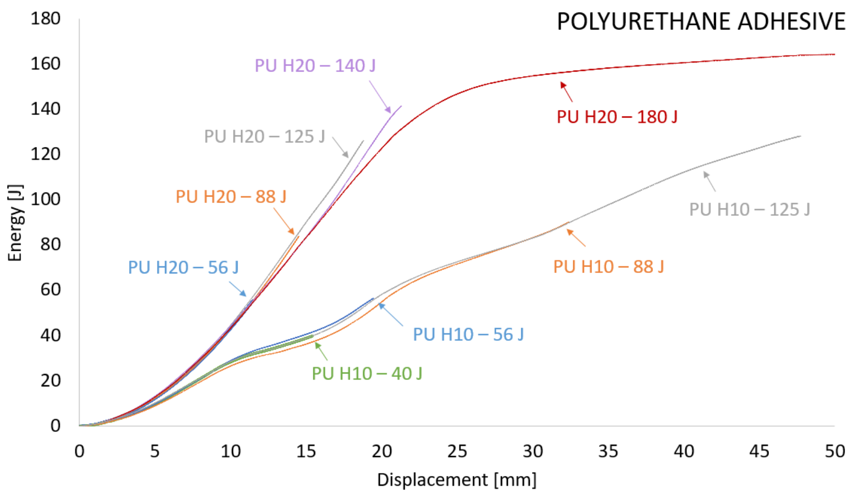

(b)

Figure 41: Impact force-displacement (a) and energy-displacement (b) curves obtained by polyurethane adhesives [170].

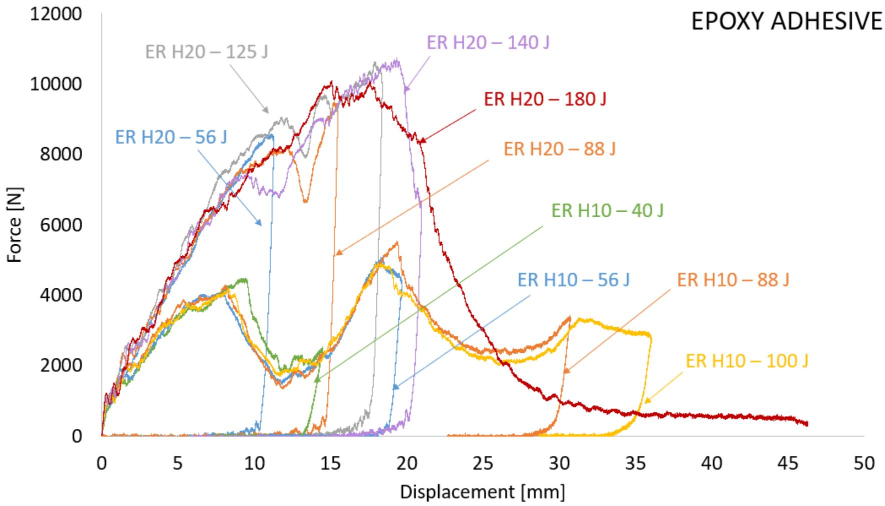

(a)

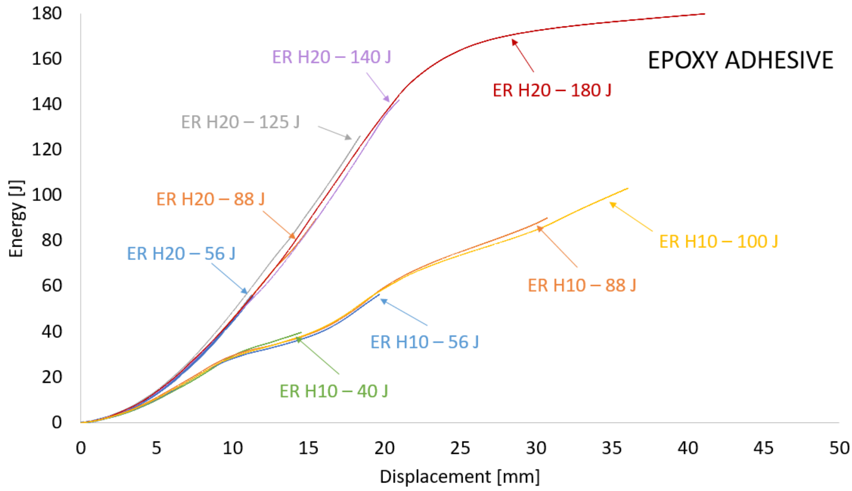

(b)

Figure 42: Impact force-displacement (a) and energy-displacement (b) curves obtained by epoxy adhesives [170].

For the tests performed with the H20 impactor on the specimens bonded by polyurethane and epoxy adhesive, at energies lower than 140 J, the energy absorption increases almost linearly with the displacement, with very narrow changes in the slope for the tests at 88 and 125 J and 140 J.

This behaviour is due, after the initial contact between the indenter and the upper skin, to the small contribution of the honeycomb core in adsorbing energy for its short height [177].

A different trend is found at 180 J, where there is an initial linear trend, a subsequent slope change, that is less than in the previous phase, due to the perforation of the lower skin. On the tests carried out with the H10 hemispherical tup, due to the geometry of the indenter, the curves trend is different from the previous case.

The curves slopes appear to be smaller, and therefore less accentuated, and the displacement values greater because of the contact between the lateral surface of the tup and the specimen. In this case, the slope changing due to the second stage [177] is still very narrow but more evident respect to the tests performed with the H20 indenter.

Overall, the results confirm that the impact performance is strongly influenced by the size and geometry of the impactor. As also reported in Table 11, the impact tests performed with the H10 tup exhibits low values of load peak, which are due to the much more severe conditions of the impactor with a smaller contact surface than the H20 one.

As it can be seen in Figure 41 and Figure 42 for the H10 impactor, very long contact time allows very important deflection of the specimens.

In the analysed specimens, this is reasonably due to the low bending stiffness of the skins [178] and to the impactor geometry (as shown Figure 21(a)).

Table 11: Results of the impact tests on the FFRP-AHS panels glued with PU and epoxy adhesives [170].

	E_{test} [J]	F_{max} [N]	TEA [J]	SEA_m [J/kg]	Density [kg/m^3]	SEA_ρ [J*m^3/kg]
PU H20 - 56J	56	8609	52	1247	747.52	0.07
PU H20 - 88J	88	10090	81	1986	724.21	0.11
PU H20 - 125J	125	10564	124	2997	723.84	0.17
PU H20 - 140J	140	10417	139	3216	770.81	0.18
PU H20 - 180J	180	8855	164	3733	785.99	**0.21**
PU H10 - 40J	40	4073	39	927	746.74	0.05
PU H10 - 56J	56	4805	55	1292	747.84	0.07
PU H10 - 88J	88	5390	88	2165	735.92	0.12
PU H10 - 125J	125	5133	125	2989	755.3	0.17
ER H20 - 56J	56	8591	53	1287	798.99	0.07
ER H20 - 88J	88	9481	88	2123	783.79	0.11
ER H20 - 125J	125	10616	123	3036	787.03	0.16
ER H20 - 140J	140	10733	140	3288	821.82	0.17
ER H20 - 180J	180	10090	180	4285	824.53	**0.22**
ER H10 - 40J	40	4483	39	933	779.67	0.05
ER H10 - 56J	56	5080	55	1330	786.53	0.07
ER H10 - 88J	88	5525	88	2140	768.73	0.11
ER H10 - 100J	100	4904	100	2473	793.57	0.13

4.1.3 Failure mode analysis

In addition to the force-displacement and energy-displacement trends, the analysis of the failure modes provides valuable insights into the damage mechanisms governing the impact response of FFRP/AHS panels. The different deflection modes due to the indenter geometry can be observed in Figure 43.

The damage analysis, performed by visual inspection, indicates that the FFRP skins can plastically deform together with the aluminium skins. The energies reported in Figure 43(b), (d), (f), and (h) (right-hand column) correspond to those required to achieve complete perforation of the bottom face as well. As shown, the impact energy is spent to deforming the skins (Figure 43) and on breaking the fibres and the matrix in a diamond shape (Figure 44) [179]. The fibre pullout mechanism and intralaminar crack [180] were also detected (Figure 45 and Figure 46).

Moreover, the ductile behaviour of the thermoplastic matrix appears to prevent delamination initiation, which was not visible. The thermogram of a tested specimen, obtained by flash thermography, is shown in Figure 47.

As highlighted in the image, the detected damage includes indentation, fibre breakage (indicated in magenta, representing colder areas due to interrupted thermal conductivity), and global bending (apparent temperature changes caused by geometric effects). Delamination and subsurface damage typically appear as hot spots, as reported in [181], which weren't detected on the impacted specimens. The impact damage is similar also for the two used adhesives, considering the H20 impactor. Some differences can be found with the H10 impactor, which causes more marked damage in the specimens glued with PU adhesive.

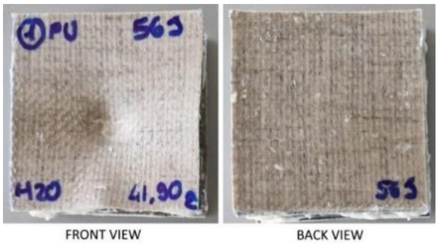

(a) PU H20_56J

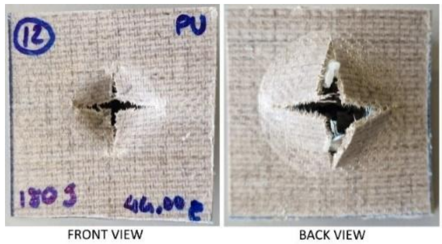

(b) PU H20_180J

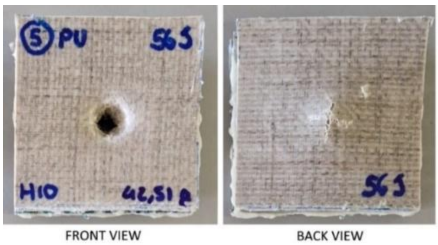

(c) PU H10_56J

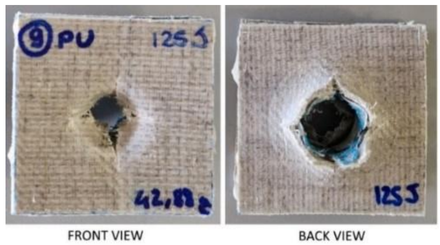

(d) PU H10_125J

(e) ER H20_56J

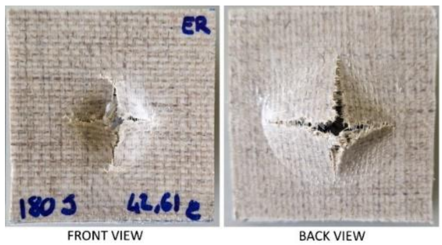

(f) ER H20_180J

(g) ER H10_56J

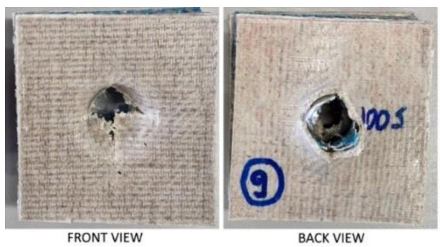

(h) ER H10_100J

Figure 43: Impact damage of the specimens [170]. The adhesive is the PU type, and the impactors were H20 in (a) and (b); H10 in (c) and (d). The adhesive is the epoxy type, and the impactors were H20 in (e) and (f); H10 in (g) and (h).

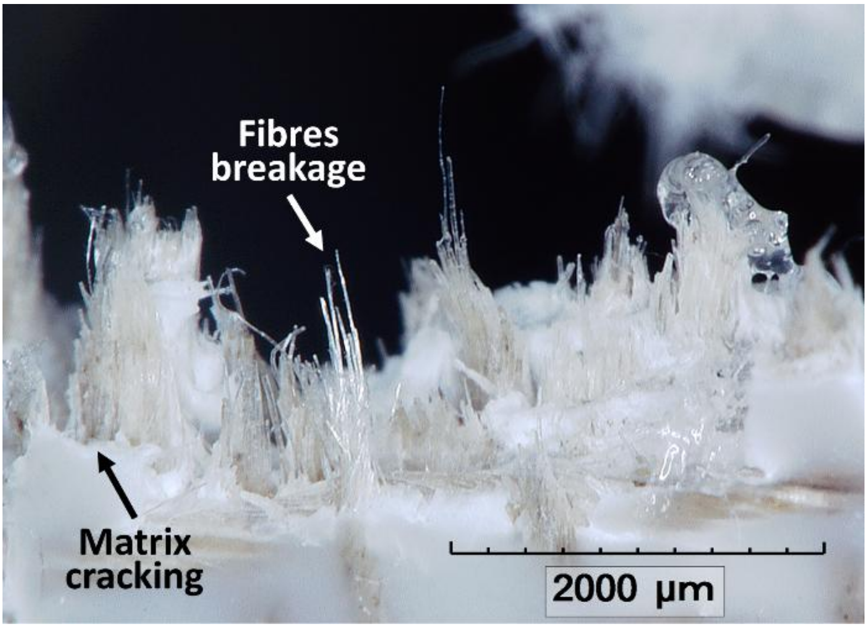

Figure 44: Fibre breakage and matrix cracking in the FFRP skin [170].

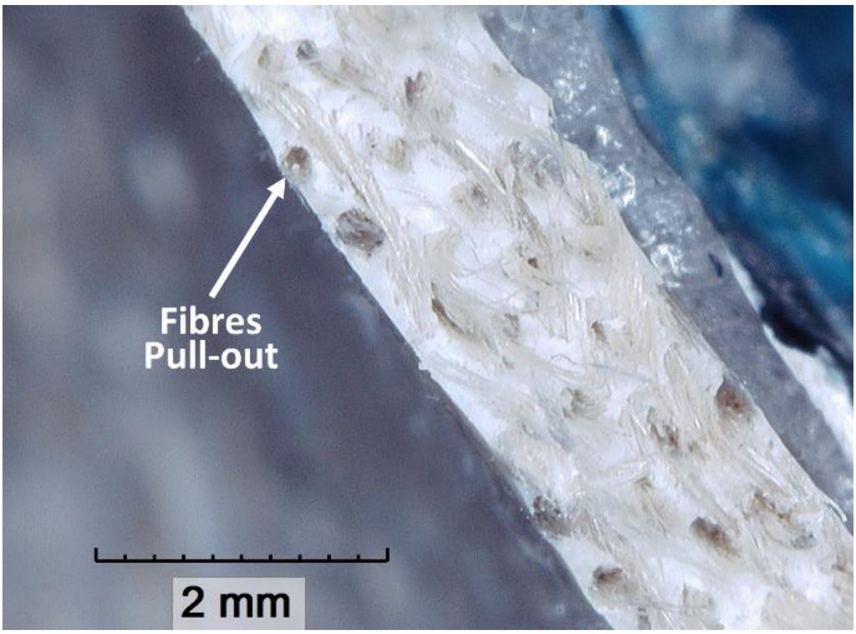

Figure 45: Fibre pullout in the FFRP skin [170].

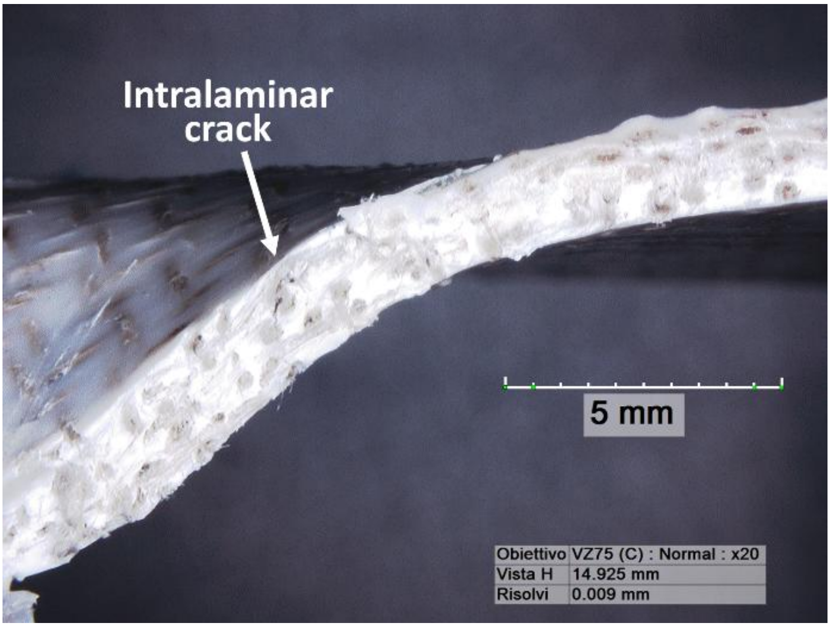

Figure 46: Interlaminar crack in the FFRP skin [170].

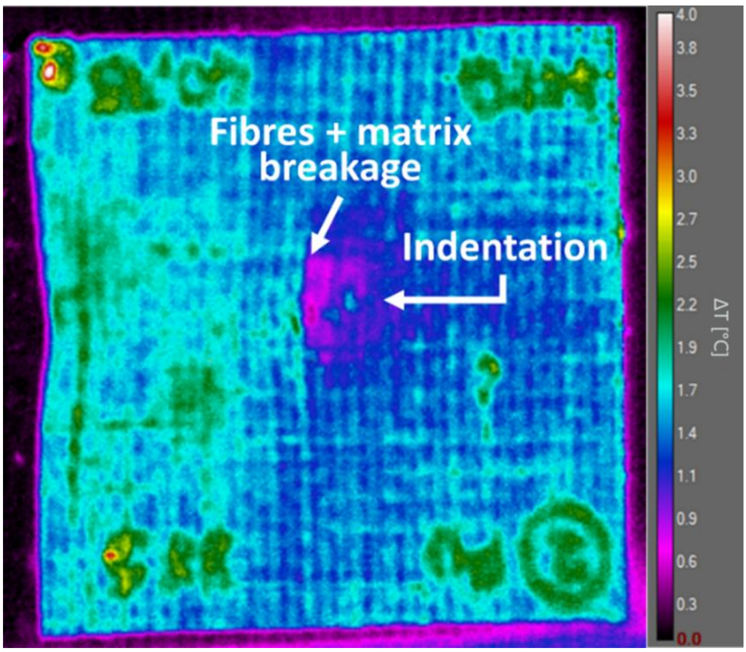

Figure 47: Thermogram of a tested specimen [170].

Digital radiography was used to further investigate the failure mechanisms, with the results presented in Figure 48.

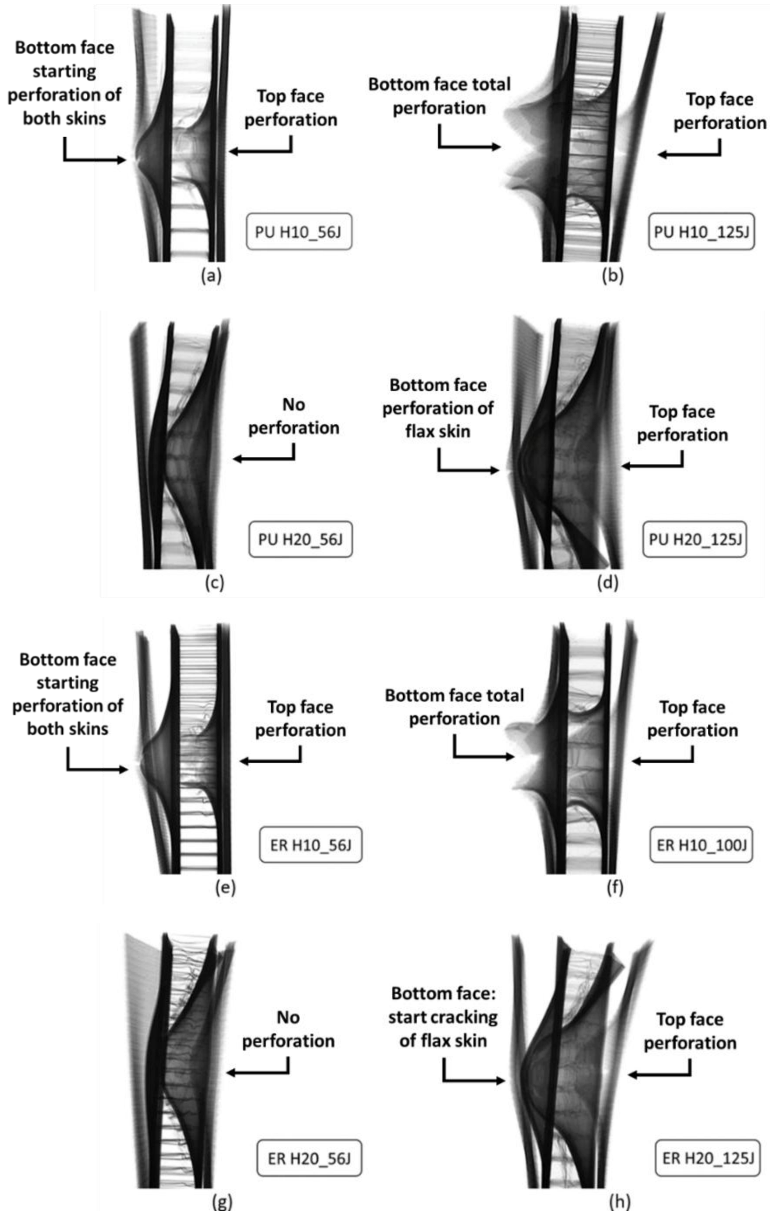

Figure 48: Radiographic inspection of the impacted specimens [170]. The adhesive is the PU type in (a), (b), (c) and (d). ER type in (e), (f), (g) and (h).

Indicating with: NP = no perforation, BFP = bottom face perforation and TFP= top face perforation, Figure 49 summarizes the failure behaviour of the impacted specimens.

This behaviour confirms that the H10 indenter represents the worst-case scenario, as complete perforation of the specimen is achieved at an early impact energy of 56 J, whereas no face-sheet perforation occurs at the same energy with the H20 tup. In contrast, with the H20 indenter, top skin perforation occurs at 88 J for both types of specimens. By increasing the impact energy to 180 J, it is possible to notice the breaking of the bottom flax reinforced skin, which leads to greater loads in the specimens bonded with epoxy adhesive.

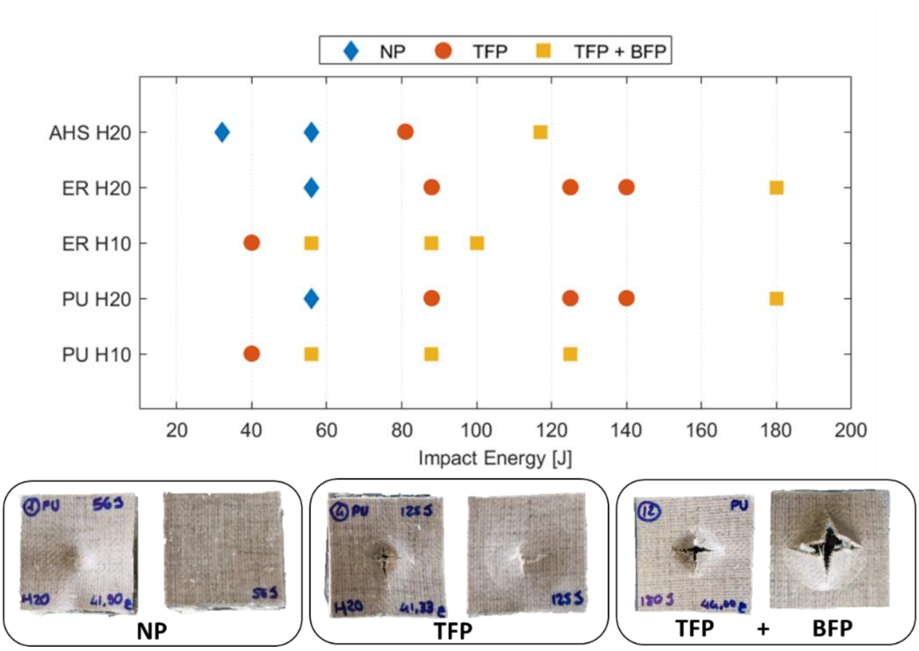

Figure 49: Failure modes comparison of the LVI samples [170].

4.1.4 Limit load prediction

Considering that the top face perforation occurred at 88 J for all hybrid sandwich, a theoretical model developed by Crupi et al. [108], [109] for the prediction of the limit load, was applied for the specimens impacted with the H20 indenter. The prediction of the limit load is expressed by:

$$P_f = P_{faceplate\_stretching} + P_{core\_crushing} + P_{core\_tearing} = 2\sqrt{2}\pi R_e A_{11}(\epsilon_{crdf})^{\frac{3}{2}} + \pi K_c R_e^2 \sigma_{ycd} + 2\pi R_e \gamma_c \quad (44)$$

The parameters reported in Eq. 44 are summarized in Table 12.

Table 12: Parameters used in the theoretical model (hemispherical tup Ø20 mm)

Symbol	Definition	Aluminium	FFRP skins
R_e	Effective radius of the hemispherical nose impactor	R_e = 0.4 [109]	
K_c	Constraint factor, resulting from the fact that the core under the indenter is constrained by the surrounding material	Average value of K_c = 2 [109]	
A_{11f}	Matrix coefficient of the dynamic extensional stiffness of the face-sheet	82418 MPa [109]	22210 MPa [this study]
ε_{crdf}	Dynamic tensile fracture strain of the face-sheet	0.02 [109]	0.021 [this study]
σ_{ycd}	Dynamic crushing strength of the core	2 MPa [109]	-
γ_c	Tear energy of the foam	6.7 kJ/m^2 [109]	-

The dynamic extensional stiffness A_{11f} for the flax skins was obtained with the lamination theory by using Hyperlaminate tool available in Altair Hyperworks® software. The value of the static tensile fracture strain of the skin εcrdf was calculated from experimental tests. For calculating the tensile and shear moduli of the single lamina the rule of mixtures was employed, and the mechanical properties of the flax fibres and of the blend components were taken from previous research papers [182], [183], [184], [185], [186], [187].

The model was able to predict the load failure with an error of 12% (11123 N vs. 9786 N, obtained as the average value of the top face-sheet perforation experimental load for the specimens glued by epoxy resin and polyurethane adhesive reported in Table 11, Section 0). The contribution of the aluminium skin was considered by superimposing its faceplate stretching.

4.1.5 Three-point bending test results and failure mode analysis

Three-point bending tests were performed to evaluate the flexural response of the FFRP/AHS panels under QS loading.

Figure 50 shows the load-deflection curves obtained from these tests. The results show that the mechanical behaviour in bending conditions is strongly affected by the support span distance. Indeed, for lower values of support span distance, the bending strength is higher than the largest one (125 mm). At L = 55 mm the efficiency of the sandwich panel is also higher (Table 13).

Table 13: Results of the three-point bending tests [170].

	L [mm]	**F_{max}** [kN]	**δ_{max}** [mm]	**E** [J]	**E_i** [J]	**η** [%]
L55	55	2.86	13.25	29.83	37.93	79
L70	70	2.70	16.54	35.80	44.69	80
L80	80	2.02	18.69	24.21	37.81	64
L125	125	1.95	19.54	20.81	38.00	55

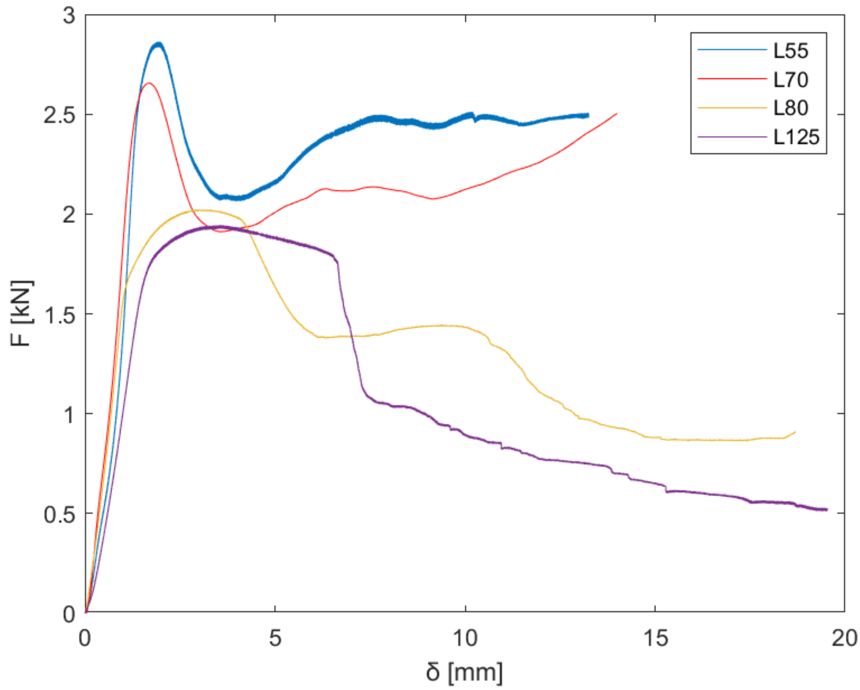

Figure 50: Load-deflection curves obtained by three-point bending test [170].

The trend of the curves suggest that different damage mechanisms were triggered during the test, as at L = 55 and 70 mm the load, after reaching the highest value, has a sudden drop, followed by a certain damage tolerance which causes a load increment. For L = 80 and 125 mm, a short load plateau occurs after the peak, followed by a gradual and continuous decrease. The slope of the decrease is steeper for L = 125 mm, indicating more severe damage in the panel. The failure modes were further investigated using visual inspection and digital radiography, which allowed a detailed detection of the different bending behaviours.

The images in Figure 51 show that for L = 55 and 70 mm, the panels fail primarily by indentation, which explains the load recovery after the peak due to local densification of the core under the applied cylinder. In this case, the damage is highly localized. For L = 80 and 125 mm, failure is dominated by core-shear, leading to extensive damage of the core and debonding from the bottom skin. It is worth noting that the debonding between FFRP and aluminium face-sheets is very narrow.

Figure 51: Failure modes of the specimens subjected to bending loads [170].

The indentation failure mode is better explained in Figure 52(a) and Figure 52(b), where is put in evidence not only that the cells involved in the damage collapsed by buckling, but also the densification, highlighted by the higher grey level recorded in the area below the cylinder. The radiography of the specimen tested at L = 80 mm (Figure 52(c)) also reveals a simultaneous presence of both failure modes: indentation and core-shear.

Therefore, this support span can be considered a borderline condition where indentation is still observed. At L = 125 mm (Figure 52(d)), only core-shear failure is present. The damage is extensive, causing an asymmetric deformation and the formation of plastic hinges.

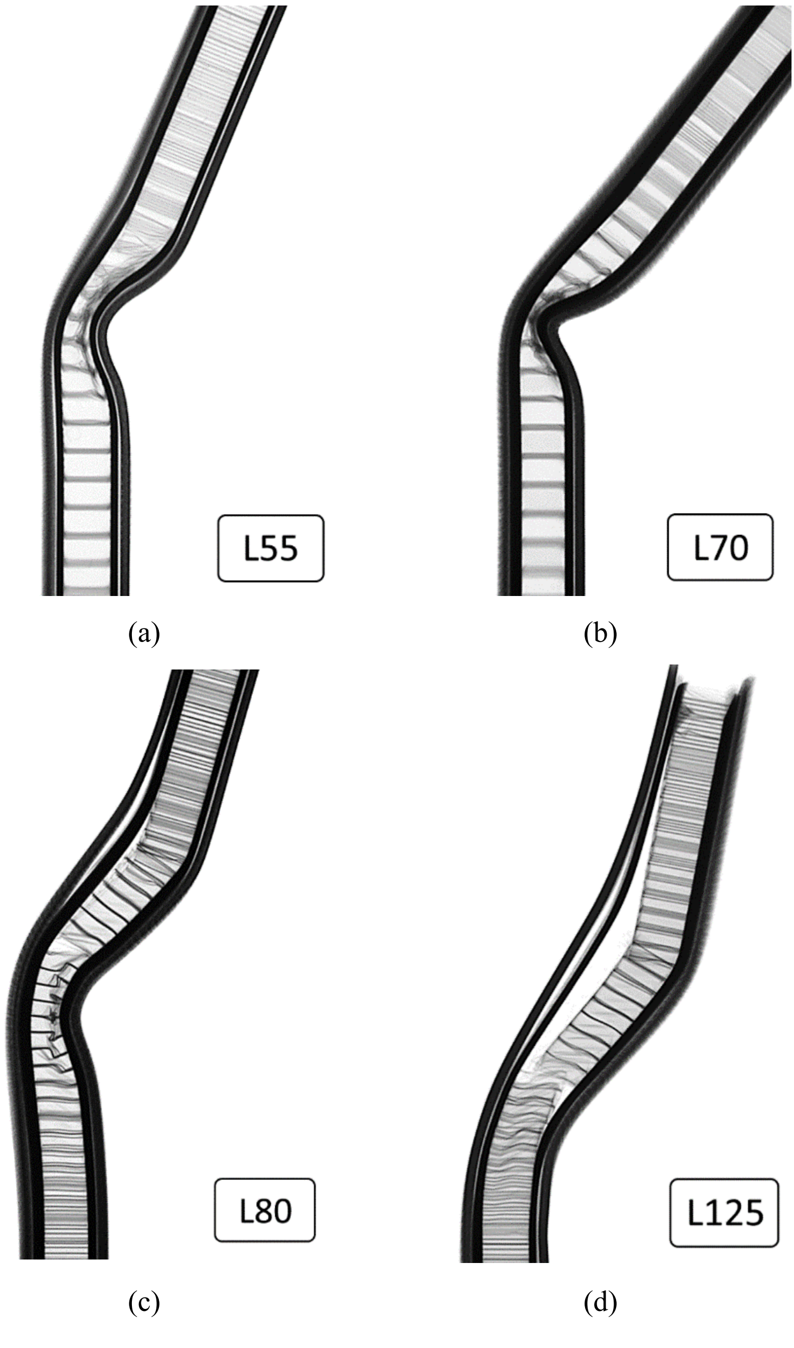

Figure 52: Digital radiography of the specimens subjected to bending loads allowed to detect internal damage [170].

4.2 BFRP/AHS hybrid sandwich structures

Basalt fibre reinforced polymers (BFRP) represent an effective compromise between mechanical performance and environmental sustainability in the field of hybrid sandwich structures. Basalt fibres are produced by melting volcanic rocks, providing a mineral-based reinforcement derived from abundant natural resources and relatively straightforward processing. Their high tensile strength, good thermal and chemical resistance, and intrinsic fire performance make them attractive for structural applications requiring durability and safety, while offering a lower environmental footprint than glass or carbon fibres [19].

Combining BFRP skins with aluminium honeycomb cores enables the development of hybrid configurations with improved structural efficiency.

This section presents the experimental investigation on hybrid BFRP/AHS panels bonded with a commercial polyurethane adhesive. The discussion is organized into three parts: materials and methods, QS perforation tests, and LVI tests.

4.2.1 Materials and methods

Basalt fibre reinforced polymer skins were fabricated and bonded to aluminium honeycomb sandwich panels to prepare the specimens for the experimental campaign. The skins were made by alternately stacking polyamide (PA12) films and plain basalt fabric layers, followed by consolidation through hot pressing. The PA12 films were prepared from a waste powder supplied by a company, originally SINTERIT PA12 Industrial Fresh (bulk density 505 kg/m^3) intended for Selective Laser Sintering. After pre-drying at 80 °C in a vacuum oven for 4 hours, the powder was transformed into films using a COLLIN P400E hydraulic press at 245 °C. The pressing cycle consisted of 2 minutes at 0 bar, 2 minutes at 10 bar and 1 minute at 20 bar. Once cooled to room temperature under a maximum pressure of 20 bar, films approximately 250 μm thick were obtained.

The composite skins were then produced by combining four plies of plain basalt fabric (Incotelogy GmbH, 210 g/m²) with the PA12 films in the same hydraulic press at 245 °C, following a pressure cycle of 3 minutes at 5 bar, 3 minutes at 10 bar, and 3 minutes at 15 bar.

Table 14 reports the main physical and geometrical properties of the BFRP/AHS panels, and Figure 53 illustrates the lay-up of the panels.

Table 14: Physical and geometrical properties of the BFRP/AHS panels.

	Numbers of layers	**Material**	**Fibre orientation/ diameter (d) and thickness (t_c) of honeycomb cell**	**Density [kg/m^3]**	**Thickness [mm]**
Upper skins	4	PA12/Basalt	[0°/90°]	1190	1.5
	1	AA5754 H32	-	2730	1.0
Core	1	AA5052	**Type 1**: d=6 mm t_c=0.06 mm 	**Type 1**: 80	9.0
			Type 2: d=3 mm t_c=0.05 mm 	**Type 2**: 130	
Lower skins	1	AA5754 H32	-	2730	1.0
	4	PA12/Basalt	[0°/90°]	1190	1.5

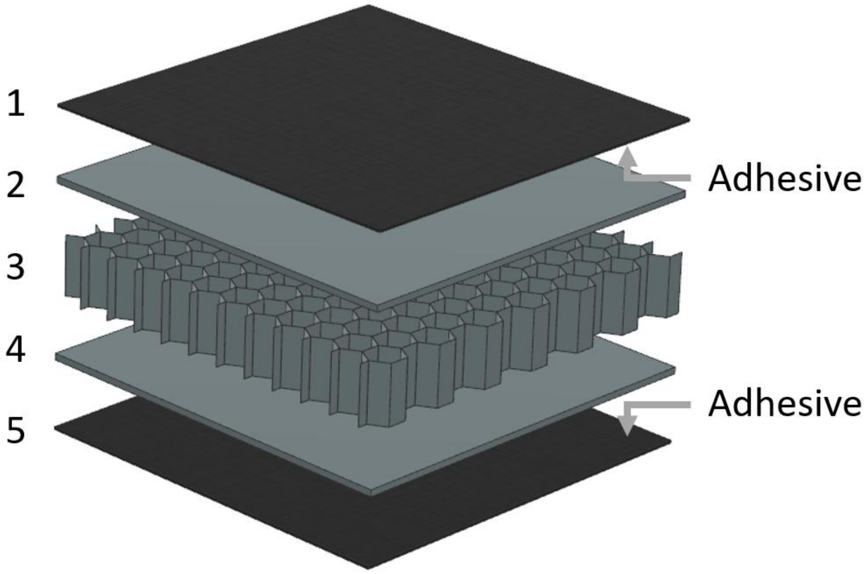

Figure 53: Lay-up of BFRP/AHS panels. The numbered labels indicate the sequence of the panel constituents: (1) PA12/BFRP upper skin, (2) aluminium upper skin, (3) aluminium honeycomb core, (4) aluminium lower skin, and (5) PA12/BFRP lower skin.

BFRP/AHS specimens were manufactured with nominal in-plane dimensions of 60 × 60 mm². Two different types of aluminium honeycomb core were employed, with 3 mm and 6 mm honeycomb cell diameters. Table 15 reports the corresponding measured average mass and density for these specimens, including standard deviations.

Table 15: Measured average mass and density of BFRP/AHS specimens

	Mass [g]	**Density [kg/m^3]**
BFRP/AHS d3	41.68 ± 1.46	826.88 ± 28.90
BFRP/AHS d6	39.09 ± 1.00	775.55 ± 19.88

The BFRP skins were bonded onto the aluminium sandwich panels using a single-component polyurethane adhesive, TEKNICA U2®, with the following properties:

- Final curing time ≈ 30 minutes

- ρ = 1460 kg/m³
- Shear strength under tensile load (EN 204 – D1) ≥ 10.5 N/mm²
- Shear strength under tensile load (EN 204 – D4) > 4.5 N/mm²
- Chemical resistance: Excellent
- Water and humidity resistance: Excellent (DIN EN 204 D4)

To investigate the mechanical performance of the BFRP/AHS hybrid sandwich panels, QS perforation and LVI tests were carried out, using the testing machines described in Section 3.1. In both QS perforation and LVI tests, the H20 hemispherical tup was employed. For the LVI tests, impact energies ranged from 180 to 250 J, with two repetitions performed at each energy level.

The failure modes of the BFRP/AHS panels were systematically investigated through digital radiography and flash thermography (the radiographic and flash thermographic equipment are described in Section 3.1 and Section 4.1.1, respectively).

4.2.2 Quasi-static perforation test results

QS perforation tests are widely used to evaluate the resistance of sandwich panels to concentrated loading and to identify the onset and progression of failure mechanisms. To assess the benefits of hybridization, the tests were conducted on both BFRP/AHS hybrid panels and the reference unreinforced aluminium honeycomb sandwich panels. The force-displacement curves, shown in Figure 54 and Figure 55 for BFRP/AHS d3 and BFRP/AHS d6, respectively, present the mechanical response of both panel types under QS loading. The force-displacement curves of the BFRP/AHS d3 hybrid panels exhibit an initial linear stage, where the load increases proportionally with displacement until reaching a first peak. This peak corresponds to the failure of the top skin, which causes a sudden load drop. Subsequently, the indentation of the core leads to a second load increase associated with the contact of the indenter with the bottom skin, producing a new peak before its perforation. Once the bottom skin is penetrated, the load sharply decreases.

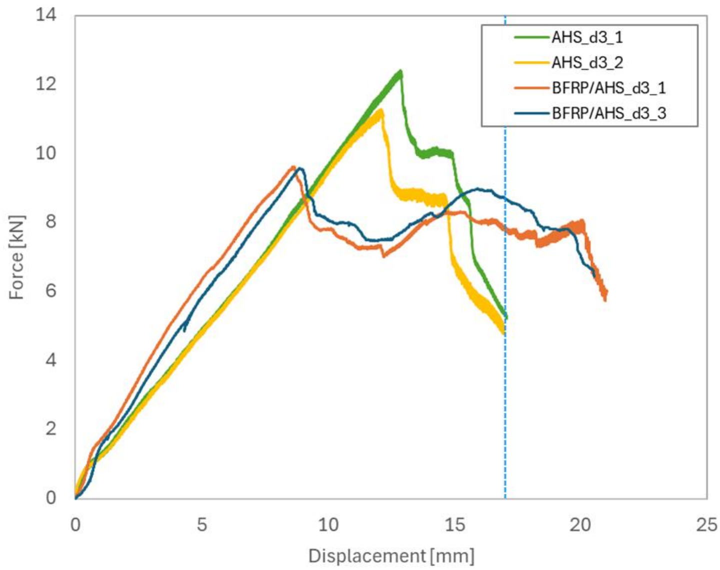

Figure 54: Force-displacement curve from the QS perforation test of the BFRP/AHS d3 hybrid panel and the reference AHS panel.

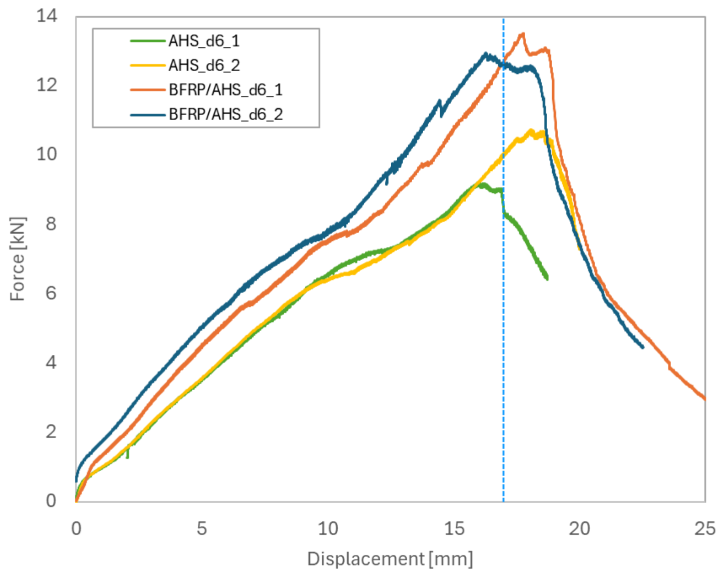

Figure 55: Force-displacement curve from the QS perforation test of the BFRP/AHS d6 hybrid panel and the reference AHS panel.

When compared with the unreinforced AHS panels, the hybrid specimens exhibit lower peak loads, while the AHS specimens show a more extended plastic deformation region.
A similar general trend is observed in the BFRP/AHS d6 panels. In this case, the linear region is significantly wider than in the 3 mm configuration: while the first peak in the BFRP/AHS d3 panels occurs at a displacement of approximately 9 mm, in the BFRP/AHS d6 panels it is delayed to approximately 17 mm. In this case, the plastic deformation phase is much more limited.
Overall, both hybrid configurations exhibit higher stiffness compared to the unreinforced AHS panels, highlighting the contribution of the BFRP skins to the initial stiffness of the sandwich panels.

Table 16: QS perforation results for BFRP/AHS.

	Provino n°	**F_{max} [kN]**	**δ_{Fmax} [mm]**	**δ_{max} [mm]**	**TEA $_{(\delta=17mm)}$ [J]**	**SEA$_{\rho\ (\delta=17mm)}$ [J*m^3/kg]**
AHS d3	**1**	12.7	12.9	17.1	116.6	0.20
	2	12	12.2	17	106.8	0.18
BFRP/AHS d3	**1**	9.7	8.6	21.0	112	0.13
	3	9.6	8.9	20.6	112	0.14
AHS d6	**1**	9.2	16.0	18.7	90.2	0.17
	2	10.9	18.1	20.0	90.2	0.16
BFRP/AHS d6	**1**	13.5	17.8	29.8	110.2	0.15
	2	13	16.3	22.5	121.1	0.16

In addition, Table 16 reports the main quantitative results obtained from the QS perforation tests, including the maximum load, displacement at maximum load, maximum displacement, total absorbed energy, and specific absorbed energy normalized by the panel density. The energy absorption parameters were calculated at a common displacement of 17 mm (light blue line), allowing a direct comparison between the BFRP/AHS hybrid panels and the reference AHS panels. The QS perforation test results provide a clear indication of the effect of hybridization on the energy absorption behaviour of the panels. For the BFRP/AHS d3 panels, he TEA of the hybrids is similar to that of the unreinforced AHS panels, while the SEA is about 30% lower due to the increased density from the BFRP skins. For the BFRP/AHS d6 panels, the hybrids exhibit higher TEA, but the SEA remains slightly lower (around 6% lower) than the reference panels, again because of the increased density. These results indicate that hybridization enhances the total energy absorption, while the specific energy per unit density can decrease due to the added mass of the reinforcing skins.

The panel stiffness K was evaluated from the initial linear portion of the load-displacement curve using the following formula:

$$K = \frac{\Delta F}{\Delta \delta} \tag{45}$$

where ΔF is the change in force and Δδ is the corresponding displacement change. The stiffness values are showed in Table 17.

Table 17: Stiffness (K) of BFRP/AHS panels, calculated from the initial linear part of the force-displacement curves obtained in QS perforation tests.

	K [N/mm]
AHS d3	905
BFRP/AHS d3	1204
AHS d6	655
BFRP/AHS d6	832

The stiffness of the BFRP/AHS d3 and d6 panels increases by approximately 33% and 27%, respectively, compared to the unreinforced AHS panels. During the QS perforation tests, a video camera was positioned to record the entire duration of each test. Synchronization between the start of the test and the beginning of the recording was achieved using a manual trigger. This setup allowed the correlation of the force-time curves with the corresponding video frames, providing visual insight into the failure progression of the specimens. Figure 56 and Figure 57 show the analysis performed on the BFRP/AHS d3 and d6 panels, respectively.

For the BFRP/AHS d3 hybrid specimen, the first force peak, corresponding to the perforation of the top skin, occurs at 107 s, with an indenter displacement of 8.63 mm. The final peak is observed at 242 s, with an indenter displacement of 20 mm. From the analysis of the last peak, the out-of-plane displacement of the skins before failure is 6.01 mm. Local debonding is indicated in the curve by a red asterisk.

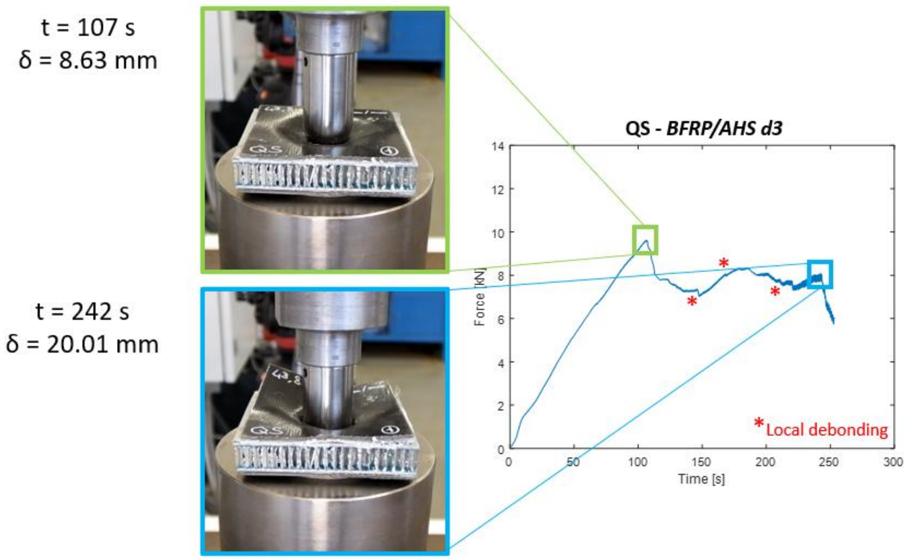

Figure 56: Force-time curve of the BFRP/AHS d3 panel, correlated with synchronized video frames showing failure progression

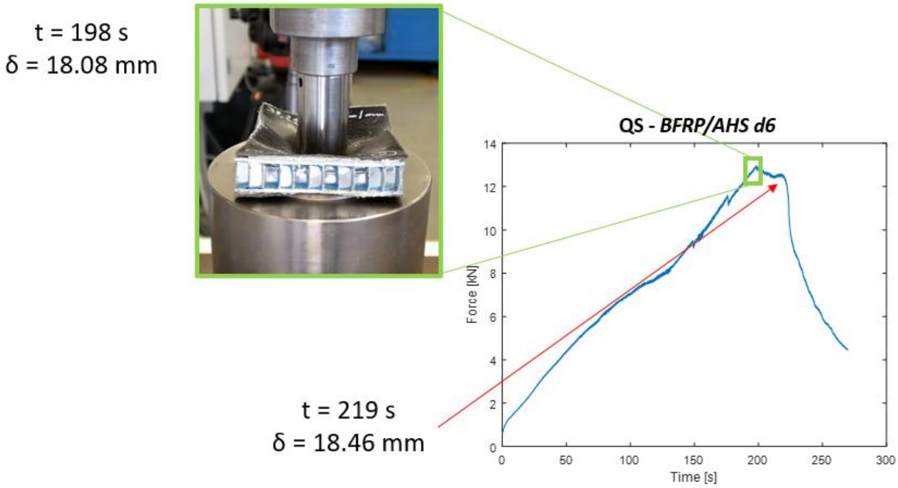

Figure 57: Force-time curve of the BFRP/AHS d6 panel, correlated with synchronized video frames showing failure progression.

For the BFRP/AHS d6 specimen, the first force peak occurs at 198 s, approximately twice the time observed for the BFRP/AHS d3 panel, corresponding to an indenter displacement of 18.08 mm. The second peak is reached shortly afterwards, at 219 s. In this case, the out-of-plane displacement is considerably higher, since the entire specimen deforms by bending.

4.2.3 Low-velocity impact test results

Low-velocity impacts represent a critical loading scenario for sandwich structures. Evaluating the impact response of BFRP/AHS panels is therefore essential to understand their mechanical performance and structural integrity.

The LVI test results are presented in Figure 58 and Figure 59, showing the force-displacement curves for BFRP/AHS d3 and d6 panels, respectively.

The trend is similar to that observed in Section 4.2.2, but with higher peak loads due to the dynamic effects of impact. The curves exhibit the typical behaviour of sandwich panels under concentrated impact: an initial linear region, followed by a first peak corresponding to the contact with the top skin. After this peak, a load drop occurs, followed by a second peak associated with the contact of the indenter with the bottom skin, prior to its perforation.

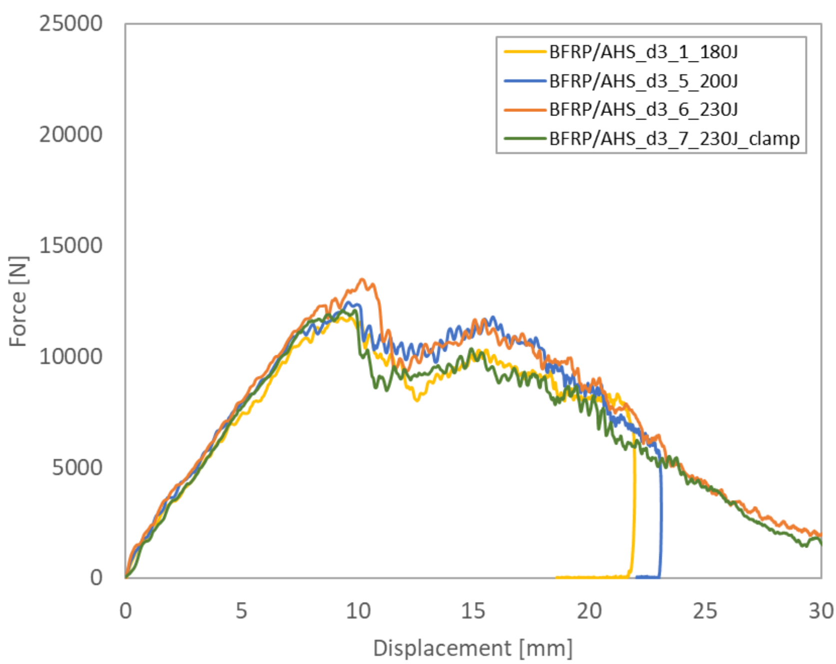

Figure 58: LVI force-displacement curves for BFRP/AHS d3

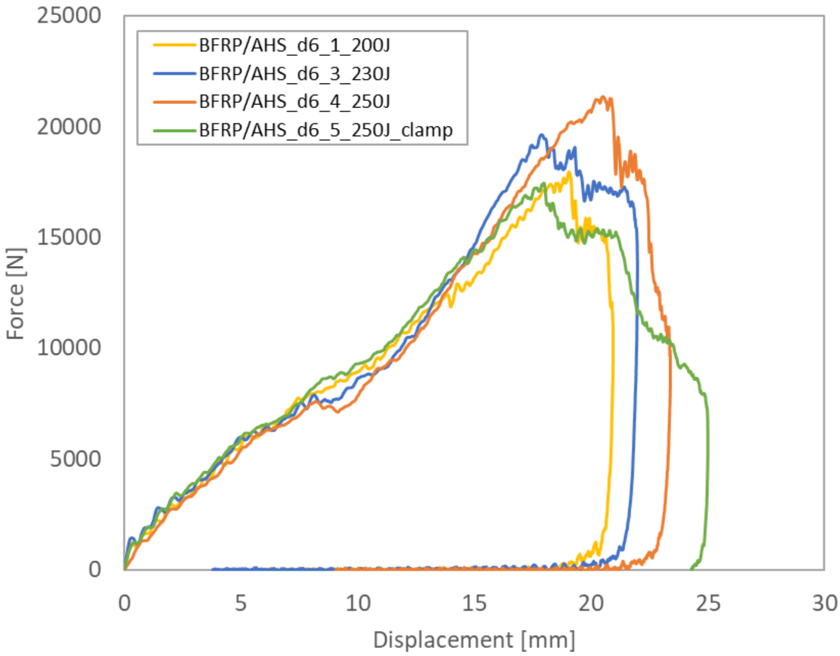

Figure 59: LVI force-displacement curves for BFRP/AHS d6

Impact test results for BFRP/AHS panels are summarized in Table 18, including peak force, maximum displacement, total absorbed energy (TEA), and specific absorbed energy (SEA) normalized by panel density. Both maximum load and energy absorption are higher for the BFRP/AHS d6 panels. Additionally, the table presents a summary of the observed failure modes: top face perforation (TFP), bottom face perforation (BFP), and total penetration (TP). These data provide a basis for comparing the mechanical response and energy absorption behaviour of the hybrid panels under low-velocity impact.

Considering the impact response at comparable damage levels, the combined top and bottom face perforation (TFP + BFP) occurs at 200 J for the BFRP/AHS d3 specimens, whereas for the BFRP/AHS d6 specimens the same damage condition is reached at 250 J, i.e., 50 J higher. Examining the corresponding peak forces, the 3 mm panels reach about 13 kN, while the 6 mm panels reach 21 kN under the same damage state. In terms of specific absorbed energy (SEA) normalized by panel density, the 3 mm panels exhibit 0.24 Jm^3/kg, whereas the 6 mm panels reach 0.32 Jm^3/kg, further highlighting the superior energy absorption efficiency of the larger cell configuration.

Table 18: LVI results for BFRP/AHS.

	Specimen n°	**E_{test} [J]**	**F_{max} [kN]**	**TEA [J]**	**SEA_ρ [J m^3/kg]**	**Damage**		
						TFP	**BFP**	**TP**
BFRP/AHS d3	**1**	180	11.8	179	0.22	X	-	-
	5	200	12.5	200	0.24	X	X	-
	6	230	13.5	230	0.26	X	X	X
	7 (clamp)	230	12.1	226	0.26	X	X	X
BFRP/AHS d6	**1**	200	18	198	0.26	X	-	-
	3	230	19.6	227	0.29	X	-	-
	4	250	21.4	248	0.32	X	X	-
	5 (clamp)	250	17.4	250	0.32	X	X	-

The stiffness of the BFRP/AHS panels under low-velocity impact was evaluated using Eq. (45). The resulting values are reported in Table 19.

Table 19: Stiffness (K) of BFRP/AHS panels, calculated from the initial linear part of the force-displacement curves obtained in LVI tests.

	K [N/mm]
BFRP/AHS d3	1401
BFRP/AHS d6	926

The stiffness of the BFRP/AHS panels measured during low-velocity impact is higher than that observed in QS tests, reflecting the strain-rate sensitivity of the fibres and the polymer matrix, which respond more rigidly under rapid deformation.

4.2.4 Failure mode evaluation

To investigate the failure mechanisms of the BFRP/AHS hybrid panels under QS loading, Figure 60 shows a BFRP/AHS d3 specimen (a) and a BFRP/AHS d6 specimen (b) after testing. Visual inspection highlights both common and distinct failure features between the two configurations.

Figure 60: Visual inspection of failed BFRP/AHS panels after QS perforation: (a) BFRP/AHS d3 specimen, (b) BFRP/AHS d6 specimen.

Both panels exhibit indentation, local debonding between the BFRP skins and the aluminium skins, and the typical cross-shaped fibre breakage characteristic of 0°/90° laminate composites.

The BFRP/AHS d3 specimen shows a localized response, with failure concentrated around the indentation area. In contrast, the BFRP/AHS d6 panels exhibits a wider spread of damage, with folding and large deflection of the skins and core extending towards the panel edges. These differences highlight the influence of cell size on load redistribution and failure progression under impact loading.

Figure 61 and Figure 62 show BFRP/AHS panels tested under low-velocity impact.

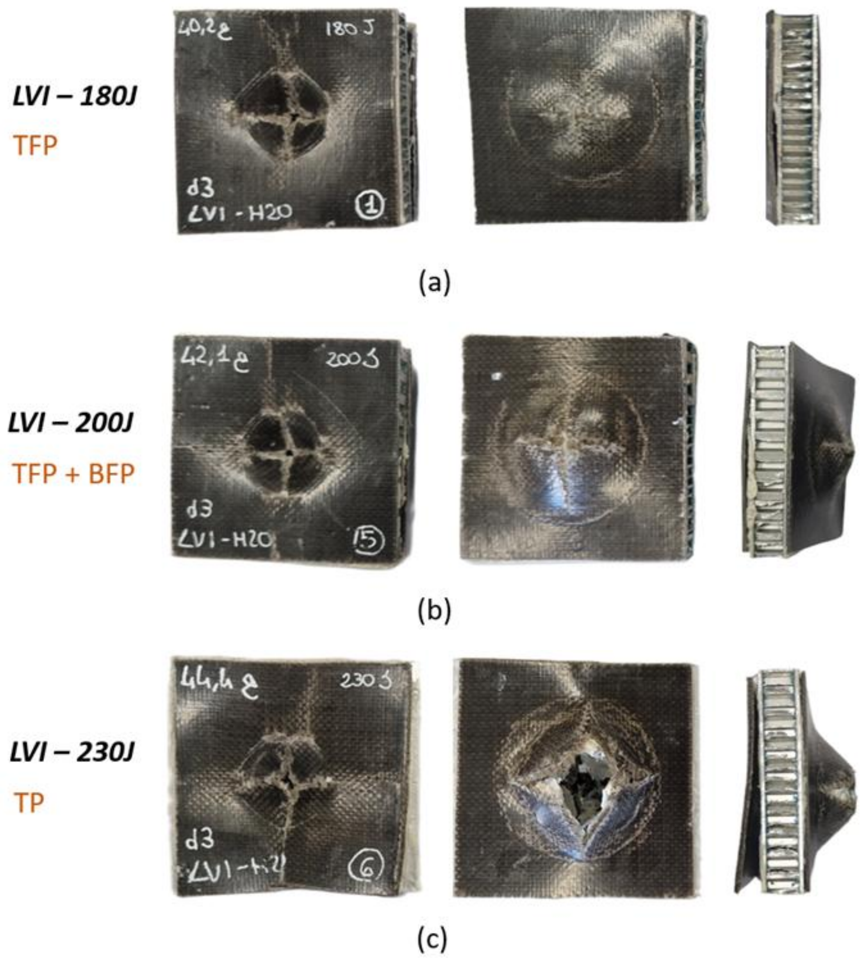

Figure 61: Low-velocity impact BFRP/AHS d3 specimens at different impact energies: (a) 180 J – TFP; (b) 200 J – TFP + BFP; (c) 230 J – TP.

For the BFRP/AHS d3 panels (Figure 61), three representative cases are shown: at 180 J the specimens exhibit top face perforation (Figure 61(a)), at 200 J both TFP and bottom face perforation are observed (Figure 61(b)), while at 230 J total penetration (Figure 61(c)) occurs. The main damage mechanisms include indentation of the impacted area, fibre fracture, and skins debonding.

For the BFRP/AHS d6 panels (Figure 62), two representative cases are presented: at 200 J only TFP is observed, with visible damage on the bottom skin but without perforation, while at 250 J both TFP and BFP occur. Compared to the 3 mm configuration, the 6 mm panels exhibit a wider damaged area, with the damage extending towards the panel edges rather than being confined to the impact zone.

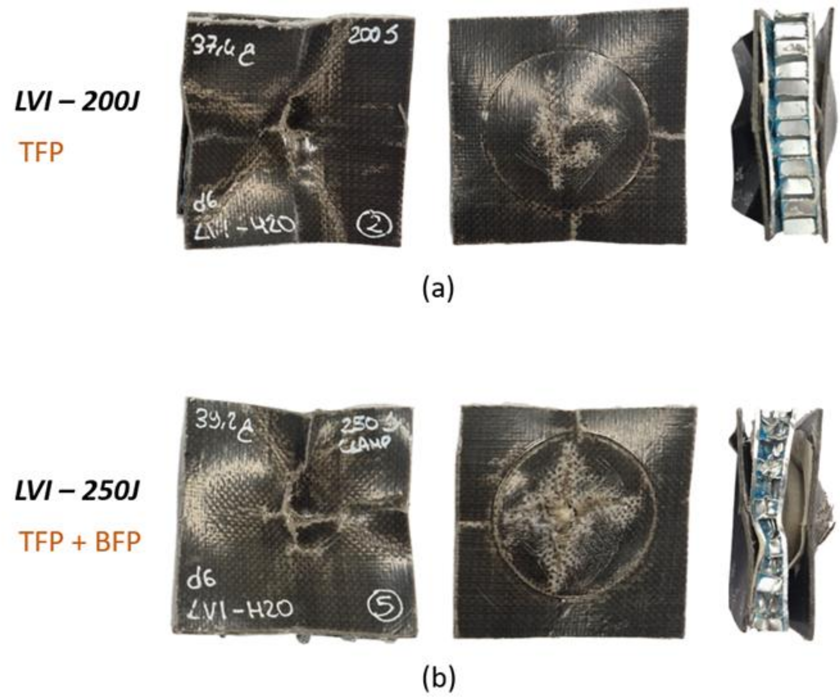

Figure 62: LVI BFRP/AHS d6 specimens at different impact energies: (a) 200 J - TFP; (b) 250 J – TFP + BFP

Following the visual inspection of the specimens, non-destructive tests were performed. For the BFRP/AHS d3 panels, flash thermography was conducted with the following parameters:

- Sub-windowing: 544 × 512 pixels
- Frame rate: 150 Hz

- Lens: MW 28 mm 2.0 HD
- Integration time: 479 ms
- Filter: Windows Average (Kernel 3 × 3 pixels)
- Display mode: Digital Detail Enhancement (FLIR)

The analysis was carried out on the specimen tested at 180 J, where top face perforation occurred. The resulting thermogram is shown in Figure 63.

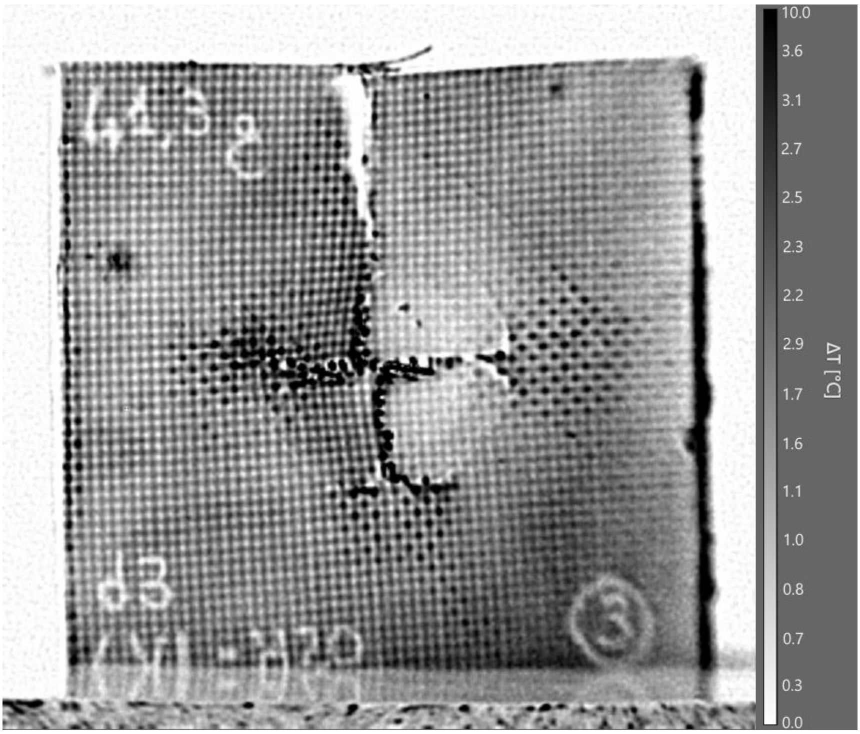

Figure 63: Flash thermography of BFRP/AHS d3 panel impacted at 180 J (TFP)

Damaged areas correspond to the failure of basalt skin, appearing as regions of higher apparent temperature (darker areas). Flash thermography provides only a superficial view of the damage; to investigate internal failure, digital radiography was employed.

The radiographic inspection was performed at 50 kV voltage and 0.4 mA current. Two BFRP/AHS d3 specimens were analysed: one tested at 180 J (TFP, Figure

64(a)) and one at 230 J (TP, Figure 64(b)). In both cases, buckling of the honeycomb core cells was observed.

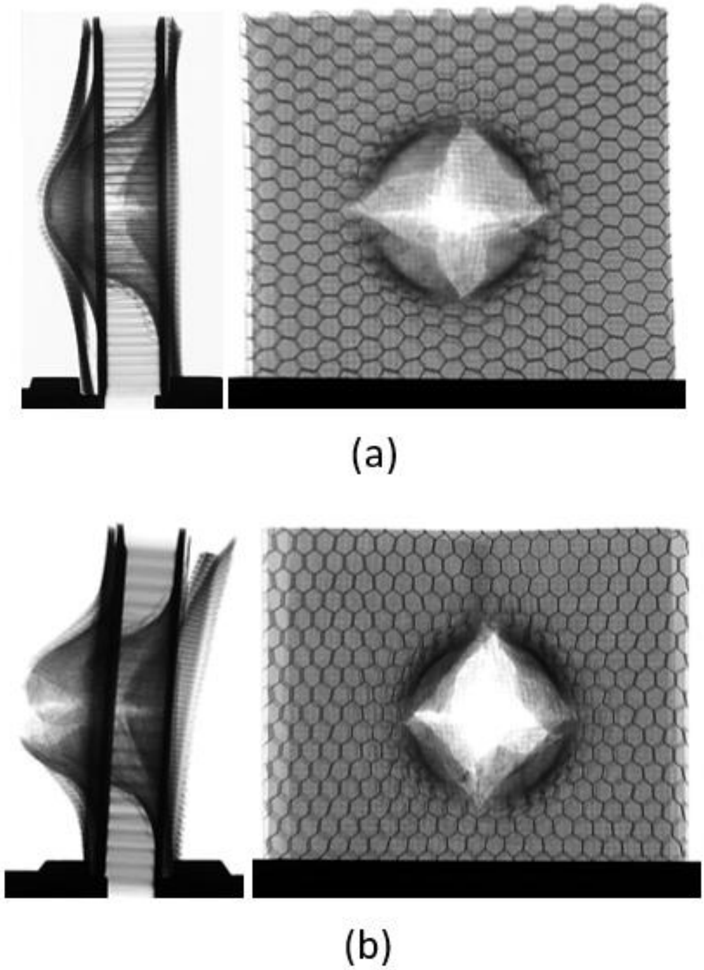

Figure 64: X-ray images of BFRP/AHS d3 panels; (a) specimen impacted at 180 J (TFP), (b) specimen impacted at 230 J (TP)

For the BFRP/AHS d6 panels, radiographic inspections were performed on specimens exhibiting TFP at 200 J (Figure 65(a)) and combined TFP + BFP at 250 J (Figure 65(b)). In both cases, buckling of the honeycomb core cells was clearly observed.

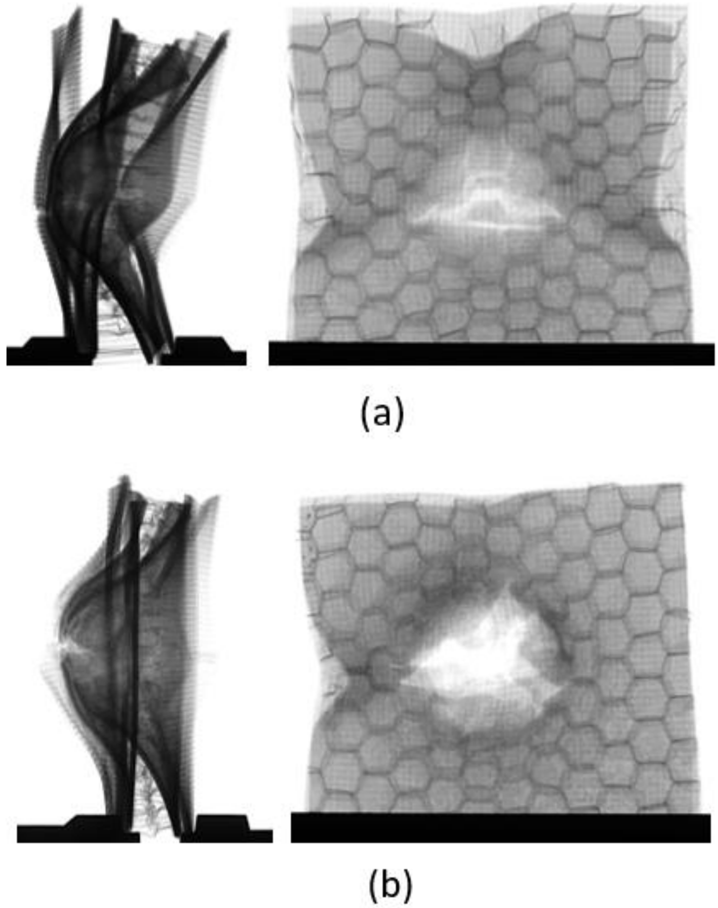

Figure 65: X-ray images of BFRP/AHS d6 panels; (a) specimen impacted at 200 J (TFP), (b) specimen impacted at 250 J (TFP + BFP)

5. Mono-material sandwich structures produced by innovative additive manufacturing process

Despite the growing interest in sustainable polymers, polylactic acid has emerged as one of the most promising materials for additive manufacturing, owing to its biodegradability, renewable origin, and ease of processing. In recent years, its use has extended beyond conventional 3D printing towards lightweight structural applications, where performance can be enhanced by reinforcing PLA with chopped carbon fibres [188].

However, current research still lacks systematic investigations on fully mono-material sandwich structures, in which both skins and core are made of the same polymer. Most studies to date have focused either on traditional polymeric foams or lattice cores fabricated via additive manufacturing [151]. These approaches, while effective, often rely on multi-material systems or non-foam-based architectures, leaving open important questions regarding how local density gradients and foam morphology influence the mechanical response of PLA sandwich structures.

Foam Additive Manufacturing represents a recent technological advancement that addresses these limitations. FAM enables the direct foaming of polymer filaments during the printing process, by incorporating a physical blowing agent into the filament. This allows the fabrication of fully mono-material sandwich systems, maintaining the chemical integrity and recyclability of PLA, while providing precise control over the internal density distribution. By tuning the printing parameters, mechanical properties can be locally tailored, optimizing bending strength, energy absorption, and impact resistance.

This chapter investigates these aspects by fabricating and characterizing PLA mono-material sandwich specimens produced via FAM. Different core density gradients were implemented and tested under three-point bending and low-velocity impact loading. The results are compared with PLA specimens containing traditional honeycomb infill, to assess the influence of core morphology and process parameters on mechanical performance and failure mechanisms. The study ultimately aims to demonstrate the potential of FAM for producing sustainable, high-performance structures suitable for lightweight engineering and eco-friendly packaging applications.

5.1 Materials and methods

This chapter describes the materials and experimental methods adopted to manufacture and characterize PLA sandwich specimens by means of Foam Additive Manufacturing. Particular attention was devoted to ensuring the reproducibility of the process and the comparability between foamed and bulk specimens, to allow a systematic investigation of how different core morphologies affect mechanical performance.

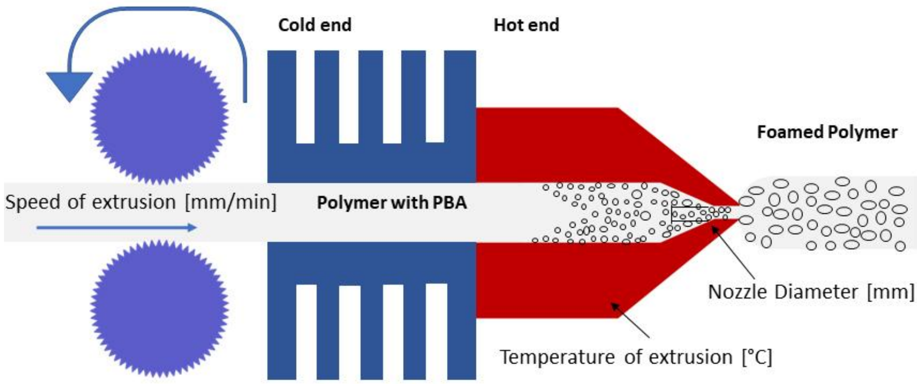

Figure 66: Extrusion process outline [189].

The FAM process consists of three main phases: solubilization, desorption, and extrusion. During the solubilization phase, the polymeric filament is placed in a pressure vessel where carbon dioxide (CO_2) is introduced as physical blowing agent. The absorption pressure (P_a), absorption temperature (T_a), and absorption time (t_a) are carefully controlled to allow CO_2 to solubilize within the polymer matrix, forming a homogeneous polymer-PBA solution. Subsequently, in the desorption phase, the saturated filament is stored at ambient pressure and temperature for a given time (t_d), allowing controlled release of part of the absorbed gas before printing. Finally, during extrusion, the polymer experiences a rapid pressure drop, and a temperature rise as it passes through the heated nozzle, leading to bubble nucleation and polymer foaming. In this stage, extrusion temperature (T_e), extrusion speed (S_e), and nozzle diameter (N_d) play a crucial role in determining the final foam morphology. A schematic illustration of the process is reported in Figure 66.

The specific PLA used, grade 710 M, was obtained as microbeads from Bewi Synbra, which allows precise control over the thermal history and the rheology of the filament. The filaments were produced by a 3D printing filament manufacturer Eumaker, Italy, while CO_2 was used as blowing agent.

All the specimens were manufactured in a single, fully automated 3D printing process. The fabrication was carried out with a custom-made filament 3D printer, named *Step 2.1*, equipped with a commercial E3D Vulcano hot end with a 0.6 mm nozzle. The solubilization parameters were kept constant across all specimens to minimize variations in the thermal history of the polymer. Specifically:

- P_a = 40 bar.
- t_a = 48 h.
- t_d = 6 to 24 h.
- T_e = 180 °C.

Table 20: Printing parameters (ND = Not defined) [168].*

Type	S_N (mm/s)	S_e (mm/min)	L_w (mm)	L_h (mm)	F_r (%)	Infill (%)	S (mm)
F1	100	498.9	1	1	20	100	ND*
F2	60	383.2	0.8	0.8	40	100	ND*
F3	40	215.5	0.6	0.6	60	100	ND*
B10	100	299.3	0.6	0.2	100	10	15
B40	100	299.3	0.6	0.2	100	40	3.3
B60	100	299.3	0.6	0.2	100	60	1.5
B100	100	299.3	0.6	0.2	100	100	ND*

Table 20 presents the key printing parameters utilized for fabricating the different zones of the specimen. These parameters were set in a slicing software called

Simplify 3D to generate the G-CODE file, which corresponds to the machine commands for each specimen. Specifically:

- S_N = Refers to the Nozzle Speed, set as the constant speed of the hot end in space. Despite high acceleration settings a = 4000 mm/s^2, accelerations are mostly negligible, ensuring a nearly constant speed throughout the process.
- L_w =Refers to the imposed layer width, which needs to be a multiple of the desired total width of the specimen.
- L_h = Refers to the imposed layer height, required to be a multiple of the desired total height of the specimen [190].
- F_r = Refers to the Flowrate Multiplier, a coefficient used to adjust the calculated flowrate to account for die swell [191].
- t_z = Refers to the total thickness of the same density zone.
- Infill = Refers to the internal geometry of the printed part, expressed in terms of percentage and shape.
- S = Refers to the dimensional measure of the honeycomb cell in the infill of the BULK specimen.
- S_e = Refers to the imposed extrusion speed, defined as the filament speed in millimetres per minute. This speed is calculated differently from the printing speed, as it is determined by the need to deposit the total volume of the strand, considering L_w and L_h. It can be computed using Eq. (46), under the assumptions of incompressibility of the polymer melt and conservation of mass.

$$S_e = \frac{L_w \cdot L_h \cdot S_N}{\pi \cdot \left(\frac{D_f}{2}\right)^2} \cdot 60 \cdot \frac{F_r}{100} \quad (46)$$

The rigid top and bottom plies of all the specimens were produced using the same parameters as the B100 reference specimen, with detailed printing parameters provided in Table 20.

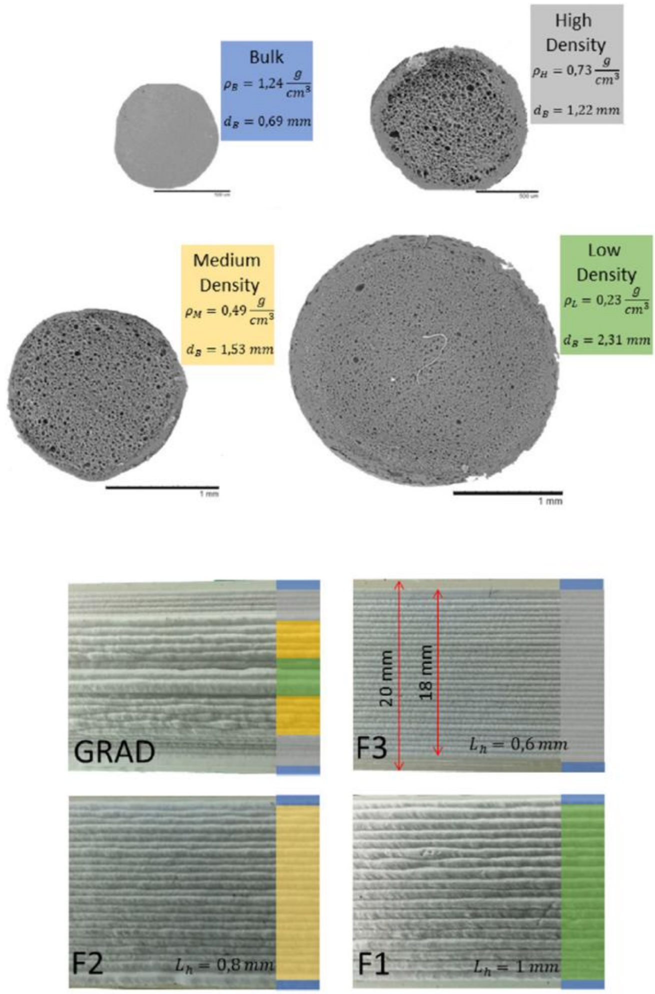

Figure 67: SEM pictures of the section of the sandwich structures with a zoom of cross section of a strand realized with the same parameter of the foam. Figure adapted from [189].

All specimens were designed with nominal dimensions of 180 × 30 × 20 mm for bending tests, and 60 × 60 × 20 mm for LVI tests. The ratio between height and thickness of the specimens was chosen to characterize the properties of the core and enable the design of an improved core lamination. The study involved evaluating eight different sample types: four featuring a foamed PLA core, designated as $F1$, $F2$, $F3$, and GRAD, and four constructed with a conventional honeycomb infill core made of non-foamed Bulk PLA, labelled as B10, B40, B60, B100.

The four images located at the bottom of Figure 67 shows the external faces of the specimens from the F and GRAD series. The lamination sequence consists of 1 mm top and bottom layers and foamed cores of varying densities.

At the top of Figure 67, four SEM images showcase the cross sections of the strands that compose the specimens. These strands are fabricated using the same parameters as the infill of the specimen. All foamed wires produced have a closed cell distribution. Specifically, the Bulk strand is highlighted in blue, the High-density foam strand in grey, the Medium-density foam strand in yellow, and the Low-density foam strand in green.

The lamination sequence for each foamed specimen (F and GRAD series) in the Z direction includes:

- Bottom plies made of 1 mm thickness non-foamed Bulk PLA to create the rigid skin, in light blue for all the specimens.
- Core made of 18 mm thickness with a 100% linear foamed as shown in Table 20 and have the following features:
    - F1 core with a Low-density foam.
    - F2 core with a Medium-density foam.
    - F3 core with a High-density foam.
    - GRAD specimen with a symmetric lamination sequence that involves all three types of density foam. The lamination sequence is explicated in Table 21.
- Top plies made of 1 mm thickness non-foamed bulk PLA to create the rigid skin, in blue for all the specimens.

Table 21: Lamination sequence and printing parameters of the gradient specimen [189].

Type	Layer	S_N (mm/s)	S_e (mm/min)	L_w (mm)	L_h (mm)	F_r (%)	t_z (mm)
Bulk	0 to 5	100	299.3	0.6	0.2	100	1
High Density	6 to 11	40	215.5	0.6	0.6	60	3
Medium Density	12 to 17	60	383.2	0.8	0.8	40	4
Low Density	18 to 22	100	498.9	1	1	20	4
Medium Density	23 to 28	60	383.2	0.8	0.8	40	4
High Density	29 to 34	40	215.5	0.6	0.6	60	3
Bulk	35 to 40	100	299.3	0.6	0.2	100	1

The B series specimens, as shown in Figure 68, are constructed using bulk polymer, with a honeycomb infill designed to achieve densities like their counterparts in the F series.

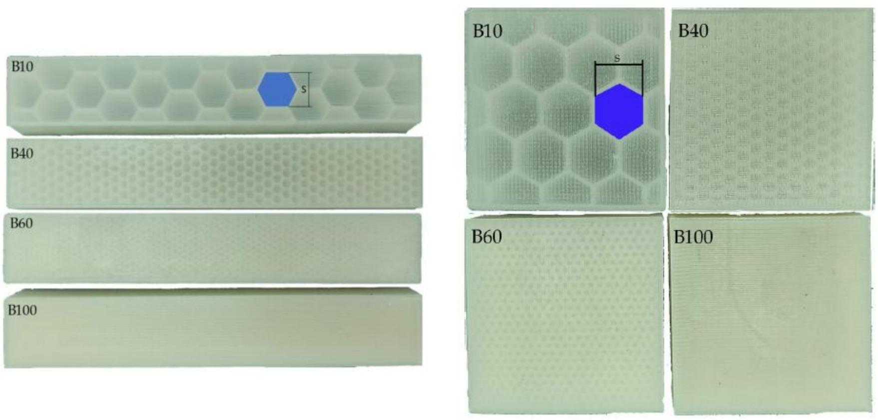

(a) (b)

Figure 68: Overview of bulk specimens showcasing the variation in honeycomb infill patterns. (a) Three-point bending bulk specimens [189]; (b) low-velocity impact bulk specimens [168].

It was determined that the three foam densities provide total weight for the specimens like those made with 10%, 40%, and 60% honeycomb infill. The lamination sequence for each non-foamed specimen (B series) in the Z direction includes:

- Bottom plies made of 1 mm thickness non-foamed Bulk PLA to create the rigid skin.
- Core made of 18 mm thickness with different percentage of honeycomb infill, as shown in Table 20.
- Top plies 1 mm of non-foamed Bulk PLA for the rigid skin.

To test the properties of selected PLA, a 100% linearly filled bulk sample, designed B100, was produced.

Table 22 summarizes the measured mass and densities of all specimens. As intended, it is observed that the densities of specimens B10 and F1, B40 and F2, B60 and F3 are very similar, respectively. The data reported include both the specimens manufactured for bending tests (180 × 30 × 20 mm) and those specifically designed for the LVI tests (60 × 60 × 20 mm).

Table 22: Mass and density values of specimens for bending and impact test campaigns [168], [189].

	Three-point bending specimens		**Low-velocity impact specimens**	
Type	**m_{avg} (g)**	**ρ_{avg} (kg/m³)**	**m_{avg} (g)**	**ρ_{avg} (kg/m³)**
F1	35.97	333.02 ± 4.61	23.66	328.65 ± 7.63
F2	60.8	562.92 ± 6.50	40.34	561.60 ± 4.09
F3	84.92	786.30 ± 12.48	56.96	791.11 ± 14.97
GRAD	61.8	572.22 ± 7.53	41.86	581.34 ± 4.88
B10	38.52	356.66 ± 7.49	24.83	344.90 ± 16.79
B40	62.71	580.63 ± 9.47	42.23	586.49 ± 11.89
B60	85.55	792.09 ± 11.95	57.11	793.19 ± 7.82
B100	131.52	1271.81 ± 17.70	90.54	1257.53 ± 2.60

Mechanical characterization was performed through three-point bending tests using the ITALSIGMA servo-hydraulic testing machine, calibrated according to ISO 7500-1 (class 1) and described in Section 3.1. Tests were conducted in displacement control at speeds of 1 and 2 mm/min to assess the influence of strain rate on the mechanical response of foamed cores. The support span was set to 120 mm, with an initial preload of approximately 80 N. For each specimen type (F1, F2, F3, GRAD, B10, B40, B60, B100), at least three samples were tested to ensure repeatability.

The absorbed energy (E) was calculated using the same formulation as in Eq. (41), with the upper integration limit set to the displacement corresponding to the first failure mechanism ($\delta_{failure}$).

The bending tests were monitored using an infrared camera (Flir Systems SC640) with a resolution of 640 × 480 pixels and a thermal sensitivity of 30 mK at 30 °C. The camera is equipped with an uncooled Focal Plane Array (FPA) microbolometer sensor, and the acquisition frame rate was set to 30 fps. Thermograms were post-processed using FLIR ResearchIR Max software, applying a 3×3 window average filter to reduce noise. Additionally, the Digital Detail Enhancement (DDE) non-linear image processing algorithm was employed to enhance thermal contrast. The 1234 palette was selected as the most suitable for the analyses conducted in this study. Due to the inherently high emissivity of PLA, no surface treatment or painting of the specimens was required [192]. The camera was positioned on a tripod approximately 0.4 m from the specimens, resulting in an instantaneous field of view (IFOV) of 0.2 mm, calculated for the 38 mm focal length lens. The measurement accuracy of the infrared system is ±2 °C or ±2 % of the reading.

LVI tests were conducted according to ISO 6603-2 using a CEAST Fractovis Plus impact testing machine (Figure 23, Section 3.1). The indenter used for the LVI test campaign is the H20 hemispherical tup (as per "ISO 6630") (Figure 38, Section 4.1.1). The tests were conducted using an impact mass, kept constant, of 6.5 kg.

5.2 Three-point bending results

In the present section, the results obtained from the three-point bending tests are presented and discussed. Particular attention is devoted to the comparison between foamed and honeycomb specimens, as well as to the effect of density and loading rate on the mechanical response. The analysis includes the evaluation of force-displacement curves, absorbed energy, and failure mechanisms, which were investigated through thermographic monitoring and microscopic observations. A summary of the experimental data is reported in Table 23.

Table 23: Three point bending tests results [189]. F_f = First failure mechanism load; δ_f = Displacement at first failure mechanism load.

Type	Test speed (mm/min)	F_f (N)	δ_f (mm)	E (J)	E/mass (J/kg)	E/ρ (J·m³/kg)
F1	2	607	11.66	5.2	143.85	0.0156
	1	604	12.5	5.21	141.65	0.0156
F2	2	1427	5.16	4.71	78.08	0.0084
	1	1610	8.08	9.69	157.61	0.0172
F3	2	1372	1.98	1.49	17.36	0.0019
	1	1118	2.08	1.31	15.74	0.0017
GRAD	2	967	3.26	2	32.49	0.0035
	1	1106	3.36	2.18	34.25	0.0038
B10	2	1441	3.63	3.04	78.27	0.0085
	1	1192	2.88	1.98	49.71	0.0056
B40	2	1981	3.75	3.7	59.15	0.0064
	1	1154	2.09	1.15	18.45	0.0020
B60	2	2654	4.5	7	81.25	0.0088
	1	2617	3.92	5.43	62.69	0.0069
B100	2	4918	3.56	8.33	63.89	0.0065
	1	5822	4.61	13.58	102.11	0.0107

By comparing the two families of specimens with the same density, the highest load values were recorded for the Bulk specimens, whereas the foamed specimens exhibited higher deflection and, for the F1 and F2 families, greater absorbed energy. The experimental data highlight the relationship between strain rate and failure mechanisms. For the F1 specimens, the indentation mechanism was found to be independent of the loading rate. For the F2 specimens the debonding failure mode at a faster rate requires twice as much energy. In F3 specimens, the core shear doesn't depend on the speed rate although requires low energy values. Finally, in the GRAD specimens, debonding occurred independently of the loading rate due to the variable porosity. The trends of the force-displacement curves are reported in Figure 69 and Figure 70.

To further investigate the failure mechanisms, thermographic images in Figures 71 and 72 were analysed qualitatively. Blue corresponds to the coldest regions, while red indicates the warmest. The detailed behaviour of foamed specimens varies according to core density. F1 specimens show an initial load increase followed by stabilization, corresponding to the onset of indentation (Figure 71, F1 b). The indentation is followed by core densification and the initiation of a crack in the bottom skin, which then propagates into the core (Figure 73, F1 a). F2 specimens exhibited the same collapse mode (detail of the crack formation in bottom skin in Figure 71, F2 c and in Figure 73, c), but in this case, it was possible to notice debonding between the upper skin and the core (Figure 71, F2 b). The microscopic investigation highlights the debonding failure between the upper skin and the core. It is also possible to observe how a portion of the core remained bonded to the skin (Figure 73, b).

In F3 specimens, indentation is followed by delamination of the core layers (core shear), as highlighted by colder regions in the thermogram (Figure 71, F3 b).

The microscopies highlight a delamination failure detail and a case in which there is also an intralayer crack in the core (Figure 73, e). In the GRAD specimens, the core layers debonding was highlighted by thermography and microscopy investigation (Figure 71, GRAD b and Figure 73, f).

In contrast, the honeycomb specimens (B10, B40, B60) and the solid sample (B100), show brittle behaviour. The thermographic investigation reveals that the B10 at 2 mm/min specimens exhibit a failure mode characterized by face wrinkling (Figure 71, B10 b), followed by core failure (Figure 71, B10 c). Conversely, in the B40, B60, and B100 specimens, distinguished by variations in apparent temperature, it is evident that the failure mechanism is related to the initiation of a crack in the bottom section and its subsequent propagation, which leads to the specimens' structural failure (Figure 71, B40 b, B60 b, B100 b).

The failure mode analysis of the specimens tested at 1 mm/min is shown in Figure 72. Notably, the test velocity has not a significant effect on failure mechanisms, since all tested specimens appeared to be very similar if subjected to visual and thermographic inspection.

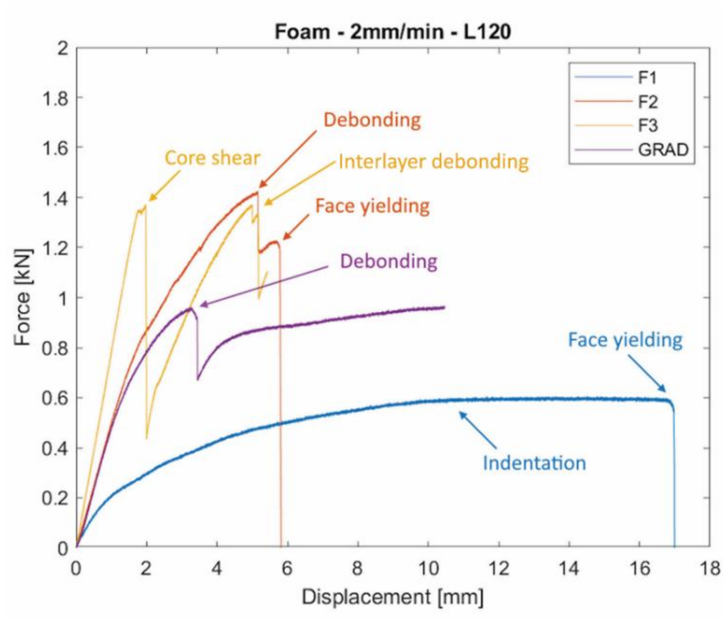

(a)

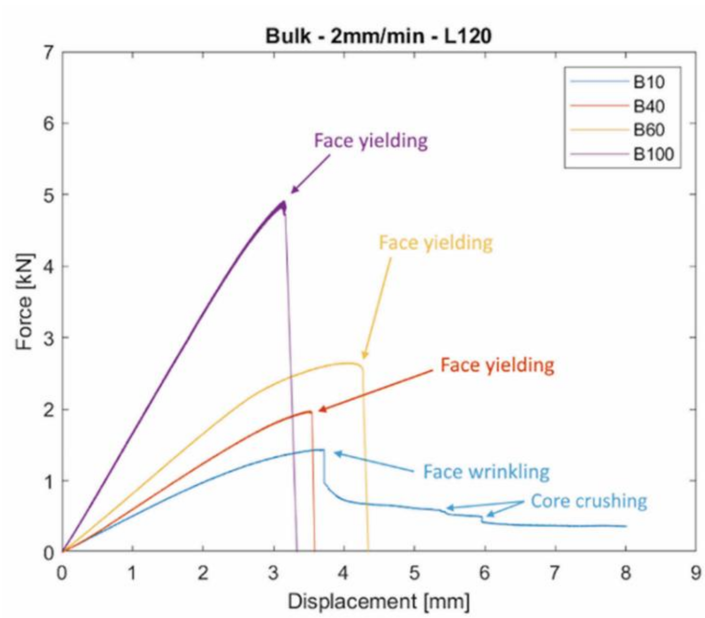

(b)

Figure 69: 2 mm/min Load-Displacement curves and failure modes for foam (a) and bulk (b) specimens [189].

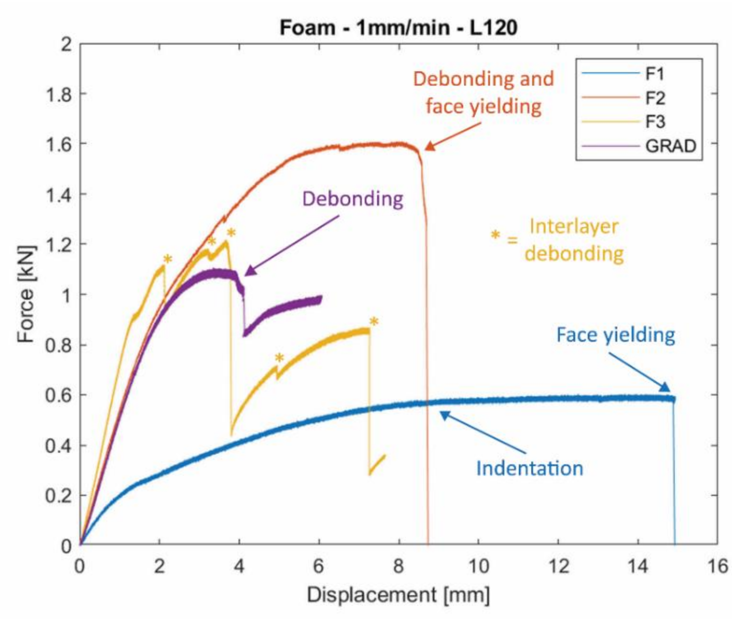

(a)

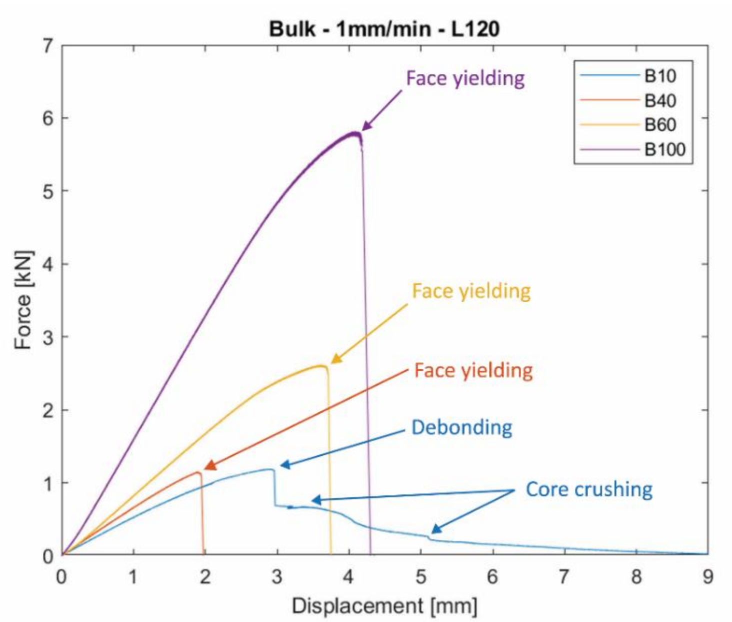

(b)

Figure 70: 1 mm/min Load-Displacement curves and failure modes for foam (a) and bulk (b) specimens [189].

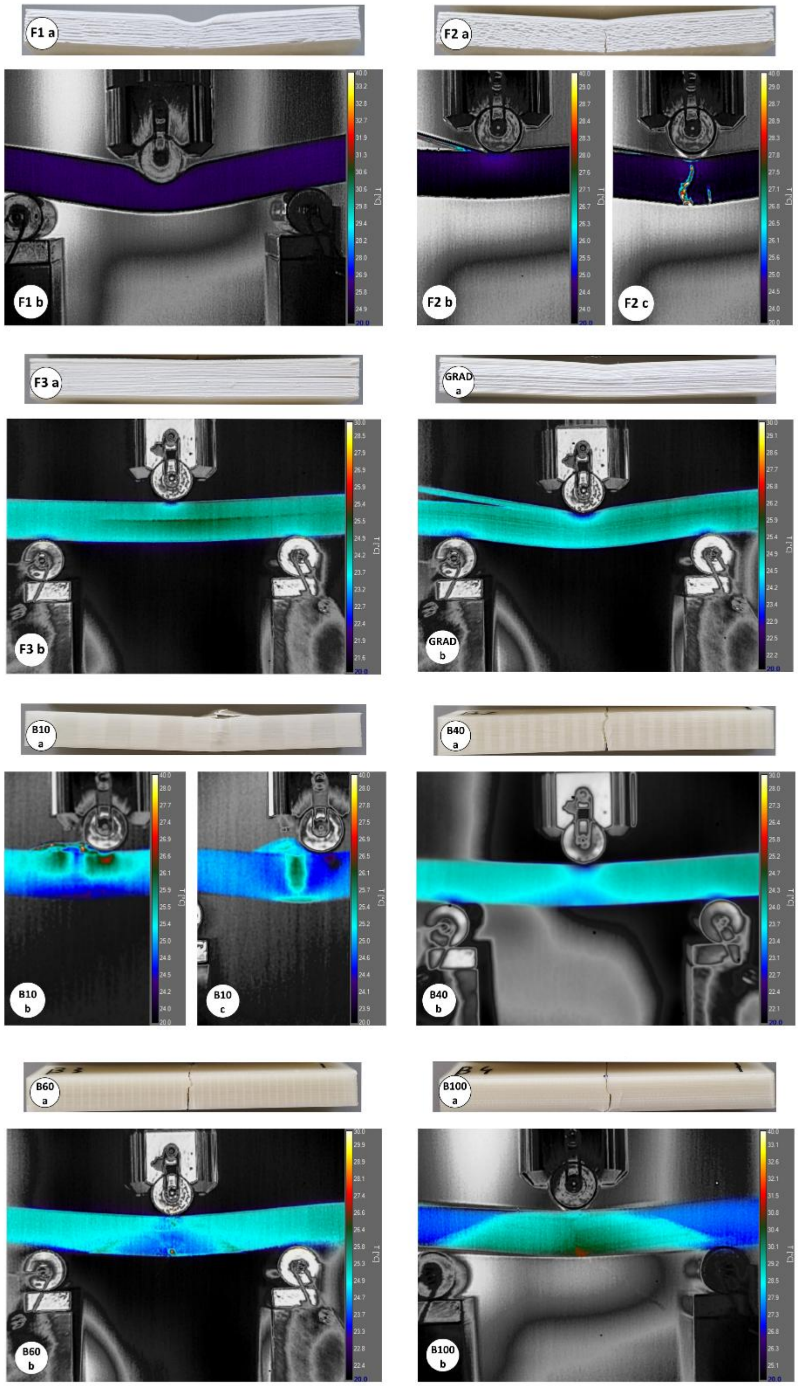

Figure 71: Failure modes analysis at 2mm/min by thermography and visual inspection [189].

Figure 72: Failure modes analysis at 1mm/min by thermography and visual inspection [189].

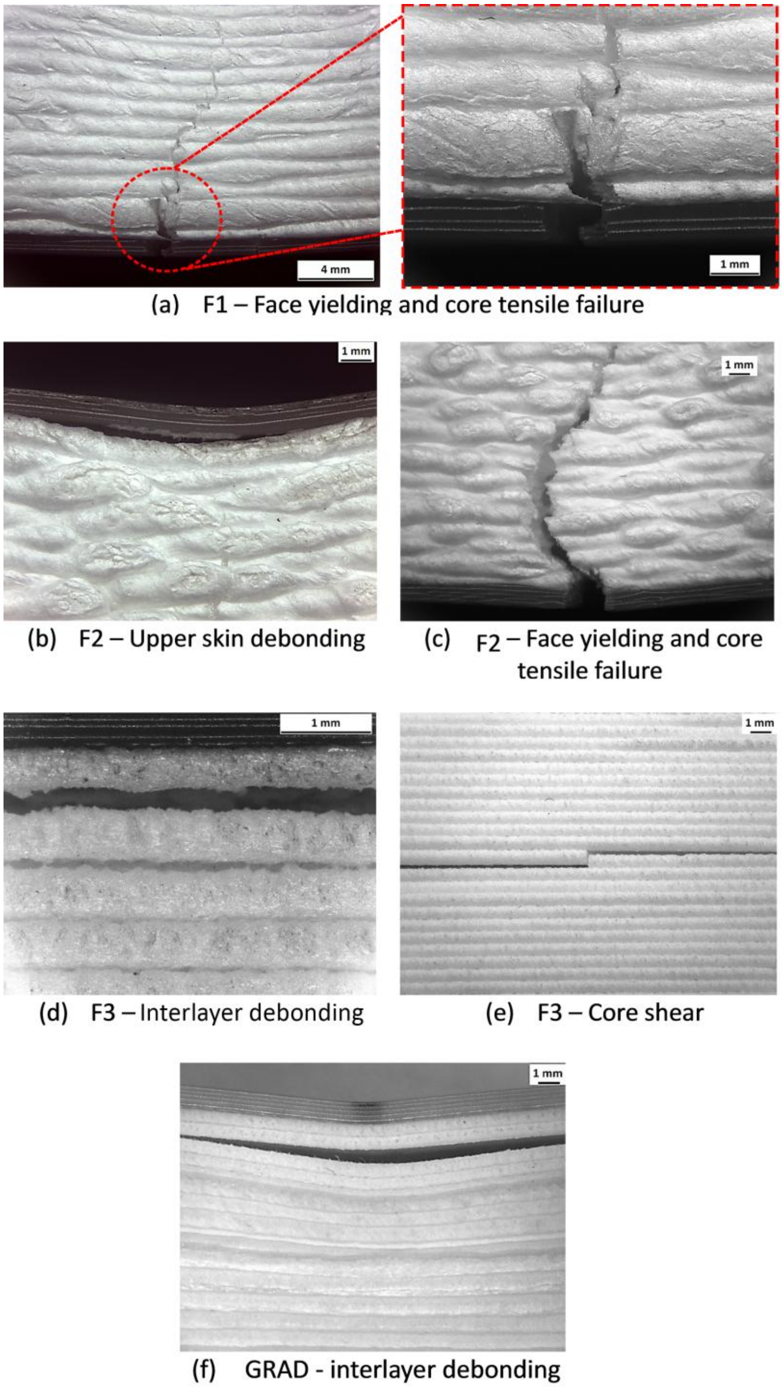

Figure 73: Microscope images of the failure mechanism of the foam specimen [189].

Gibson and Ashby [35] proposed an analytical model to evaluate the flexural and shear stresses in sandwich structures. In particular, the flexural stress σ can be calculated by Eq. (47), while the shear stress τ is reported in Eq. (48):

$$\sigma = \frac{F \cdot l}{4 \cdot b \cdot t \cdot c} \tag{47}$$

$$\tau = \frac{F}{2 \cdot b \cdot c} \tag{48}$$

where F represents the applied load in the three-point bending test, l is the span distance, b denotes the specimen width, t refers to the skin thickness and c indicates the core thickness. The flexural stresses associated with the different failure mechanisms are summarized in Table 24 and Table 25, while the maximum flexural strength values σ_{max}, related to the applied flexural moment M, are reported in Table 26. Once the maximum flexural strengths were evaluated, it was possible to calculate the relative flexural strength through the ratio with the maximum stress obtained for the non-foamed 100% infill specimen (B100).

Table 24: Failure data of 2 mm/min specimens [189].

Specimen	**Failure mechanism**	**$\sigma_{failure}$ (N/mm²)**
F1	Face yielding	32.95
F2	Debonding	78.63
	Face yielding	67.48
F3	Core shear	75.96
	Interlayer debonding	75.68
GRAD	Debonding	52.75
B10	Face wrinkling	79.90
	Core crushing	32.86
B40	Face yielding	108.77
B60	Face yielding	143.89
B100	Face yielding	268.16

Table 25: Failure data of 1 mm/min specimens [189].

Specimen	Failure mechanism	$\sigma_{failure}$ (N/mm²)
F1	Face yielding	32.40
F2	Debonding and face yielding	84.56
F3	Interlayer debonding	62.13
GRAD	Debonding	57.06
B10	Debonding	67.71
	Core crushing	37.25
B40	Face yielding	60.91
B60	Face yielding	142.76
B100	Face yielding	320.55

Table 26: Bending stiffness and maximum bending strength [189].

Specimen	D (N·mm²)	Test speed (mm/min)	σ_{max} (N/mm²)	τ_{max} (N/mm²)
F1	$2.82 \cdot 10^{6}$	2	33.72	$5.62 \cdot 10^{-4}$
		1	33.54	$5.59 \cdot 10^{-4}$
F2	$5.04 \cdot 10^{6}$	2	79.27	$1.32 \cdot 10^{-3}$
		1	89.46	$1.49 \cdot 10^{-3}$
F3	$1.70 \cdot 10^{7}$	2	76.23	$7.20 \cdot 10^{-4}$
		1	67.66	$1.13 \cdot 10^{-3}$
GRAD	-	2	53.70	$8.95 \cdot 10^{-4}$
		1	61.45	$1.02 \cdot 10^{-3}$
B10	-	2	80.04	$8.15 \cdot 10^{-4}$
		1	66.21	$1.10 \cdot 10^{-3}$
B40	-	2	110.04	$1.86 \cdot 10^{-3}$
		1	64.08	$8.10 \cdot 10^{-4}$
B60	-	2	147.43	$2.46 \cdot 10^{-3}$
		1	145.39	$2.45 \cdot 10^{-3}$

B100	$4.54 \cdot 10^{7}$	2	273.24	$4.55 \cdot 10^{-3}$
		1	323.45	$5.39 \cdot 10^{-3}$

The relative density (ρ_{rel}) was calculated as the ratio between the specimens' density and the density of a fully (non-foamed) filled specimen (ρ_{PLA} = 1.26 g/cm^3). Relative strength was plotted against relative density to apply the Gibson-Ashby model, as shown in Figure 74.

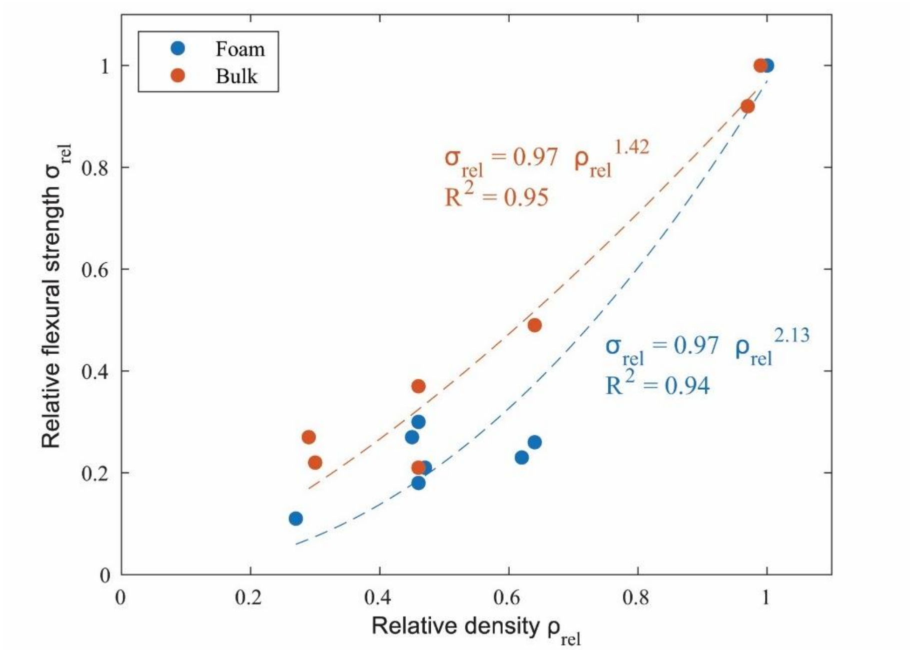

Figure 74: Relative flexural strength vs. relative density [189].

The results allow the prediction of the mechanical strength of the proposed sandwich structures under three points bending load, with a good fitting. The stiffness (D) is calculated from the equivalent flexural rigidity of the beam by using the well-known relationship (2). It is important to note that for the non-foamed specimen (B100), the flexural rigidity was evaluated using the Euler-Bernoulli beam theory [193]. The stiffness values are reported in Table 26

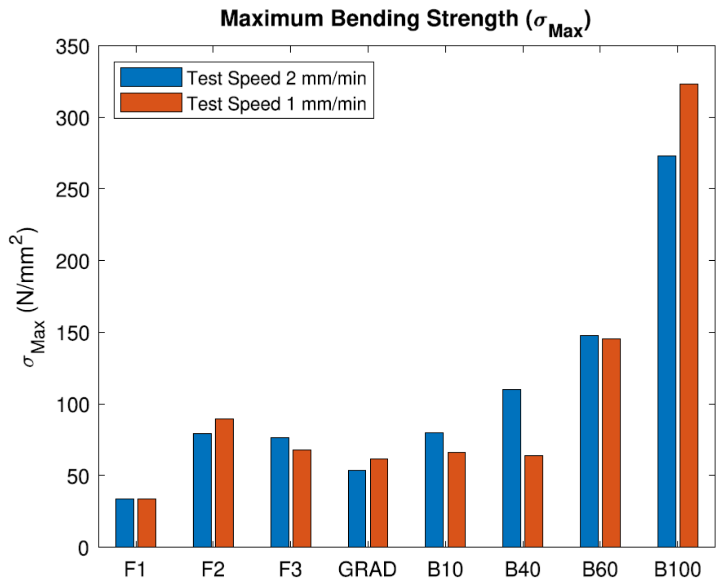

(a)

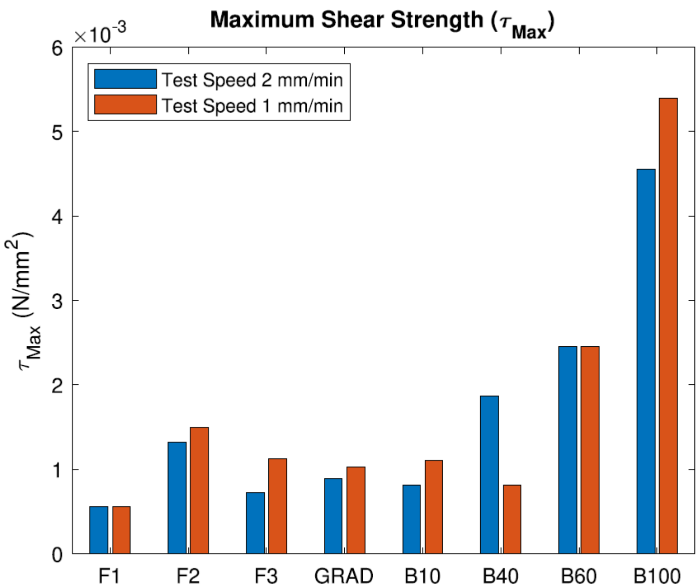

(b)

Figure 75: Maximum bending strength and maximum shear strength comparison [189].

The effect of the testing velocity is summarized in Figure 75, which shows that no significant influence can be detected either on flexural or shear strength. A different trend was observed only for the B40 specimens, which exhibited higher strength at 2 mm/min. This behaviour can be explained by the location of the crack initiation point under tensile load, which in that case was not centred along the specimen (see Figure 71, B40b). In general, the Bulk specimens showed an increasing trend of flexural strength with density, whereas within the foamed core specimens, the F2 family exhibited superior mechanical performance compared to both graded and other foam densities.

5.3 Low-velocity impact results

In this section, the results of the LVI tests performed on both foamed, graded and bulk specimens are presented and discussed. The objective was to evaluate the impact response of the different sandwich configurations and to compare their mechanical behaviour under increasing impact energy levels.

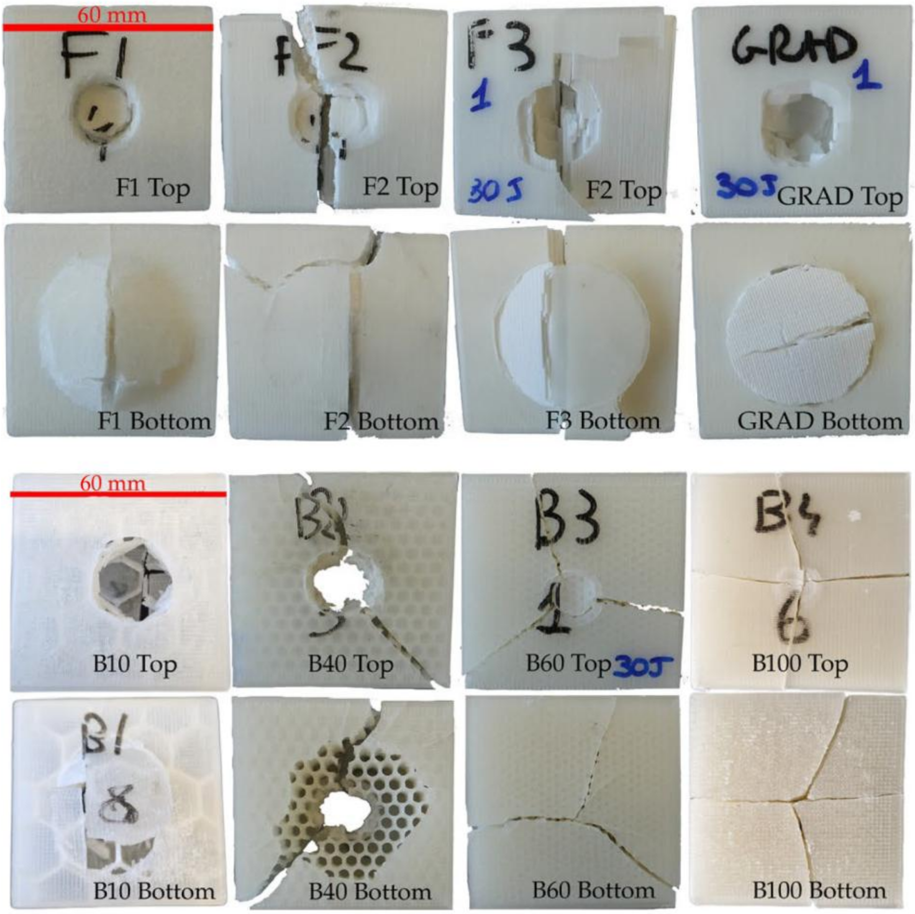

Figure 76: Foam and bulk specimens after impact test [168].

Figure 76 reports the front and rear sides of the impacted specimens at 30 J, showing the interaction between the impactor and the samples. The impact damage is concentrated under the contact point between the specimen and the impactor for the foam and grad samples, while a more brittle behaviour is observed for the bulk specimens, which collapsed by breaking into four parts. When the impact energy exceeded 25 J, all specimen typologies showed a perforation of both the faces and the core.

Figure 77 shows the load-displacement curves of all tested specimens impacted at different energy levels until complete penetration, offering a detailed description of the mechanical response. Across all examined specimen groups, a characteristic force-displacement trend is noticeable, characterized by an initial phase where the load increases linearly with displacement, followed by a peak load attributed to the contact between the tup and the top skin, and finally, a subsequent decrease in load. The specimen typology strongly influences both the impact force and the duration of the impact event.

Figure 78 shows the force-displacement curves of bulk samples for different impact energies for all fill densities. In this case, for all tested samples, the maximum peak load increases as the impact energy increases. For specimens with lower density, the curves are characterized by high level of curve noise due to the failure of the core cell walls. These oscillations decrease as the density increases, showing a smoother curve. Also, the maximum load increases with the bulk density. However, the displacement in correspondence of the load peak decreases since the higher density of the specimen also visible in the mode breakage in Figure 76.

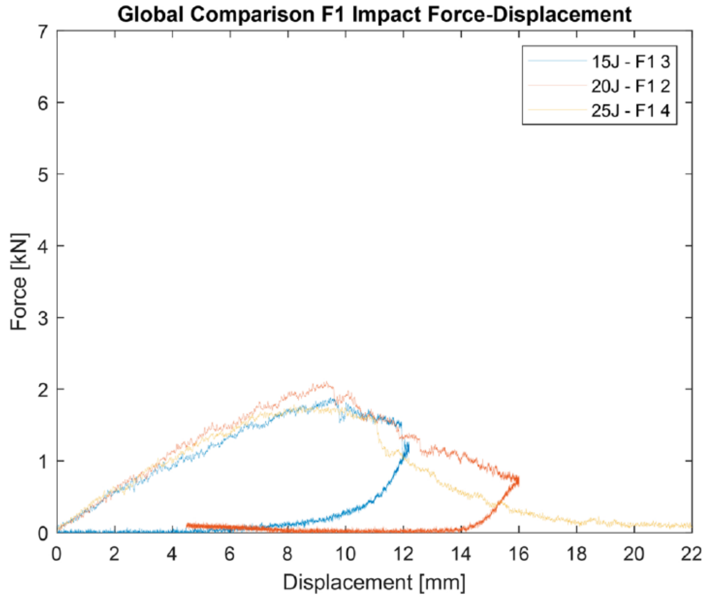
Global Comparison F1 Impact Force-Displacement
15J - F1 3
20J - F1 2
25J - F1 4
Force [kN]
Displacement [mm]
0
1
2
3
4
5
6
7
0
2
4
6
8
10
12
14
16
18
20
22

(a)

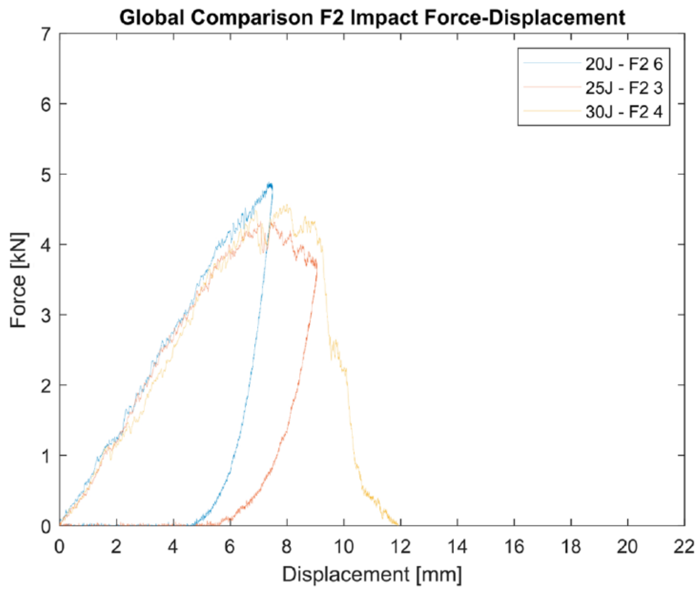
Global Comparison F2 Impact Force-Displacement
20J - F2 6
25J - F2 3
30J - F2 4
Force [kN]
Displacement [mm]
0
1
2
3
4
5
6
7
0
2
4
6
8
10
12
14
16
18
20
22

(b)

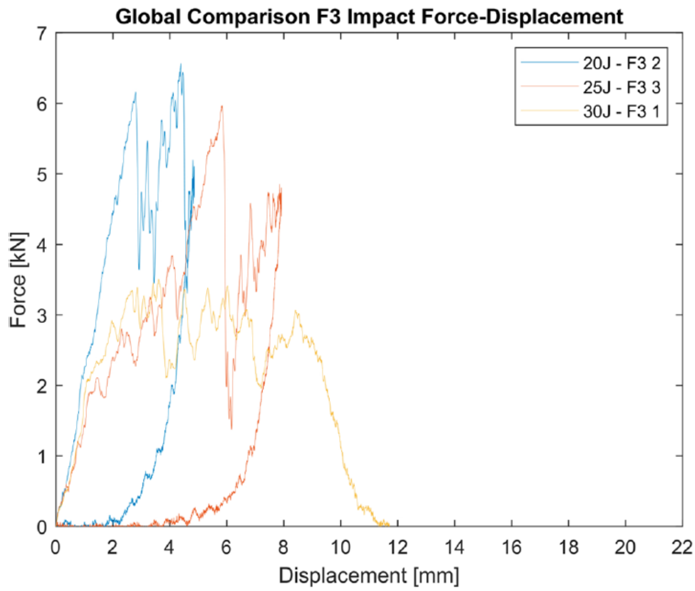

(c)

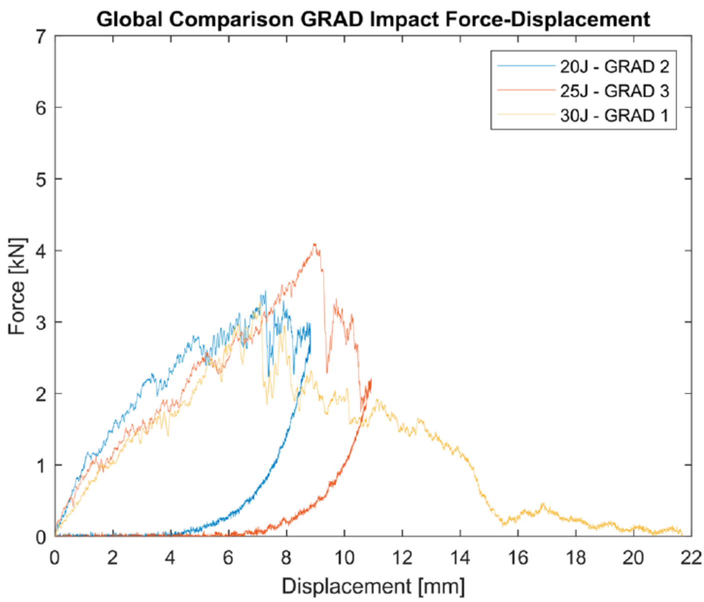

(d)

Figure 77: Foam force-displacement curves. (a) F1; (b) F2; (c) F3; (d) GRAD [168].

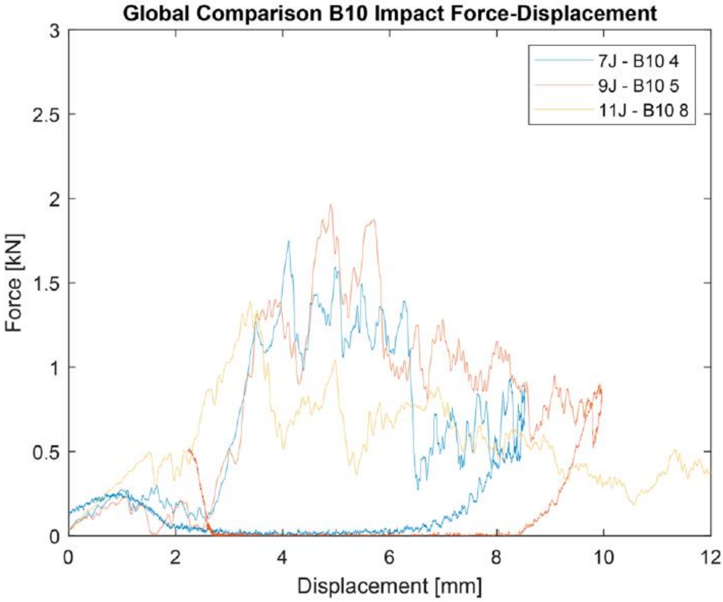
Global Comparison B10 Impact Force-Displacement
7J - B10 4
9J - B10 5
11J - B10 8
Force [kN]
Displacement [mm]
0
0.5
1
1.5
2
2.5
3
0
2
4
6
8
10
12

(a)

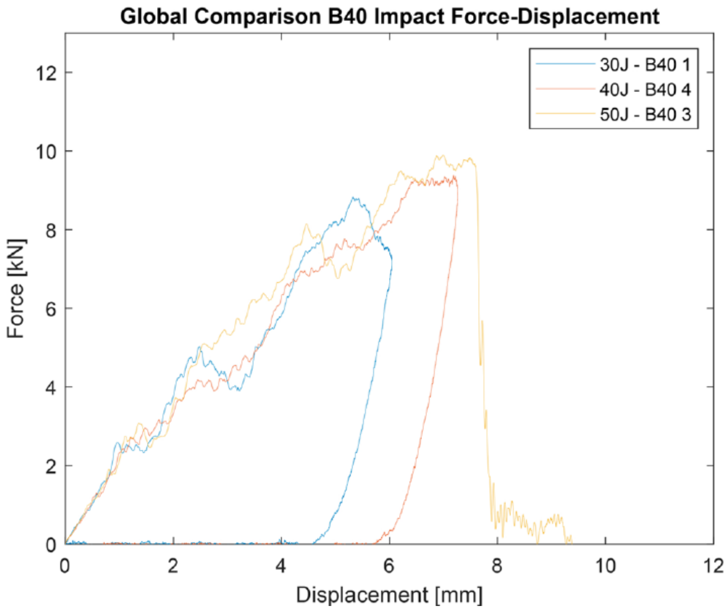
Global Comparison B40 Impact Force-Displacement
30J - B40 1
40J - B40 4
50J - B40 3
Force [kN]
Displacement [mm]
0
2
4
6
8
10
12
0
2
4
6
8
10
12

(b)

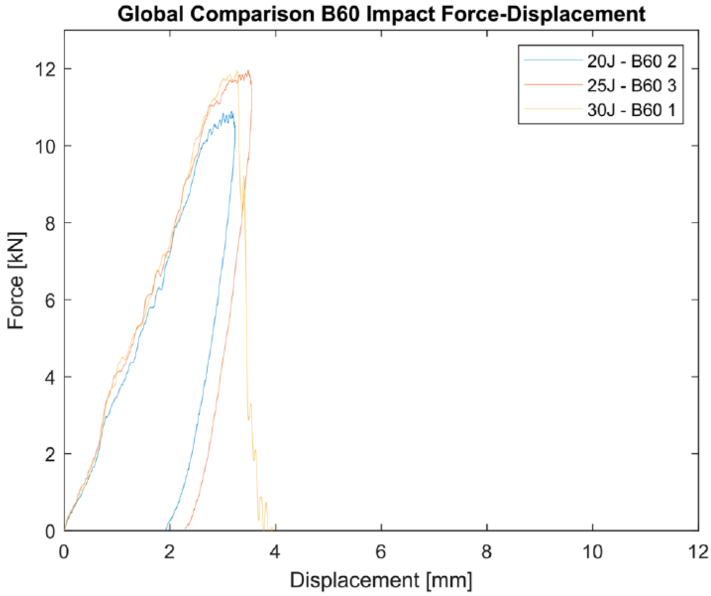

(c)

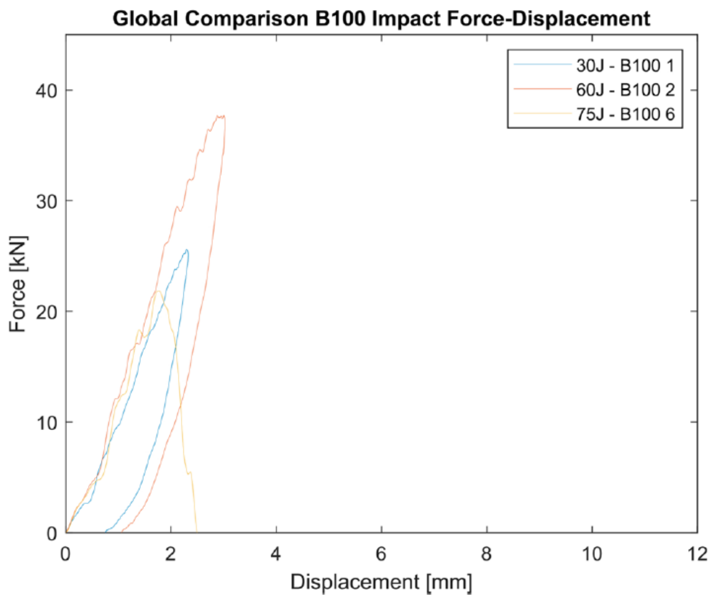

(d)

Figure 78: Bulk force-displacement curves. (a) B10; (b) B40; (c) B60; (d) B100 [168].

Comparing the foam and grad structures (Figure 77 and Figure 88) it is possible to notice an increase in the maximum load of the foam structures going from specimen F1 to F3, indicating an increasing rigidity upon the impact of the material also indicated by the greater slope of the linear section of the curve.
The first maximum load of approximately 2000 N is reached for the F1 specimen, while higher values are recorded for F2 and F3, justified by their greater density. For all foamed structures, complete penetration occurred between 25 J and 30 J (as reported in bold in Table 27).
It is important to underline that the first maximum load corresponds to the failure of the upper skin and appears to be independent of the impact energy. About the F3 samples for all impacted energies, a first change in the linear pendency can be observed at about 1 ms due to the upper skin failure, while several important drops of loads were recorded due to the interaction of the impactor with the core of the sample.
The velocity-time plot provides relevant insights into the material's ability to decelerate and stop the impacting mass, as shown in Figure 79 for the foam specimens. For example, at 25 J the F1 specimen undergoes total perforation and is unable to stop the mass: the velocity decreases but never reaches zero. The same trend is observed at higher energies for the other specimen types. However, for energy values less than the penetration ones, the F1 samples slow down the mass in a range of time greater than the other structures since the more important damage recorded.
Figure 80 shows the velocity-time curves of bulk specimens. For low values of impact energy each specimen can stop the mass, and the deceleration is faster the higher the density of the specimen.

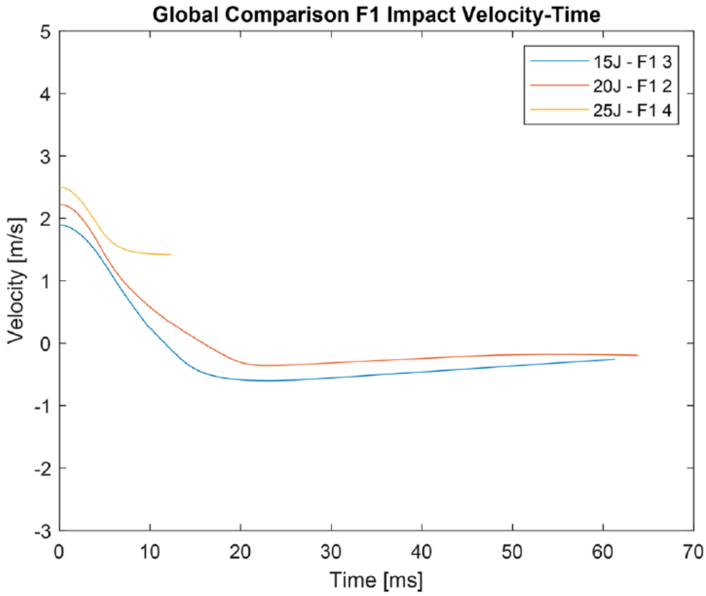
Global Comparison F1 Impact Velocity-Time
15J - F1 3
20J - F1 2
25J - F1 4
Velocity [m/s]
Time [ms]
5
4
3
2
1
0
-1
-2
-3
0
10
20
30
40
50
60
70

(a)

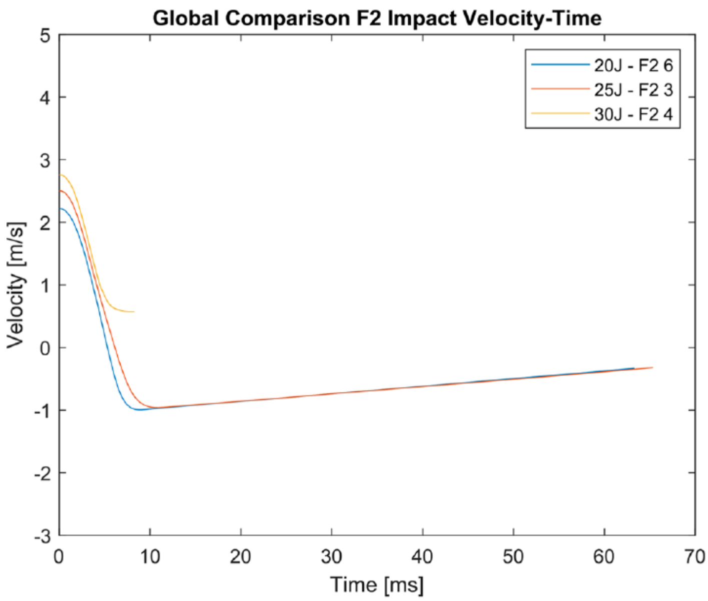
Global Comparison F2 Impact Velocity-Time
20J - F2 6
25J - F2 3
30J - F2 4
Velocity [m/s]
Time [ms]
5
4
3
2
1
0
-1
-2
-3
0
10
20
30
40
50
60
70

(b)

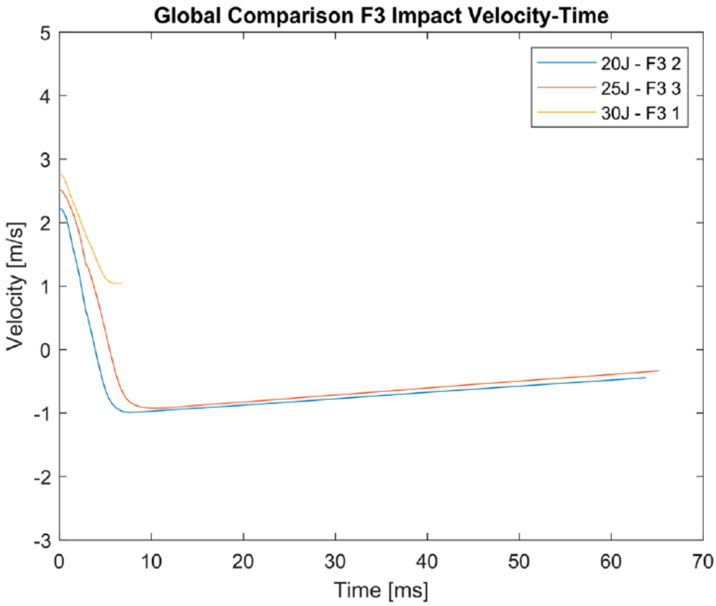

(c)

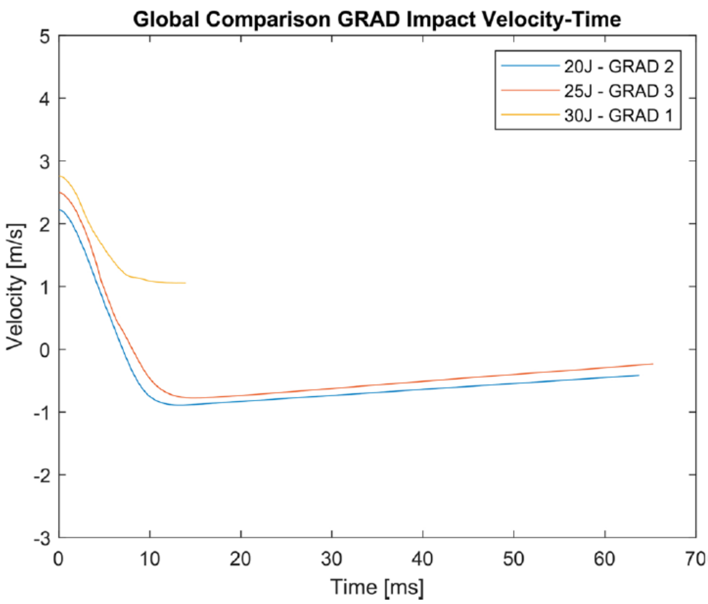

(d)

Figure 79: Foam velocity-time curves. (a) F1; (b) F2; (c) F3; (d) GRAD [168].

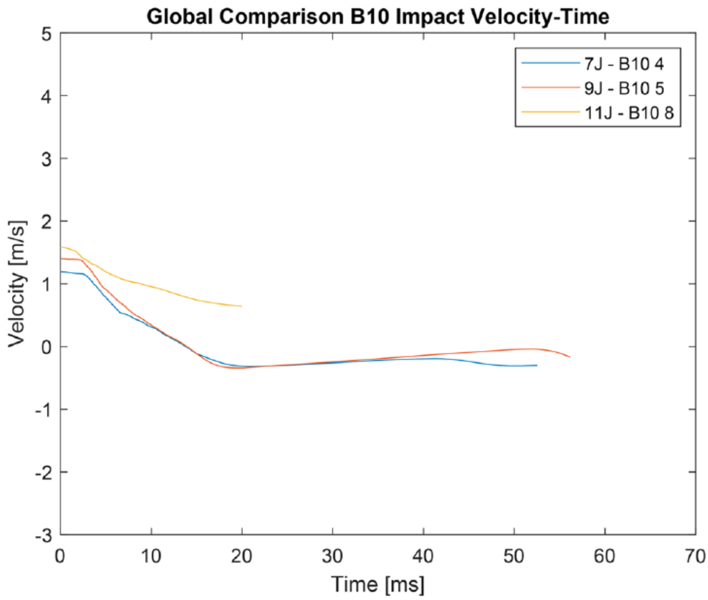
Global Comparison B10 Impact Velocity-Time
Velocity [m/s]
Time [ms]
7J - B10 4
9J - B10 5
11J - B10 8
5
4
3
2
1
0
-1
-2
-3
0
10
20
30
40
50
60
70

(a)

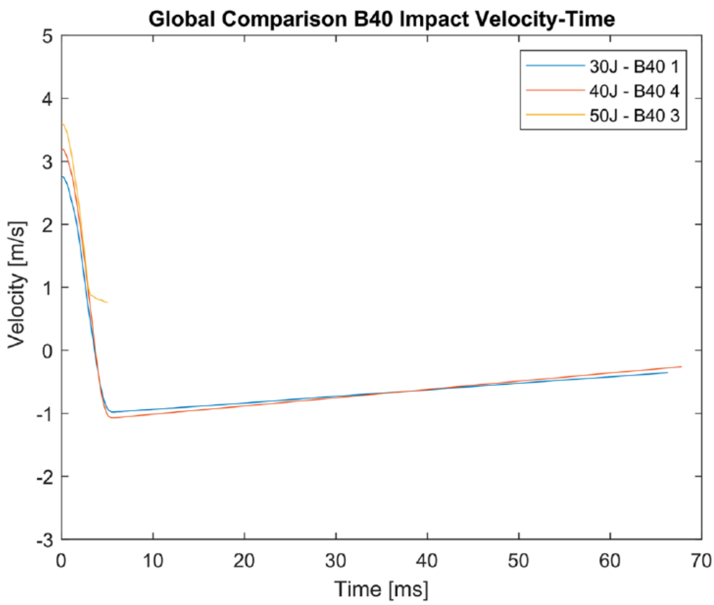
Global Comparison B40 Impact Velocity-Time
Velocity [m/s]
Time [ms]
30J - B40 1
40J - B40 4
50J - B40 3
5
4
3
2
1
0
-1
-2
-3
0
10
20
30
40
50
60
70

(b)

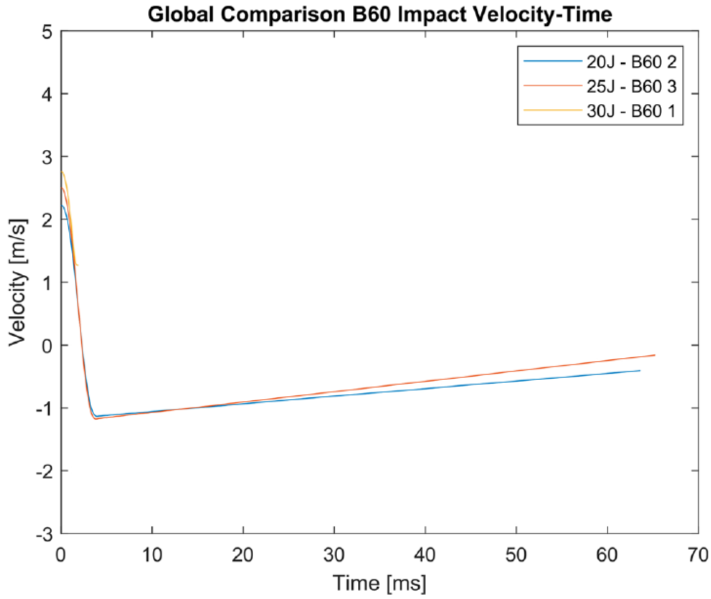

(c)

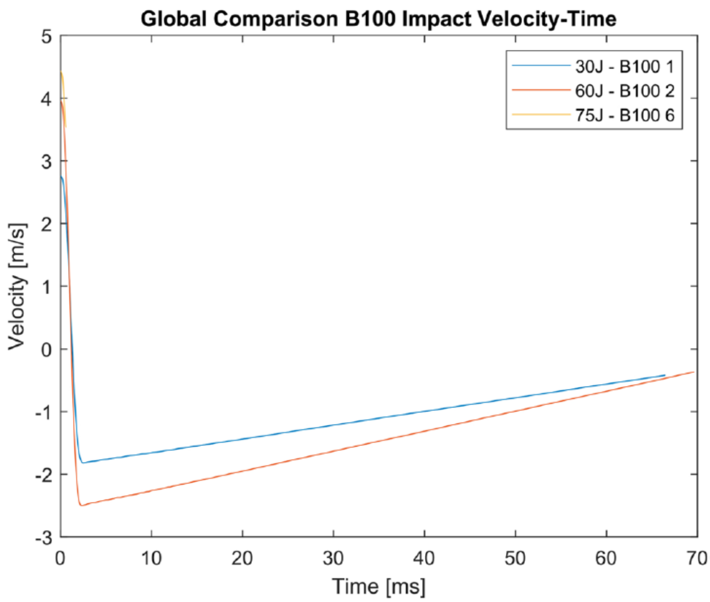

(d)

Figure 80: Bulk velocity-time curves. (a) B10; (b) B40; (c) B60; (d) B100 [168].

Table 27 summarizes the main results of the impact tests, including the applied impact energy (E_{test}), maximum force (Fmax), displacement at maximum force (δ_{Fmax}), total energy absorbed (TEA), and specific energy absorption relative to mass (SEA_m) and density (SEA_ρ). Results highlight that the best performance in terms of specific energy absorbed was achieved by the bulk specimen B40. For foamed specimens, the highest SEA_ρ was observed in the F1 specimen tested at 25 J.

When comparing foamed and bulk specimens of the same density, it emerges that at low densities (F1 vs. B10) similar maximum load values are reached, but the displacement at maximum force is larger for foamed specimens. Moreover, higher perforation energies are recorded for F1. At medium densities (F2, GRAD, and B40), bulk specimens show higher perforation energy and maximum load values, though with lower displacement values. At high densities (F3 and B60), the same perforation energy and similar values of displacement relative to the maximum force are recorded, but higher peak maximum force for bulk specimens.

The failure modes of the specimens after the impact tests were analysed by high-resolution optical microscopy. Figure 81 reports the optical images and scanning electron micrographs of the foamed specimens. The morphology of the foam core was observed before and after the tests, allowing a direct correlation with the load-displacement curves.

Table 27: Low-velocity impact test results [168].

Type	Test n°	E_{test} [J]	F_{max} [kN]	δ_{Fmax} [mm]	TEA [J]	SEA_m [J/kg]	SEA_ρ [J m^3/kg]
F1	3	15	1.89	9.47	12.43	526.31	0.04
	2	20	2.12	9.33	18.67	763.63	0.05
	4	**25**	**1.79**	**8.21**	**19.57**	**838.58**	**0.06**
F2	6	20	4.89	7.36	15.76	385.47	0.03
	3	25	4.33	7.06	20.88	519.28	0.04
	4	**30**	**4.57**	**7.99**	**28.22**	**702.60**	**0.05**
F3	2	20	6.57	4.38	14.94	256.70	0.02
	3	25	5.97	5.83	20.98	373.38	0.03
	1	**30**	**3.51**	**3.61**	**25.37**	**449.01**	**0.03**
GRAD	2	20	3.44	7.28	15.75	378.96	0.03
	3	25	4.10	8.94	21.85	517.33	0.04
	1	**30**	**3.28**	**7.08**	**25.98**	**621.80**	**0.04**
B10	4	7	1.80	4.12	4.88	198.71	0.01
	5	9	2.00	4.89	7.40	308.24	0.02
	8	**11**	**1.44**	**3.40**	**9.57**	**379.32**	**0.03**
B40	1	30	8.84	5.33	25.45	599.89	0.04
	4	40	9.39	7.19	35.53	849.80	0.06
	3	**50**	**9.89**	**6.98**	**47.11**	**1087.15**	**0.08**
B60	2	20	10.90	3.17	13.81	244.61	0.02
	3	25	11.96	3.48	18.45	321.07	0.02
	1	**30**	**11.94**	**3.27**	**22.80**	**397.33**	**0.03**
B100	1	30	25.63	2.29	16.18	178.83	0.01
	2	60	37.72	2.88	35.44	392.32	0.03
	6	**75**	**22.87**	**1.77**	**26.92**	**295.33**	**0.02**

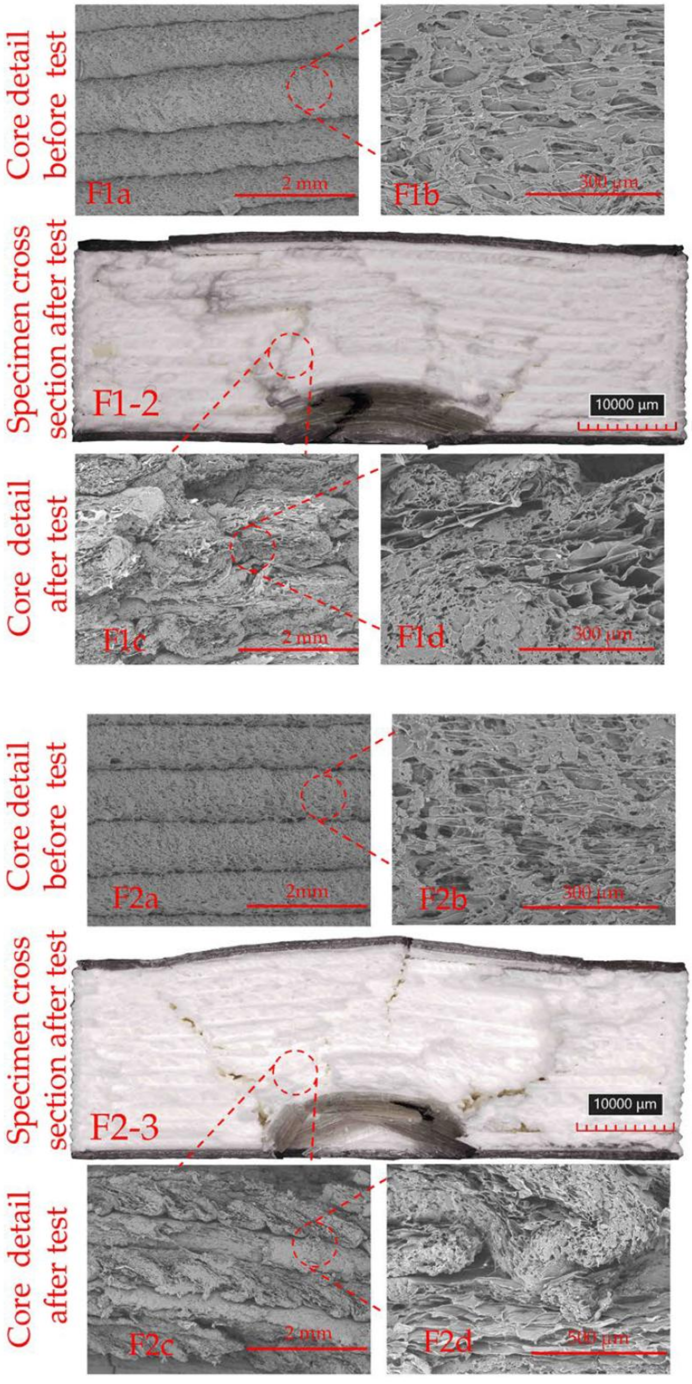

Core detail before test
F1a
2 mm
F1b
300 µm
Specimen cross section after test
F1-2
10000 µm
Core detail after test
F1c
2 mm
F1d
300 µm
Core detail before test
F2a
2mm
F2b
300 µm
Specimen cross section after test
F2-3
10000 µm
Core detail after test
F2c
2 mm
F2d
500 µm

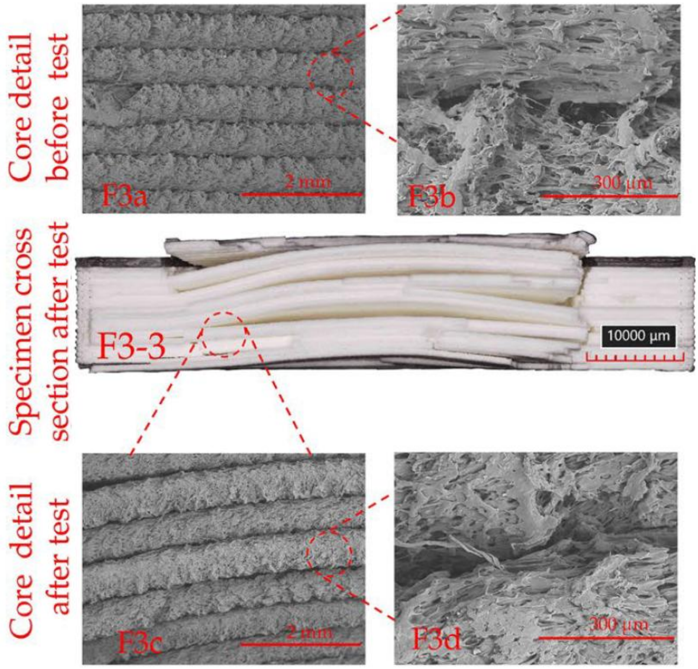

Figure 81: Optical and scanning electron microscopies of the section of the foam sandwich structures after LVI [168].

F1 specimens showed a clear foam cell collapse, which represents the main energy absorption mechanism. The same behaviour was observed in F2 specimens, whose higher density gives a lower size of the pores. The global failure of F1 and F2 specimens is dominated by upper skin indentation, core densification, and out-of-plane displacement of the bottom skin. Intralaminar cracks in the core exhibited the typical pine-tree pattern of thick laminates [194]. The ability to give out of plane displacements generally characterizes a structure prone to energy adsorption [195].

F3 specimens experienced a different failure mode, where both displacement and indentation were very limited. Due to the higher stiffness of the specimen, the inability to bend caused the breakage of the layers bonding. Moreover, at higher optical magnitude, the failure mechanism of the core highlights that the densification didn't occur as in the F1 and F2 typologies. The progressive interlayer bonding failure is also visible in the force-displacement curve, where several load drops were recorded during the impact tests.

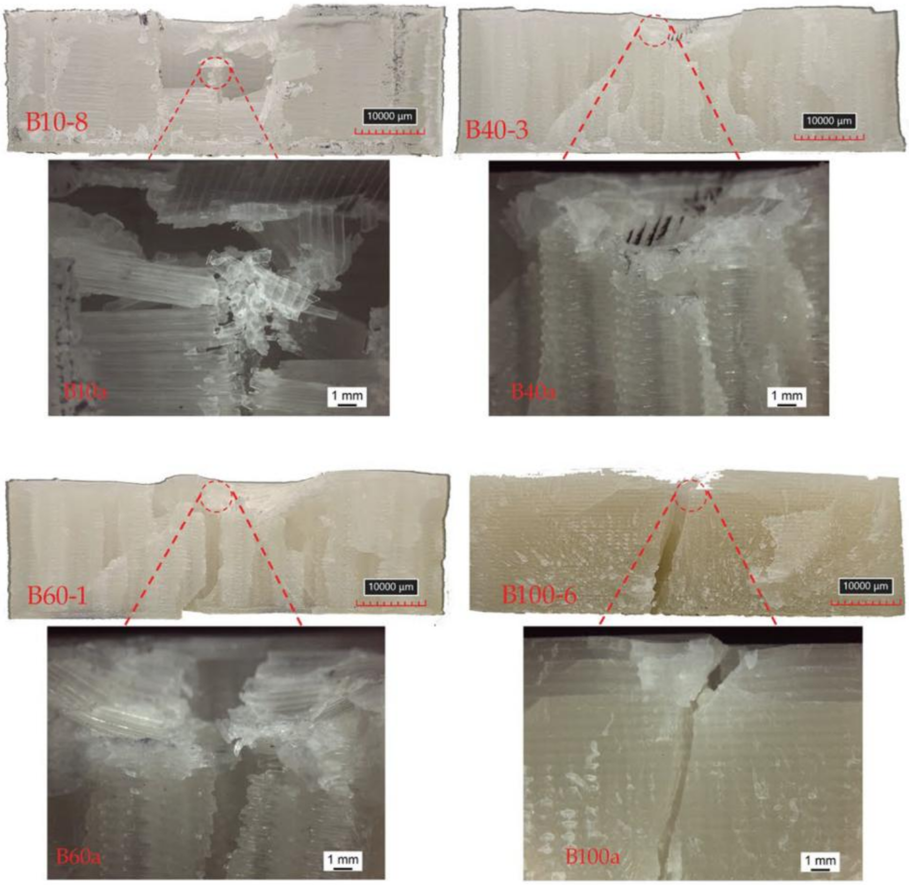

Figure 82: Visual inspection and microscopic images of bulk specimens' section after LVI [168].

For the bulk series, Figure 82 shows that B10 specimens failed mainly through fracture of the honeycomb cell walls. The corresponding micrograph (B10a) highlights the delamination of the layers. In contrast, for the specimens B40a, B60a, and B100a, the reduced cell size inhibits delamination. Instead, horizontal crack propagation was observed, indicating a different failure mechanism compared to lower-density specimens.

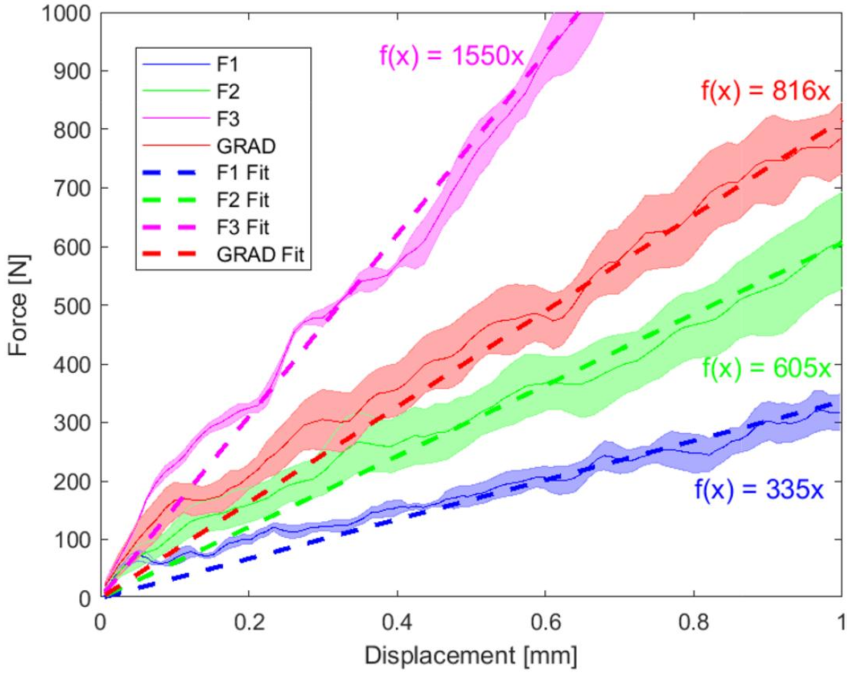

Figure 83: Force-displacement curves linear part for each foam specimen. The shaded error bars indicate the standard deviation calculated on each repetition [168].

By analysing the force-displacement curves, the average value of the slope in the linear region was extracted. Figure 83 illustrates how the greater stiffness of the material is found in the F3 family specimens, followed by the F2 and GRAD families, where the value of the angular coefficient is quite similar. Finally, in the F1 family specimens, this value is low due to the lower density. The stiffness values are summarized in Table 28.

Table 28: Stiffness values for the foamed specimens [168].

	K [N/mm]
F1	335
F2	605
F3	1550
GRAD	816

Table 29 shows the peak accelerations of the specimens at the impact energy causing total perforation. The results confirm that the tested specimens can be used as cushioning materials to reduce impact damage, for instance in agricultural harvesting [196]. Considering peak accelerations, peak loads, impact duration (i.e., the time over which energy transfer occurs), and deformation capacity under load, F2 specimens demonstrated the most balanced mechanical behaviour [197].

Table 29: Peak acceleration value for each specimen type [168].

	a [m/s^2]
F1	288
F2	589
F3	811
GRAD	557
B10	272
B40	128
B60	163
B100	513

An additional relevant property is illustrated in Figure 84, which reports the specific absorbed energy normalised by density. Considering the overall results from impact tests and failure modes, F2 specimens achieved a SEA_ρ value comparable to other sandwich structures reported in [44]. Although this value is lower than that of multilayer trapezoidal corrugated and honeycomb aluminium sandwiches, it is like that of plywood-core structures with GFR or CFR skins.

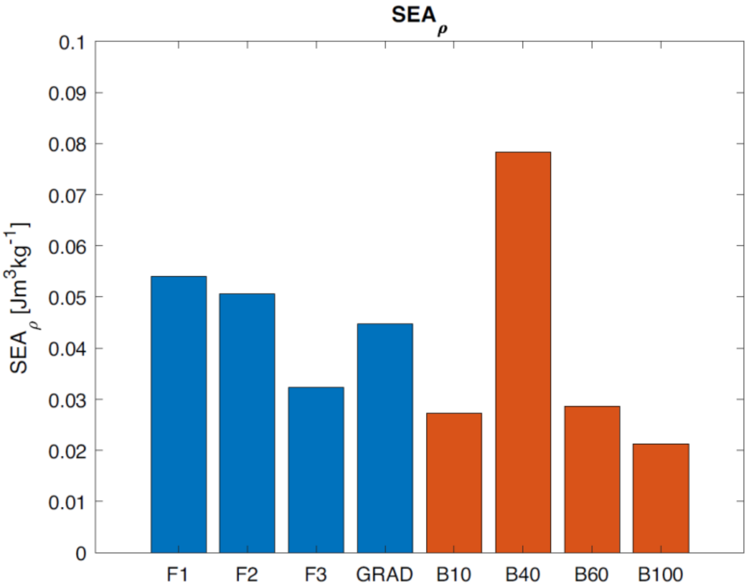

Figure 84: Specific energy absorbed comparison [168].

Figure 85 shows the trend of loads (solid curves) and energies (dashed curves) as a function of displacement, at energy levels close to specimen failure. In foamed specimens (Figure 85(a)), the initial slope change of the energy-displacement curve corresponds to the failure of the upper skin (around 1 mm displacement), followed by multiple variations due to the interaction between the impactor and the core. A similar behaviour was observed in bulk specimens B10, B40, and B60, where the initial slope change corresponds to upper skin failure and subsequent changes to core failure (Figure 85(b)). In contrast, the B100 sample showed an initial slope change followed by a linear trend.

Figure 86 shows the force-displacement curves of the impact tests at the energy that causes the total perforation of the specimens. It can be observed that for foamed specimens F1 and GRAD, the striker is able to fully penetrate the specimens. For specimens F2 and F3 the striker only reaches

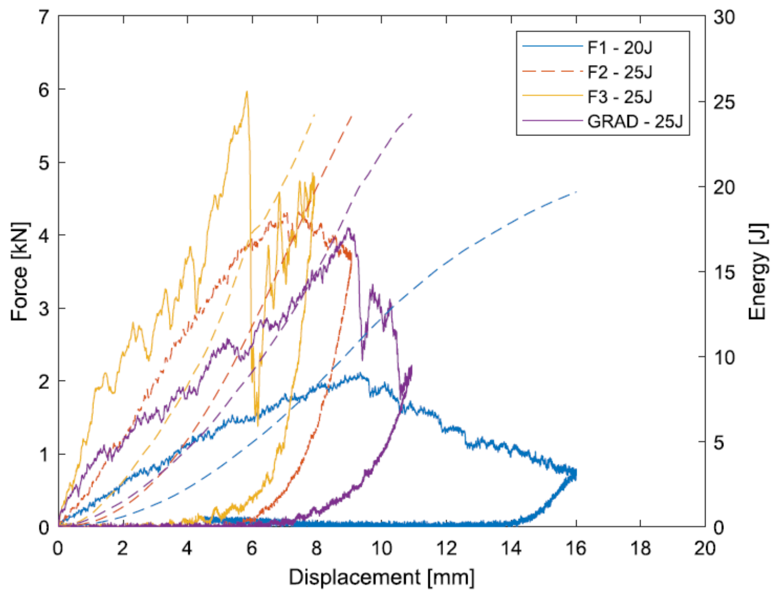

(a)

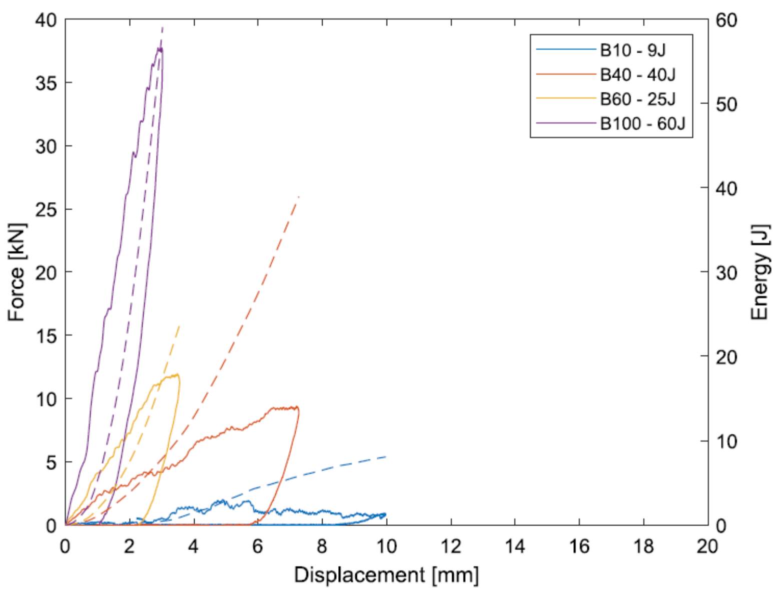

(b)

Figure 85:Force-energy-displacement curves at lower perforation energy [168]. (a) foam specimens; (b) bulk specimens.

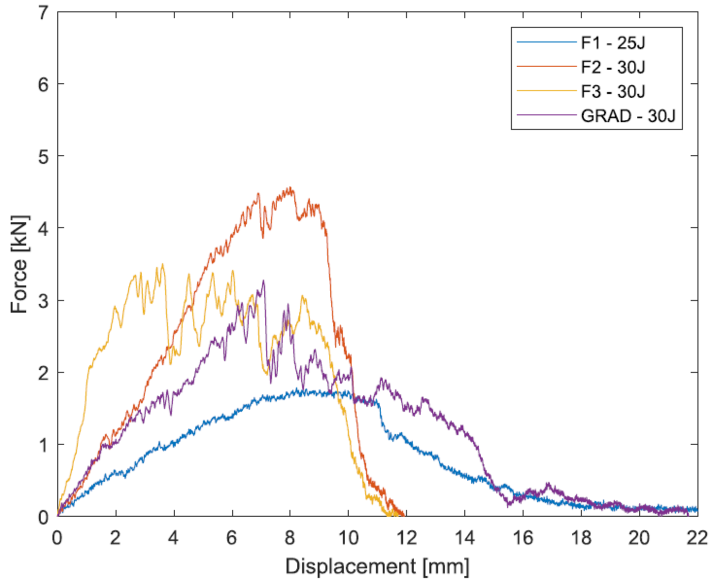

(a)

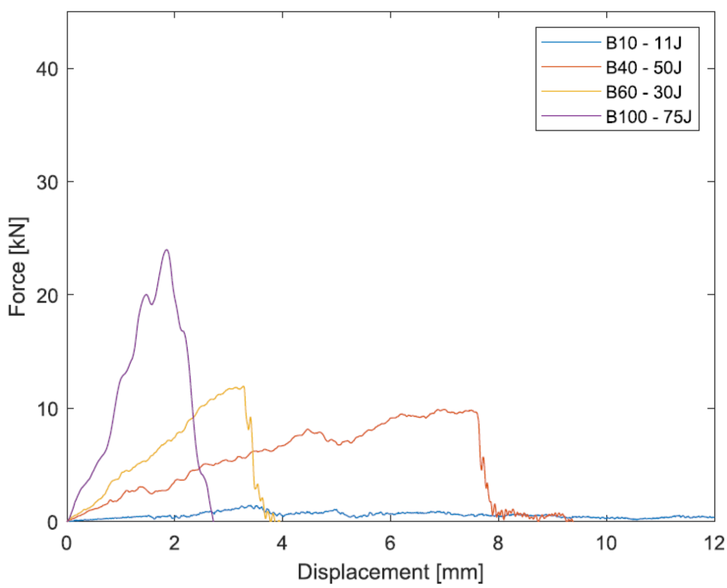

(b)

Figure 86: Comparison of force-displacement curves for foam [168]. (a) and bulk (b) specimens at perforation energies.

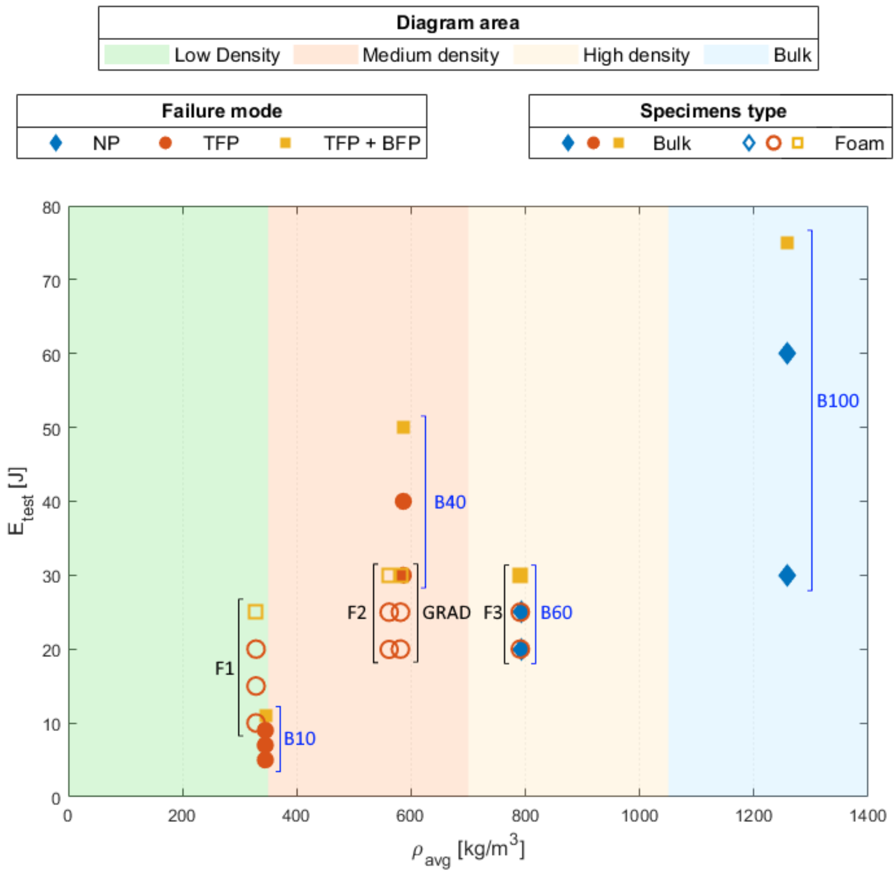

Figure 87: Failure map comparison in Energy-Density plane for the different type of specimen. Figure adapted from [168].

A failure mode map is shown in Figure 87, which allows the different mechanisms to be analysed as a function of density and impact energy. Diamond, circle, and square markers indicate non-perforation (NP), top-face perforation (TFP), and total perforation (TPF + TFP), respectively. For comparison, filled markers correspond to bulk specimens and empty markers to foamed ones. In the low-density region, the energy required for the total perforation of the foam F1 specimen is 127% higher than for bulk B10. In the medium-density region, foam F2 and GRAD specimens required almost the same energy for upper skin and total perforation, while the bulk B40 required 67% more. In the high-density region, both foam F3 and bulk B60 failed at the same perforation energy (30 J). Importantly, bulk specimens showed a much more brittle behaviour compared to foams, with a sudden transition from non-perforation to total perforation (as also observed for B100).

6. Discussion

This chapter discusses and interprets the results presented in the previous sections, providing a comparative assessment of the energy absorption capabilities of different sandwich configurations and a comprehensive understanding of their mechanical behaviour under various loading conditions.

6.1 Dynamic scaling factor and energy absorption: AHS vs composite sandwiches

The evaluation of the mechanical properties of aluminium honeycomb sandwich specimens, carried out through QS perforation and LVI tests, together with the analysis of the corresponding failure modes by visual inspection and digital radiography, has highlighted the potential for replacing traditional composite-skin sandwiches, which are more difficult to recycle at end of life. The numerical results in terms of absorbed energy have also enabled the definition of a coefficient capable of estimating the dynamic behaviour of the analysed structures starting from simpler and more cost-effective static tests.

In this context, a specific analysis was conducted to compare the perforation energies obtained from QS and LVI tests, with the aim of establishing a quantitative relationship between the two loading conditions. This comparison was motivated by the fact that QS perforation testing is simpler, requires less specialised equipment, and provides results that are easier to interpret. To this end, a Dynamic Scaling Factor (DSF) was introduced, defined as the ratio of LVI to QS perforation energies:

$$DSF = \frac{TEA_{LVI,perf}}{TEA_{QS,erf}} \tag{49}$$

The results of this analysis are summarised in Table 30.

Table 30: Results of upper and lower face perforation, for both tup geometries (H10 hemispherical and conical), in terms of TEA and DSF values

	Hemispherical TEA_{Perf}			**Conical TEA_{Perf}**		
	QS (J)	LVI (J)	DSF	QS (J)	LVI (J)	DSF
Upper face						
AHS h11	21.8	22.1	1.01	28	28.9	1.03
GFRP PVC	5.5	8.1	1.47	6.9	8.7	1.26
AHS h32	19.7	20.6	1.05	26.9	30.5	1.13
GFRP balsa	14.1	17.7	1.26	11.9	22.9	1.92
Lower face						
AHS h11	43	48	1.12	61	65	1.07
GFRP PVC	54	80	1.48	85	100	1.18
AHS h32	70	80	1.14	99	110	1.11
GFRP balsa	191	210	1.10	198	260	1.31

All DSF values are equal to or greater than unity, confirming that higher perforation energies are required under dynamic loading compared to QS conditions. For AHS structures, DSF values are between 1.0 and 1.15 in all cases, showing that for this sandwich solution the energy absorbed in QS tests is close to that from LVI tests and hence QS tests may be used to conservatively predict LVI perforation energies with a DSF of 1.2, or less conservatively (but still within the bounds of experimental variation) of 1.1. Except for the thicker AHS with conical indentation at top face perforation, the differences between QS and LVI are minimal, with a DSF close to 1.0. In general, the DSF of full perforation of the AHS is approximately 1.1, indicating that the crushing of the honeycomb core possibly adds some form of rate dependence to the damage mechanisms.

In all cases except for full perforation of the GFRP/balsa laminate with the H10 hemispherical tup, the DSF values of the composite sandwich laminates are greater than those of their equivalent AHS, and in that case AHS and composite laminates do not differ greatly. Hence, the composite failure modes appear to be more rate dependent than those of their relevant AHS counterparts. The known viscoelastic behaviour of PVC foam will also contribute to this, and in fact perforation of the upper face with the hemispherical tup involves significant compression of the underlying PVC foam, resulting in higher GFRP/PVC hemispherical DSF values compared to their GFRP/Balsa counterparts. However, for the conical tup, where far more lateral compression occurs, the GFRP/Balsa DSF values become even larger than their GFRP/PVC counterparts.

Table 30 shows that DSF values for composite sandwiches range from 1.1 (full perforation of GFRP/balsa with H10 hemispherical tup) to 1.9 (upper face perforation of GFRP/balsa with conical tup), reflecting more complex failure modes and higher rate-dependent behaviour for composites than for AHS. DSF values of 1.5 and 1.25 give conservative estimates of LVI tests from QS tests for hemispherical and conical perforation, respectively, for both upper face and full sandwich GFRP/PVC perforation. However, for the GFRP/Balsa laminates, only trends are evident; there is more loading rate effect for the conical tup than for the hemispherical one, and less loading rate effect for full sandwich perforation than for that of the upper face only.

These DSF results provide a framework to correlate QS and LVI responses. To extend the discussion, comparing the absorbed energies (both total and specific) allows a more complete evaluation of the relative performance of the different sandwich configurations.

The relative energy absorption abilities of each sandwich solution were compared for both tup geometries (hemispherical and conical) and for upper face and full sandwich perforations, in terms of both TEA and SEA_{ρ} (Figure 88-Figure 91). All figures confirm the DSF ≥ 1 trend, confirming the higher energy required under dynamic loading.

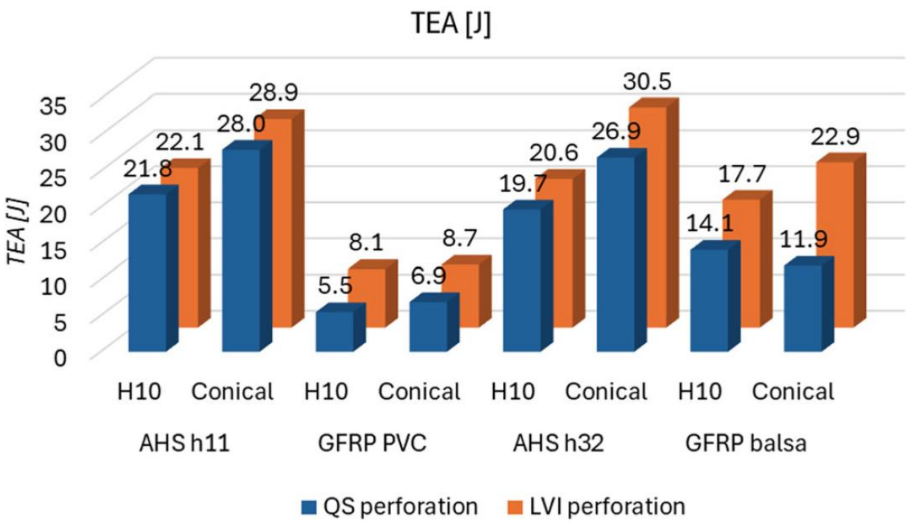

Figure 88: Upper face perforation TEA [165]

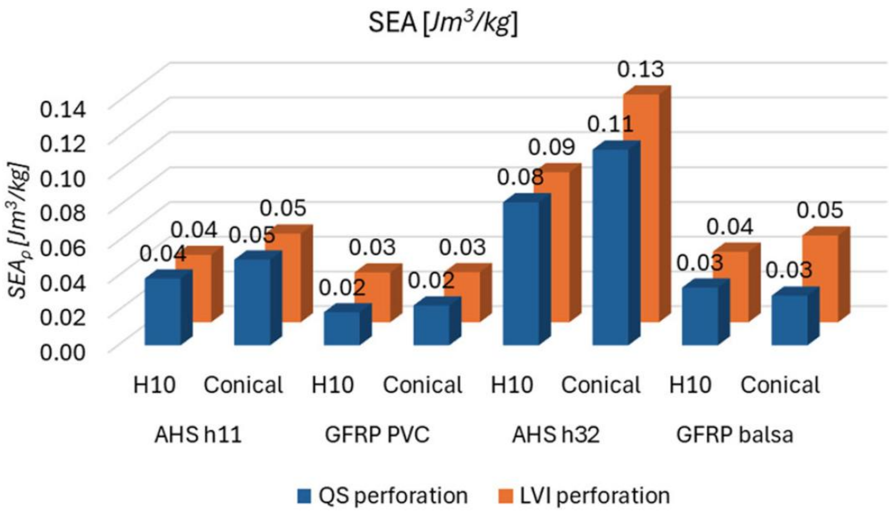

Figure 89: Upper face perforation SEA_{ρ} [165]

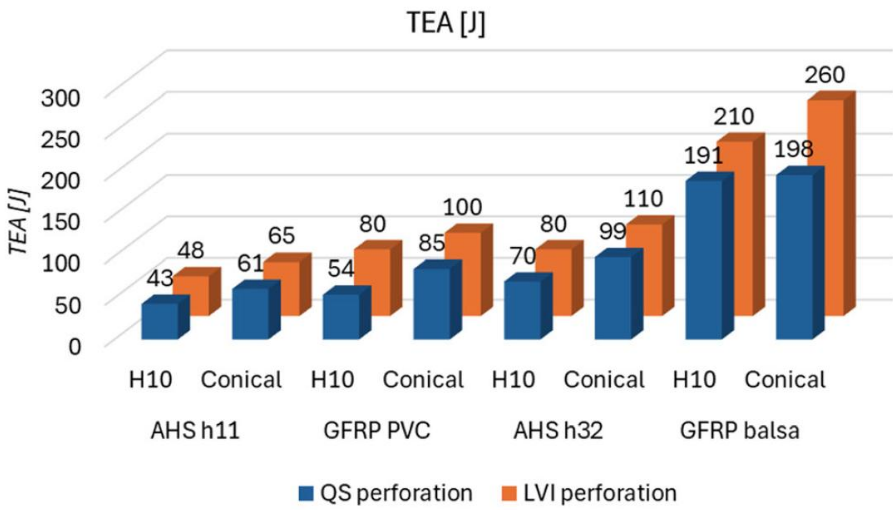

Figure 90: Full sandwich perforation TEA [165]

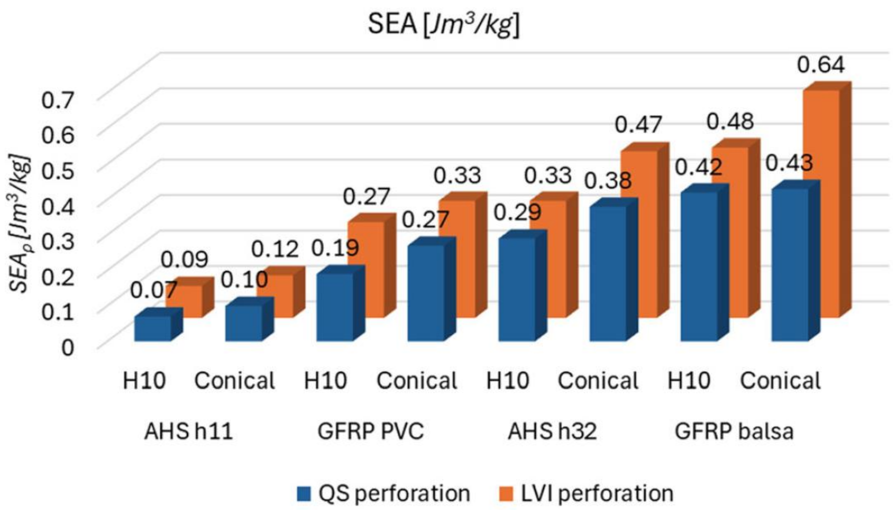

Figure 91: Full sandwich perforation SEA_ρ [165]

For upper face perforation, which is arguably the most critical design failure mode, AHS panels are significantly better energy absorbers in all cases, especially for the thinner, lighter design case (Figure 88). As expected, the conical tup induced higher energy absorption than the hemispherical one, due to the more severe damage introduced. The thinner/lighter and thicker/heavier AHS cases absorb generally similar levels of energy, perhaps to be expected as the faces are identical in each case, the core only differs in thickness between the two, and the specimen geometry does not allow significant global deformations, even in the thinner case. However, the thicker balsa-cored composite sandwich (irreversibly) absorbs significantly more energy, around twice as much, as the thinner PVC-cored laminate for top face perforation. This would also be expected as the balsa is far stiffer and more brittle than the PVC, with the PVC no doubt suffering far less permanent damage up to this upper face perforation only failure level.

When energy absorption is normalised by density (Figure 89), the comparison takes on greater relevance for lightweight design applications, where weight efficiency and stability are crucial. For the lighter/thinner case, the normalised energies put the composite solution closer to AHS, though AHS still absorbs roughly twice the specific energy of the composite PVC sandwich. For the thicker/heavier case, considering density increases the advantage of AHS over balsa to about three times the specific energy absorbed.

A broader perspective is obtained by examining full sandwich perforation (Figure 90). As expected, both AHS and composite structures absorbed more energy in the thicker than in the thinner case. Interestingly, the thinner composite case absorbs more energy than does the thicker AHS case, although both become approximately equal in this capacity when the data is normalised by density in Figure 91, which shows a steady increase in absorbed energy from AHS h11 to GFRP/PVC to AHS h32 to GFRP/Balsa.

Contrary to the trend seen for upper face perforation only, Figure 90 shows that the composite sandwich solution absorbs more energy than the equivalent AHS solution for full sandwich perforation both thinner and thicker panels. Normalising absorbed energy by density (Figure 91) generally increases the advantage of composites over AHS for thinner/lighter designs, while slightly reducing it for thicker/heavier designs.

6.2 Performance evaluation of hybrid aluminium honeycomb sandwich panels with FFRP and BFRP skins

Although aluminium honeycomb sandwich panels have demonstrated good mechanical properties and offer several advantages, such as lightweight design and excellent recyclability, the potential benefits of hybridising these structures with natural fibre skins were systematically investigated. Hybridisation was achieved by introducing natural fibre skins with the aim of enhancing specific mechanical characteristics, including energy absorption, stiffness, and impact resistance, while also improving the performance of the panels.

Table 31: Low-velocity impact results summary (H20 hemispherical tup). All specimens have honeycomb cell size core of 6 mm.

	AHS	**GFRP/AHS**	**FFRP/AHS PU adhesive**	**FFRP/AHS ER adhesive**	**BFRP/AHS**
E [J]	F_{max} [kN]	F_{max} [kN]	F_{max} [kN]	F_{max} [kN]	F_{max} [kN]
56	7.86	8.35	8.61	8.59	-
88	7.95	12.87	10.10	9.48	-
125	8.46	17.91	10.56	10.62	-
~ 180	-	16.81	8.86	10.10	17.95
230	-	-	-	-	19.63
~ 250	-	20.32	-	-	21.35

Impact tests were conducted using H20 hemispherical tup on panels with 6 mm and 3 mm honeycomb core cells size to quantify the influence of hybrid skins. Table 31 summarises the results for the 6 mm honeycomb cell size panels, comparing AHS [187], GFRP/AHS [109], FFRP/AHS (with PU and ER adhesives), and BFRP/AHS configurations.

At the lowest impact energy (56 J), FFRP skins increased the maximum load by ~8 % relative to AHS and ~3 % relative to GFRP/AHS specimens. At higher impact energies (88, 125, and 180 J), the differences between GFRP/AHS and FFRP/AHS specimens become more evident, with GFRP/AHS exhibiting higher increments in maximum load. At a ~180 J, where BFRP/AHS specimens were also tested, the basalt skins provided the highest performance, with a maximum load up to 46 % higher than FFRP hybrids and ~6 % higher than GFRP/AHS panels.

An additional comparison at approximately 250 J shows that BFRP/AHS panels still outperform their counterparts, with a maximum load about 5 % greater than that of the GFRP/AHS specimens.

A further comparison was carried out on sandwich structures with a honeycomb core cell size of 3 mm, as reported in Table 32. In this case, three configurations were analysed: non-hybrid AHS, GFRP/AHS, and BFRP/AHS specimens. All the panels were tested under impact loading using the H20 indenter, ensuring consistency with the results previously discussed.

Table 32: Low-velocity impact results summary (H20 hemispherical tup). All specimens have honeycomb cell size core of 3 mm.

	AHS	**GFRP/AHS**	**BFRP/AHS**
E [J]	F_{max} [kN]	F_{max} [kN]	F_{max} [kN]
56	9.70	11.49	-
88	9.38	13.21	-
125	9.65	13.30	-
~ 180	-	14.48	11.75
~ 230	-	14.25	13.48

By analysing the two energy levels common to both hybrid configurations, it can be observed that, at approximately 180 J and 230 J, the maximum load is slightly higher for the GFRP/AHS specimens compared to the BFRP/AHS ones.

The experimental results can be summarized by considering the effect of weight on the mechanical performance of the hybridised structures. In this context, the highest SEA values obtained from the impact tests were calculated relative to the panel density and compared with available reference data for the corresponding AHS structures [74], [108], [109], [170], [177].

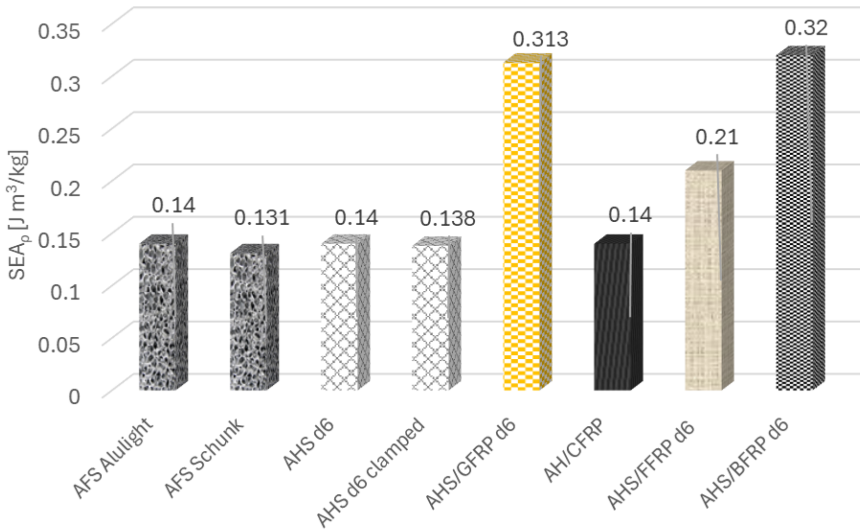

Figure 92: Maximum SEA$_\rho$ calculated by the impact tests compared with other sandwich structures with honeycomb cell size core of 6 mm.

All the data considered were obtained from tests performed with the H20 indenter and clearly highlight a significant improvement in performance when the sandwich structures are hybridised. As shown in Figure 92, the contribution of FFRP skins to energy absorption lies approximately midway between that of the fully aluminium sandwich and the GFRP/AHS configuration. This increment is also remarkable compared to high-performance carbon fibre hybridised AHS (+54%).

The addition of BFRP skins further enhances the energy absorption capabilities, showing the highest SEA values in both 6 mm and 3 mm honeycomb configurations. For the 6 mm honeycomb cell diameter (Figure 92), the performance of BFRP hybrids is substantially higher than that of non-hybrid honeycomb and carbon fibre-reinforced cores, and about 2 % higher than GFRP-reinforced specimens. The comparison between BFRP and FFRP hybrids indicates SEA values up to 46 % higher for the BFRP-reinforced panels. Similar trends are observed for the 3 mm cell configurations (Figure 93), with BFRP hybrids displaying significantly higher SEA compared to non-hybrid structures and about 7 % higher than GFRP-reinforced hybrids.

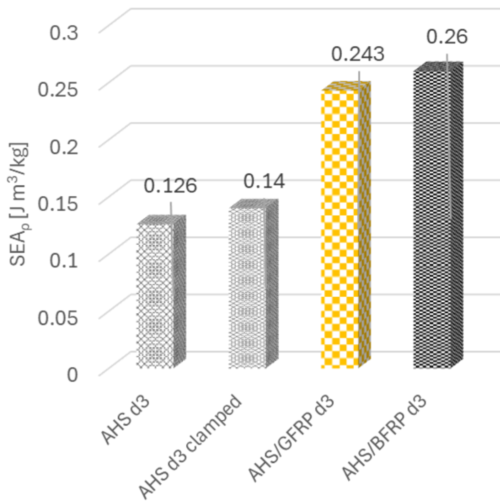

Figure 93: Maximum SEA_ρ calculated by the impact tests compared with other sandwich structures with honeycomb cell size core of 3 mm.

Overall, these findings demonstrate that hybrid aluminium honeycomb sandwiches with BFRP skins offer the best combination of stiffness, strength, and energy absorption, while FFRP skins provide a moderate improvement over conventional GFRP laminates. The superior performance of BFRP hybrids across different core sizes confirms their suitability for lightweight and impact-critical applications, providing a clear pathway for tailoring sandwich panel performance through fibre selection.

6.3 Foamed PLA sandwiches: flexural and energy response

Additive manufacturing, and particularly the Foam Additive Manufacturing process, enables the fabrication of innovative sandwich configurations using a single material. In this context, PLA was employed to produce mono-material sandwich specimens with foamed cores of different densities, allowing a systematic investigation of the influence of core density on both stiffness and energy absorption.

Flexural tests were conducted to evaluate both bending and shear stresses, and the relative flexural strength of each configuration was assessed by normalizing the maximum stresses against the bulk specimen (B100), following the Gibson-Ashby analytical model. The results showed that the F2 specimens achieved the highest maximum flexural stress (σ_{max}) among the foamed-core sandwiches (~79 MPa at 2 mm/min), outperforming the lower-density F1 (~33 MPa) and the high-density F3 (~76 MPa), demonstrating that an intermediate core density provides an optimal combination of stiffness and load-bearing capacity. The graded (GRAD) specimen exhibited intermediate behaviour (~54 MPa), indicating the potential of density gradients to tailor flexural response.

In Figure 94, a comparison is reported with literature data on sandwich structures produced with natural or recycled materials, including the F1, F2, F3 and Graded specimens from this study, alongside various reported configurations such as CFRP/PET foam [198], Flax/bottle caps [199], Wood/PLA [200], Paper/PLA [201], all-PLA honeycomb [153], Flax/PLA-HC [202], and CFRP-based (CITHSS [203] and CS16-20 [204]). It is highlighted that the F2 typology analysed here exhibits the highest relative flexural strength among all PLA-core sandwiches, being inferior only to the Flax/Bottle caps configuration by approximately 30 %. Moreover, the PLA foamed-core sandwiches investigated show interesting properties even when compared to other non-conventional sandwich arrangements, confirming the potential of these structures for applications requiring tailored mechanical performance.

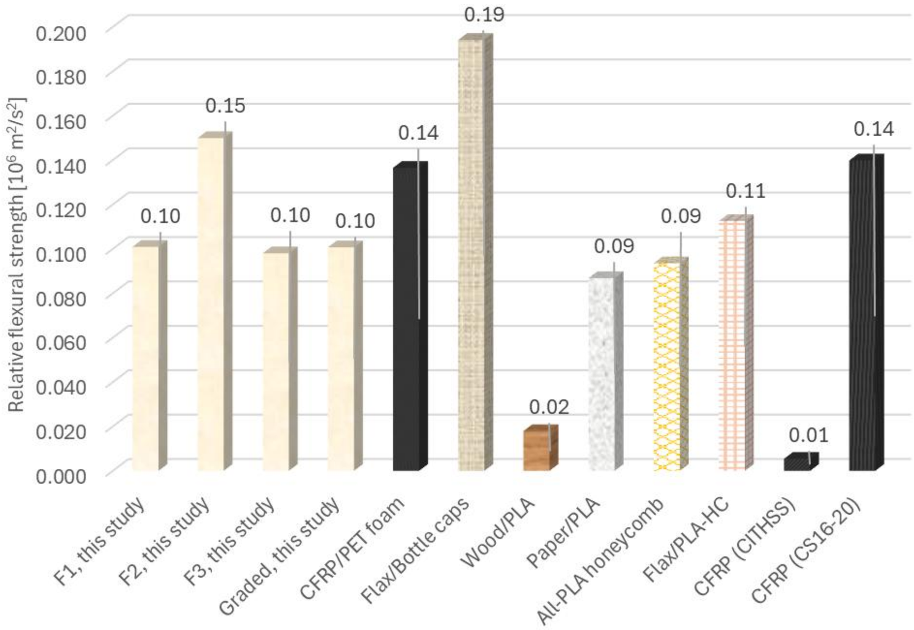

Figure 94: Flexural strength of the PLA sandwich analysed in this study compared with existing literature. Figure adapted from [189]

Impact tests were performed using H20 hemispherical tup to evaluate energy absorption under low-velocity impacts. The foamed specimens demonstrated a clear correlation between core density and absorbed energy: F1 (low density) exhibited the highest density-normalized absorbed energy (≈0.06 J·m³/kg), allowing large displacement, F2 (intermediate density) showed slightly lower SEA_ρ (≈0.05 J·m³/kg) with a balanced combination of stiffness and deformation, while F3 (high density) displayed limited deformation and the lowest SEA_ρ (≈0.03 J·m³/kg). This behaviour reflects the trade-off between stiffness and ductility: low-density cores deform more and absorb more energy per unit density, whereas high-density cores are stiffer but less capable of dissipating energy efficiently.

Comparison with bulk honeycomb PLA specimens (B10, B40, B60, B100) revealed that foamed cores provide higher displacement at peak load and better energy absorption at lower densities, while bulk specimens reach higher maximum forces but fail more brittlely. GRAD specimens, with a layered density arrangement, offered intermediate performance, suggesting that graded structures can be tailored for specific energy absorption requirements.

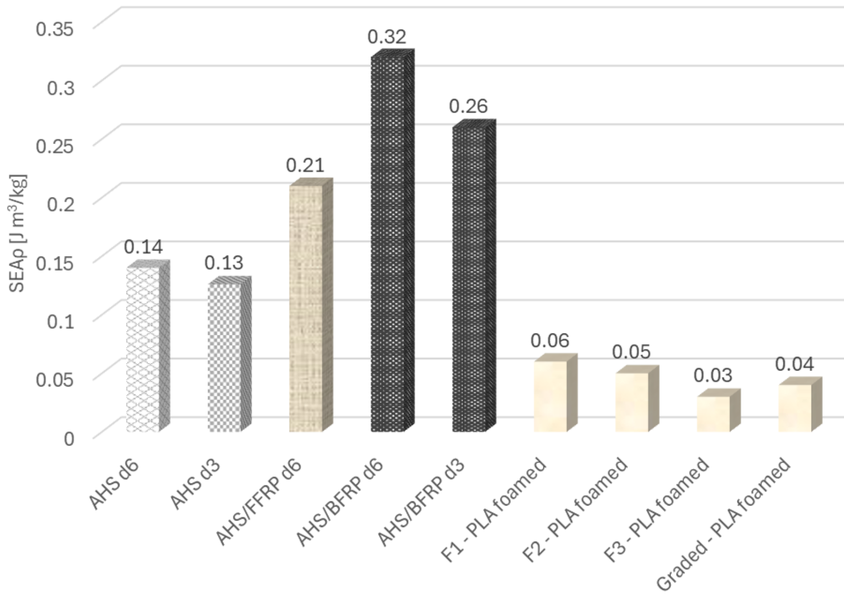

Figure 95: Maximum SEA_ρ comparison between foamed PLA, AHS and hybrid sandwich structures.

Although the application context of these PLA sandwiches differs from that of aluminium honeycomb or hybrid fibre-reinforced panels, the SEA provides a useful metric for comparison (Figure 95). Foamed PLA sandwiches exhibit performance levels suitable for lightweight and sustainable applications (e.g., food packaging), where low weight, impact absorption, and biodegradability are prioritized over the mechanical requirements of automotive or aerospace panels. While they do not compete with hybrid or metallic structures in terms of SEA_ρ, their behaviour is coherent and promising within their intended application scope.

7. Conclusions

This PhD thesis addressed the development and characterisation of lightweight and sustainable structural solutions, motivated by the growing demand for environmentally friendly technologies that reduce emissions, improve energy efficiency, and enable circular economy strategies.

An initial analysis of the sustainability scenario and of existing approaches to lightweight structures highlighted both the potential of advanced sandwich configurations and the gaps that remain to be bridged, thus guiding the experimental work presented in this thesis (Chapter 2).

The first task of the PhD work concentrated on all-aluminium honeycomb sandwich structures, selected for their recyclability, structural efficiency, and relevance to transport applications (Chapter 3). Their mechanical behaviour was studied under QS perforation and LVI, with particular attention to damage mechanisms and dynamic response. Based on experimental results, a Dynamic Scaling Factor was defined to estimate dynamic impact behaviour from QS tests, providing a practical and cost-effective method for predicting LVI performance.

Aluminium honeycomb sandwich structures were compared with conventional composite sandwich laminates, which are known to be highly susceptible to impact damage, a critical issue that can compromise structural integrity and reliability in demanding applications. Two design cases were considered: a thinner/lighter panel and a thicker/heavier one. Damage was evaluated using NDT X-ray digital radiography, and force-displacement data were correlated with complex, multiple, and progressive damage modes identified through both visual and radiological inspections.

For upper-face perforation, AHS solutions were significantly better energy absorbers than their composite equivalents, particularly for the thinner/lighter and more sustainable design case. Perforation with H10 hemispherical tup required 22 J for the thinner /lighter AHS, compared to 8 J for the GFRP/PVC composite sandwich, a substantial difference in energy absorption. In the thicker/heavier design, the total absorbed energy was similar for both materials (21 J for AHS vs 18 J for GFRP/Balsa). Both the thinner/lighter and thicker/heavier AHS solutions absorbed similar levels of energy for upper-face perforation. In contrast, the thicker balsa-cored composite sandwich absorbed roughly twice the energy of the thinner PVC-cored composite in the same test. Considering the specific absorbed energy (i.e., normalized by panel weight), the AHS still outperformed composites: about twice the specific energy for the thinner structures, and up to three times higher for the thicker design. For complete sandwich perforation (upper and lower faces), the general trend of increasing specific absorbed energy was observed from thinner to thicker structures, from hemispherical to conical tups, and from AHS to composite sandwiches. This confirms the superior and more predictable performance of AHS across design cases.

The DSF values confirmed that AHS behaviour is more predictable and less sensitive to impact velocity compared to composite laminates. For upper face perforation, AHS ranged from 1.0 to 1.1, while composites reached up to 1.9, indicating greater velocity sensitivity. For complete perforation, AHS values ranged from 1.07 to 1.14, whereas composites exhibited higher and more variable values, up to 1.5 in some cases. These findings provide practical guidance for using QS test data to predict more complex and costly dynamic impact behaviour via the DSF, which is particularly useful during early design stages when different materials and panel architectures need to be compared efficiently and reliably.

Aluminium honeycomb sandwich can provide a new and viable high-performance lightweight alternative to traditional composite solutions in terms of impact resistance, while simultaneously achieving far higher levels of sustainability. This makes AHS a valuable material choice in applications that emphasise weight reduction, energy efficiency, durability, and recyclability.

The second task of the PhD work focused on hybrid aluminium honeycomb sandwich structures, reinforced with natural fibre polymer skins, with the aim of enhancing mechanical performance while maintaining low weight and sustainability (Chapter 4). Flax fibre reinforced laminates (FFRP/AHS) and basalt fibre reinforced panels (BFRP/AHS) were bonded onto aluminium honeycomb cores using appropriate adhesives, creating recyclable hybrid solutions.

LVI tests on FFRP/AHS panels showed that the flax skins deform plastically together with the aluminium face sheets, dissipating energy through fibre breakage, matrix cracking, and indentation. Impact response depended on the impactor geometry: smaller contact areas (H10 tup) produced higher localized damage, with complete bottom skin perforation at around 56 J, whereas larger H20 tup required 180 J for full perforation. Epoxy-bonded specimens sustained higher loads due to stronger adhesion. Three-point bending tests highlighted the role of FFRP skins in flexural performance: for shorter spans (55-70 mm), local indentation dominated failure, whereas for longer spans (80-125 mm), core-shear and plastic hinge formation prevailed. Overall, FFRP hybridization improved maximum load by up to 8 % at low impact energies (56 J) compared to unreinforced AHS, with a corresponding increase in energy absorption.

QS perforation and LVI tests on BFRP/AHS panels revealed similar trends, with hybridization improving stiffness and energy absorption. Panels with 6 mm core cells were more effective than the 3 mm configuration, producing higher maximum loads, higher specific absorbed energy relative to panel density, and an extended linear part in the force-displacement curve, indicating larger deformation before failure.

Panels with 3 mm core cells reached peak forces of about 13 kN, while panels with 6 mm core cells reached 21 kN under comparable LVI damage conditions (top and bottom skin perforation). For 6 mm core cells, BFRP/AHS panels exhibited SEA values up to 46 % higher than FFRP/AHS and 2 % higher than GFRP/AHS, while for 3 mm cores the SEA was 7 % higher than GFRP/AHS. Failure mechanisms included top and bottom skin perforation, core buckling, and limited local debonding between fibre skins and aluminium sheets.

These results confirm that hybridising aluminium honeycomb sandwiches with natural fibre skins effectively enhances mechanical performance, particularly in terms of stiffness, impact resistance, and energy absorption, while preserving low weight and recyclability. FFRP skins provide a sustainable improvement in energy absorption with moderate performance gains, whereas BFRP skins provide the highest strength and energy absorption, making them ideal for high-performance applications.

However, by critically analysing these results, although basalt fibres have superior mechanical performance compared to flax and other natural reinforcements, their production process is considerably more energy intensive. Basalt fibre manufacturing involves extraction, crushing of the raw material (4-20 mm fraction), and melting at around 1500 °C, a process that demands high energy input and results in significant CO_2 emissions [205]. In addition, basalt fibres are generally more expensive than flax or glass fibres, although they remain less costly than carbon fibres [15]. These aspects highlight the need to balance mechanical advantages with energy and environmental considerations when evaluating basalt as a sustainable alternative among natural fibre reinforcements.

Despite the higher energy requirements, the high strength of basalt fibres can justify their use in high-performance hybrid laminates, where durability, strength, and structural reliability are critical.

The adhesives used to bond the composite skins to the aluminium cores, including commercial polyurethane and epoxy resins, also play a role in the overall environmental impact. These adhesives proved highly effective in ensuring excellent mechanical performance. While natural fibres and recycled aluminium enhance panel sustainability, the adhesives are not entirely green, even though only a very thin layer (~500 µm) is applied. From a scientific perspective, it would be valuable to investigate hybrid panels using more sustainable bonding solutions, such as bio-based epoxies or other green adhesives, to fully assess the environmental sustainability of these hybrid sandwich structures.

The final task of the PhD work focused on mono-material sandwich structures produced via Foam Additive Manufacturing using PLA, including both bulk and foamed-core specimens (Chapter 5). This study systematically investigated how core density affects bending and LVI behaviour across different foam configurations.

Flexural tests showed that foamed-core specimens generally absorb more energy and exhibit higher bending performance than bulk specimens, with the F2 configuration achieving the highest maximum flexural stress and providing an optimal combination of stiffness and strength among the foamed types. The F1 specimen, although lower in flexural stress, exhibited a more compliant behaviour. The graded specimen displayed intermediate flexural performance, indicating that density gradients can be effectively used to tailor stiffness and strength for specific applications. A clear correlation between the observed flexural stresses and the underlying failure mechanisms (face yielding, core shear, and interlayer debonding) was established, demonstrating that tailoring the foam density allows controlled deformation and energy dissipation.

LVI tests further demonstrated the advantages of foamed cores over bulk specimens. F2 specimens exhibited the highest maximum force values and a balanced combination of stiffness, deformation, and energy absorption compared to the other foamed specimens. F3 specimens displayed greater stiffness, followed by F2 and GRAD, whereas F1 showed the lowest stiffness due to its lower density. Impact observations indicated that foamed cores deform uniformly, dissipating energy through core indentation and controlled face-sheet bending, while avoiding the brittle failure typical of bulk PLA specimens.

The FAM process enables precise control of foam morphology and density gradients, allowing the mechanical performance of sandwich panels, including stiffness, deformation, and energy absorption, to be tailored for specific applications. Foamed PLA sandwiches are particularly suitable for lightweight and sustainable applications, such as food packaging, where low weight, impact absorption, and biodegradability are prioritized. The ability to adjust core density and foam structure provides enhanced protective properties, offering a promising solution for environmentally friendly packaging with improved energy-dissipating capabilities.

Overall, the combination of tailored core densities, controlled mechanical performance, and sustainable material selection demonstrates that PLA foamed-core sandwiches fabricated via FAM are a promising solution for lightweight, energy-dissipating structures. They also provide a benchmark for evaluating novel sandwich configurations in terms of specific energy absorption, confirming their potential for efficient and sustainable design even in applications where high mechanical demands are secondary.

Given the above framework, the main findings presented in this PhD thesis can be summarised as follows:

- The mechanical performance and impact resistance of aluminium honeycomb sandwich structures were characterised, highlighting the influence of core thickness and geometry on energy absorption. The DSF provides a practical tool to predict LVI response from QS tests, supporting efficient design of lightweight, high-performance metallic panels.
- The hybridisation of aluminium honeycomb sandwiches with natural and mineral fibre skins demonstrated that structural performance, stiffness, and energy absorption can be significantly enhanced while maintaining

recyclability and low weight. BFRP skins were shown to maximise strength and impact resistance, offering design strategies for high-performance applications.

- Mono-material PLA sandwich structures produced via Foam Additive Manufacturing demonstrated that tailoring core density enables predictable mechanical performance. The F2 foam configuration provided the most effective combination of stiffness, bending strength, and energy absorption, supporting the development of fully recyclable, lightweight solutions for applications prioritising energy dissipation, such as food protective packaging.

Overall, this thesis demonstrates that advanced sandwich structures, whether metallic, hybrid, or polymer-based, can achieve high mechanical performance while supporting environmental sustainability. The combination of experimental, analytical, and predictive approaches enables informed design of lightweight structures, with potential applications spanning transport, aerospace, and packaging sectors. Future work could extend the experimental investigation to additional hybrid configurations, explore alternative bio-based polymers, and apply innovative manufacturing techniques to further expand the potential of sustainable and lightweight sandwich structures.

Nomenclature

Symbols		Unit of measurement
Latin symbols		
b	Sandwich beam width	mm
d	Distance between the centroid axis of the sandwich skins	mm
D	Sandwich bending stiffness	Nmm^2
E	Young’s modulus	MPa
E_b	Energy spent for bending deformation during impact	J
E_c	Core Young’s modulus	MPa
E_{cn}	Energy spent in contact effect	J
E_f	Skin Young’s modulus	MPa
E_m	Energy spent for membrane deformation during impact	J
E_{sh}	Energy spent for shear deformation during impact	J
E_3	Out-of plane Young’s modulus of the core	MPa
G_c	Core shear modulus	MPa
h	Sandwich overall thickness	mm
I	Area moment of inertia	mm^4
k_b	Bending deflection coefficient	
K_b	Stiffness in the spring-mass model correlated to bending deformation effect	N/m
K_{bs}	Stiffness in the spring-mass model combining *Kb* and *Ks*	
K_c	Stiffness in the spring-mass model correlated to non-linear contact effect	N/m^n

K_m	Stiffness in the spring-mass model correlated to non-linear membrane effect	N/m^3
k_s	Shear deflection coefficient	
K_s	Stiffness in the spring-mass model correlated to shear deformation effect	N/m
m_1	Projectile mass	kg
m_2	Sandwich structure mass	kg
M	Bending moment	Nmm
n	Contract parameter	
N_d	Nozzle diameter	mm
P	Load	N
P_a	Absorption pressure	MPa
R_c	Radius of curvature	mm
s	Core cell size	mm
S	First moment of area	mm^3
S_e	Extrusion speed of the filament	mm/min
t_a	Absorption time	h
t_c	Sandwich core thickness	mm
t_f	Sandwich skin thickness	mm
T_a	Absorption temperature	°C
T_e	Temperature of extrusion	°C
v	Impact velocity	m/s
W	Section modulus	mm^3
w_b	Deflection at impact point	mm
Greek symbols		
α	Indentation depth	mm
δ	Displacement	mm
δ_b	Bending contribute to sandwich beam deflection	mm
δ_s	Shear contribute to sandwich beam deflection	mm
ε_c	Core strain	
ε_f	Skin strain	

ρ	Density	kg/m³
ρ_{rel}	Relative density	kg/m³
σ	Stress	MPa
σ_c	Core stress	MPa
σ_{cc}	Core out-of-plane compressive strength	MPa
σ_f	Skin stress	MPa
$\sigma_{failure}$	Flexural stress at failure	MPa
σ_{fi}	Skin critical in-plane stress for intra-cell dimpling	MPa
σ_{fy}	Yield stress of the sandwich skin	MPa
σ_{fw}	Critical compressive stress for wrinkling	MPa
τ	Shear stress	MPa
τ_{cs}	Core shear strength	MPa
τ_{max}	Maximum shear stress	MPa

Acronyms

AHS	Aluminium honeycomb sandwich
AM	Additive manufacturing
ASTM	American Society for Testing and Materials
BFP	Bottom face perforation
BFRP	Basalt fibre reinforced polymer
BJ	Binder jetting
CAD	Computer aided design
CBA	Chemical blowing agent
CFRP	Carbon fibre reinforced polymer
CT	Computed tomography
CMC	Ceramic-matrix composites
DED	Directed energy deposition
DSF	Dynamic scaling factor
EoL	End-of-life

FAM	Foam additive manufacturing
FDM	Fused deposition modelling
FFRP	Flax fibre reinforced polymer
FRP	Fibre reinforced polymer
GFRP	Glass fibre reinforced polymer
H10	Hemispherical tup with 10 mm diameter
H20	Hemispherical tup with 20 mm diameter
IKE	Incident Kinetic Energy
LCA	Life cycle assessment
ME	Material extrusion
MJ	Material jetting
MMC	Metal-matrix composites
MRI	Magnetic resonance imaging
NP	No perforation
NZE	Net zero emissions
PA	Polyamide
PBF	Powder bed fusion
PET	Polyethylene terephthalate
PLA	Polylactic acid
PMC	Polymer-matrix composites
PP	Polypropylene
PU	Polyurethane
PVC	Polyvinyl chloride
SL	Sheet lamination
STL	Standard triangulation language
TFP	Top face perforation
VP	Vat photopolymerization

8. Bibliography

[1] P. Friedlingstein *et al.*, “Global Carbon Budget 2024,” *Earth Syst Sci Data*, vol. 17, no. 3, pp. 965–1039, Mar. 2025, doi: 10.5194/essd-17-965-2025.

[2] Statista, “Where Do Emissions Come From?” Accessed: Jul. 22, 2025. [Online]. Available: https://www.statista.com/chart/33334/total-greenhouse-gas-emissions-by-sector/

[3] I. Stenius, A. Rosén, and J. Kuttenkeuler, “On structural design of energy efficient small high-speed craft,” *Marine Structures*, vol. 24, no. 1, pp. 43–59, Jan. 2011, doi: 10.1016/j.marstruc.2011.01.001.

[4] G. Palomba, G. Epasto, L. Sutherland, and V. Crupi, “Aluminium honeycomb sandwich as a design alternative for lightweight marine structures,” *Ships and Offshore Structures*, vol. 17, no. 10, pp. 2355–2366, Oct. 2022, doi: 10.1080/17445302.2021.1996109.

[5] S. B. Nagaraju, H. C. Priya, Y. G. T. Girijappa, and M. Puttegowda, “Lightweight and sustainable materials for aerospace applications,” in *Lightweight and Sustainable Composite Materials*, Elsevier, 2023, pp. 157–178. doi: 10.1016/B978-0-323-95189-0.00007-X.

[6] Z. Wawryniuk, E. Brancewicz-Steinmetz, and J. Sawicki, “Revolutionizing transportation: an overview of 3D printing in aviation, automotive, and space industries,” *The International Journal of Advanced Manufacturing Technology*, Sep. 2024, doi: 10.1007/s00170-024-14226-y.

[7] A. J. Timmis *et al.*, “Environmental impact assessment of aviation emission reduction through the implementation of composite materials,” *Int J Life Cycle Assess*, vol. 20, no. 2, pp. 233–243, Feb. 2015, doi: 10.1007/s11367-014-0824-0.

[8] W. D. Callister, *Materials Science and Engineering: An Introduction*, 7th ed. John Wiley & Sons, 2007.

[9] M. A. Ahmad, H. Rafiq, S. I. A. Shah, S. A. Khan, S. T. ul I. Rizvi, and T. A. Shams, “Selection Methodology of Composite Material for Retractable Main Landing Gear Strut of a Lightweight Aircraft,” *Applied Sciences*, vol. 12, no. 11, p. 5689, Jun. 2022, doi: 10.3390/app12115689.

[10] J. R. Duflou, J. De Moor, I. Verpoest, and W. Dewulf, “Environmental impact analysis of composite use in car manufacturing,” *CIRP Annals*, vol. 58, no. 1, pp. 9–12, 2009, doi: 10.1016/j.cirp.2009.03.077.

[11] P. A. Vo Dong, C. Azzaro-Pantel, and A.-L. Cadene, “Economic and environmental assessment of recovery and disposal pathways for CFRP waste management,” *Resour Conserv Recycl*, vol. 133, pp. 63–75, Jun. 2018, doi: 10.1016/j.resconrec.2018.01.024.

[12] E. A. Calado, M. Leite, and A. Silva, “Selecting composite materials considering cost and environmental impact in the early phases of aircraft structure design,” *J Clean Prod*, vol. 186, pp. 113–122, Jun. 2018, doi: 10.1016/j.jclepro.2018.02.048.

[13] D. Rajak, D. Pagar, P. Menezes, and E. Linul, “Fiber-Reinforced Polymer Composites: Manufacturing, Properties, and Applications,” *Polymers (Basel)*, vol. 11, no. 10, p. 1667, Oct. 2019, doi: 10.3390/polym11101667.

[14] B. D. Agarwal and L. J. Broutman, *Analysis and performance of fiber composites*, 2nd ed. John Wiley & Sons, 1990.

[15] V. Crupi, G. Epasto, F. Napolitano, G. Palomba, I. Papa, and P. Russo, “Green Composites for Maritime Engineering: A Review,” *J Mar Sci Eng*, vol. 11, no. 3, p. 599, Mar. 2023, doi: 10.3390/jmse11030599.

[16] A. B. Nair and R. Joseph, “Eco-friendly bio-composites using natural rubber (NR) matrices and natural fiber reinforcements,” in *Chemistry,*

Manufacture and Applications of Natural Rubber, Elsevier, 2014, pp. 249–283. doi: 10.1533/9780857096913.2.249.

[17] F. Rubino, A. Nisticò, F. Tucci, and P. Carlone, "Marine Application of Fiber Reinforced Composites: A Review," *J Mar Sci Eng*, vol. 8, no. 1, p. 26, Jan. 2020, doi: 10.3390/jmse8010026.

[18] L. S. Sutherland, "A review of impact testing on marine composite materials: Part I – Marine impacts on marine composites," *Compos Struct*, vol. 188, pp. 197–208, Mar. 2018, doi: 10.1016/j.compstruct.2017.12.073.

[19] S. V. Joshi, L. T. Drzal, A. K. Mohanty, and S. Arora, "Are natural fiber composites environmentally superior to glass fiber reinforced composites?," *Compos Part A Appl Sci Manuf*, vol. 35, no. 3, pp. 371–376, Mar. 2004, doi: 10.1016/j.compositesa.2003.09.016.

[20] L. J. Gibson and M. F. Ashby, *Cellular Solids*. Cambridge University Press, 1997. doi: 10.1017/CBO9781139878326.

[21] T. Bitzer, "Sandwich design," in *Honeycomb Technology*, Dordrecht: Springer Netherlands, 1997, pp. 43–69. doi: 10.1007/978-94-011-5856-5_3.

[22] J. M. Davies, *Lightweight Sandwich Construction*. John Wiley & Sons, 2008.

[23] D. Zenkert, *The handbook of sandwich construction*. Engineering Materials Advisory Services (EMAS), 1997.

[24] J. R. Vinson, *The Behavior of Sandwich Structures of Isotropic and Composite Materials*. Routledge, 2018. doi: 10.1201/9780203737101.

[25] Y. Zhang, M. Lu, C. H. Wang, G. Sun, and G. Li, "Out-of-plane crashworthiness of bio-inspired self-similar regular hierarchical honeycombs," *Compos Struct*, vol. 144, pp. 1–13, Jun. 2016, doi: 10.1016/j.compstruct.2016.02.014.

[26] A. Krzyżak, M. Mazur, M. Gajewski, K. Drozd, A. Komorek, and P. Przybyłek, "Sandwich Structured Composites for Aeronautics: Methods of Manufacturing Affecting Some Mechanical Properties," *International Journal of Aerospace Engineering*, vol. 2016, pp. 1–10, 2016, doi: 10.1155/2016/7816912.

[27] F. J. Plantema, *Sandwich construction: The bending and buckling of sandwich beams, plates, and shells*. 1966.

[28] H. G. Allen, *Analysis and design of structural sandwich panels*. Elsevier, 1969.

[29] D. Zenkert, *An introduction to sandwich structures*. 1995.

[30] W. J. Cantwell and J. Morton, "The impact resistance of composite materials — a review," *Composites*, vol. 22, no. 5, pp. 347–362, Sep. 1991, doi: 10.1016/0010-4361(91)90549-V.

[31] S. Abrate, *Impact on Composite Structures*. Cambridge University Press, 1998. doi: 10.1017/CBO9780511574504.

[32] K. N. Shivakumar, W. Elber, and W. Illg, "Prediction of Impact Force and Duration Due to Low-Velocity Impact on Circular Composite Laminates," *J Appl Mech*, vol. 52, no. 3, pp. 674–680, Sep. 1985, doi: 10.1115/1.3169120.

[33] A. Petras and M. P. F. Sutcliffe, "Failure mode maps for honeycomb sandwich panels," *Compos Struct*, vol. 44, no. 4, pp. 237–252, Apr. 1999, doi: 10.1016/S0263-8223(98)00123-8.

[34] J. P. Vitale, G. Francucci, J. Xiong, and A. Stocchi, "Failure mode maps of natural and synthetic fiber reinforced composite sandwich panels," *Compos Part A Appl Sci Manuf*, vol. 94, pp. 217–225, Mar. 2017, doi: 10.1016/j.compositesa.2016.12.021.

[35] L. J. Gibson; M. F. Ashby, *Cellular Solids: Structure and Properties*. Cambridge University Press, 1999.

[36] C. A. Steeves and N. A. Fleck, “Collapse mechanisms of sandwich beams with composite faces and a foam core, loaded in three-point bending. Part I: analytical models and minimum weight design,” *Int J Mech Sci*, vol. 46, no. 4, pp. 561–583, Apr. 2004, doi: 10.1016/j.ijmecsci.2004.04.003.

[37] H. G. Allen, *Analysis and Design of Structural Sandwich Panels*. Franklin Book Co, 1969.

[38] A. Mostafa, K. Shankar, and E. V. Morozov, “Insight into the shear behaviour of composite sandwich panels with foam core,” *Mater Des*, vol. 50, pp. 92–101, Sep. 2013, doi: 10.1016/j.matdes.2013.03.016.

[39] M. K. Egbo, “A fundamental review on composite materials and some of their applications in biomedical engineering,” *Journal of King Saud University - Engineering Sciences*, vol. 33, no. 8, pp. 557–568, Dec. 2021, doi: 10.1016/j.jksues.2020.07.007.

[40] W. He *et al.*, “On impact behavior of fiber metal laminate (FML) structures: A state-of-the-art review,” *Thin-Walled Structures*, vol. 167, p. 108026, Oct. 2021, doi: 10.1016/j.tws.2021.108026.

[41] M. K. Faidzi, S. Abdullah, M. F. Abdullah, A. H. Azman, D. Hui, and S. S. K. Singh, “Review of current trends for metal-based sandwich panel: Failure mechanisms and their contribution factors,” *Eng Fail Anal*, vol. 123, p. 105302, May 2021, doi: 10.1016/j.engfailanal.2021.105302.

[42] J. R. Vinson, “Sandwich Structures: Past, Present, and Future,” in *Sandwich Structures 7: Advancing with Sandwich Structures and Materials*, Berlin/Heidelberg: Springer-Verlag, 2005, pp. 3–12. doi: 10.1007/1-4020-3848-8_1.

[43] P. Noury, B. Hayman, D. McGeorge, and J. Weitzenböck, “Lightweight construction for advanced shipbuilding—recent development,” in *Proceedings of the 37th WEGEMT Summer School*, 2002, pp. 11–15.

[44] G. Palomba, G. Epasto, and V. Crupi, "Lightweight sandwich structures for marine applications: a review," *Mechanics of Advanced Materials and Structures*, vol. 29, no. 26, pp. 4839–4864, Oct. 2022, doi: 10.1080/15376494.2021.1941448.

[45] W. Zhang and J. Xu, "Advanced lightweight materials for Automobiles: A review," *Mater Des*, vol. 221, p. 110994, Sep. 2022, doi: 10.1016/j.matdes.2022.110994.

[46] T. Bitzer, *Honeycomb Technology: Materials, Design, Manufacturing, Applications and Testing*. Dordrecht: Springer Netherlands, 1997. doi: 10.1007/978-94-011-5856-5.

[47] A. Elmarakbi, *Advanced composite materials for automotive applications: Structural integrity and crashworthiness*. John Wiley & Sons, 2013.

[48] W. Ma and R. Elkin, *Sandwich Structural Composites*. Boca Raton: CRC Press, 2021. doi: 10.1201/9781003035374.

[49] N. S. Fatima, G. S. Dhaliwal, and G. Newaz, "Influence of interfacial adhesive on impact and post-impact behaviors of CFRP/end-grain balsawood sandwich composites," *Compos B Eng*, vol. 212, p. 108718, May 2021, doi: 10.1016/j.compositesb.2021.108718.

[50] Z. Lu, J. Li, J. Xie, P. Huang, and L. Xue, "Durability of flexurally strengthened RC beams with prestressed CFRP sheet under wet–dry cycling in a chloride-containing environment," *Compos Struct*, vol. 255, p. 112869, Jan. 2021, doi: 10.1016/j.compstruct.2020.112869.

[51] J. P. Nunes and J. F. Silva, "Sandwiched composites in aerospace engineering," in *Advanced Composite Materials for Aerospace Engineering*, Elsevier, 2016, pp. 129–174. doi: 10.1016/B978-0-08-100037-3.00005-5.

[52] L. S. Sutherland and C. Guedes Soares, "The use of quasi-static testing to obtain the low-velocity impact damage resistance of marine GRP

laminates," *Compos B Eng*, vol. 43, no. 3, pp. 1459–1467, Apr. 2012, doi: 10.1016/j.compositesb.2012.01.002.

[53] A. Fam and T. Sharaf, "Flexural performance of sandwich panels comprising polyurethane core and GFRP skins and ribs of various configurations," *Compos Struct*, vol. 92, no. 12, pp. 2927–2935, Nov. 2010, doi: 10.1016/j.compstruct.2010.05.004.

[54] A. Mostafa, K. Shankar, and E. V. Morozov, "Behaviour of PU-foam/glass-fibre composite sandwich panels under flexural static load," *Mater Struct*, vol. 48, no. 5, pp. 1545–1559, May 2015, doi: 10.1617/s11527-014-0253-3.

[55] A. Mostafa, K. Shankar, and E. V. Morozov, "Experimental, Theoretical and Numerical Investigation of the Flexural Behaviour of the Composite Sandwich Panels with PVC Foam Core," *Applied Composite Materials*, vol. 21, no. 4, pp. 661–675, Aug. 2014, doi: 10.1007/s10443-013-9361-4.

[56] A. Russo and B. Zuccarello, "Experimental and numerical evaluation of the mechanical behaviour of GFRP sandwich panels," *Compos Struct*, vol. 81, no. 4, pp. 575–586, Dec. 2007, doi: 10.1016/j.compstruct.2006.10.007.

[57] J. Galos, R. Das, M. P. Sutcliffe, and A. P. Mouritz, "Review of balsa core sandwich composite structures," *Mater Des*, vol. 221, p. 111013, Sep. 2022, doi: 10.1016/j.matdes.2022.111013.

[58] A. D. Almutairi, Y. Bai, and W. Ferdous, "Flexural Behaviour of GFRP-Softwood Sandwich Panels for Prefabricated Building Construction," *Polymers (Basel)*, vol. 15, no. 9, p. 2102, Apr. 2023, doi: 10.3390/polym15092102.

[59] N. Ye *et al.*, "Dynamic response and failure of sandwich plates with PVC foam core subjected to impulsive loading," *Int J Impact Eng*, vol. 109, pp. 121–130, Nov. 2017, doi: 10.1016/j.ijimpeng.2017.06.005.

[60] W. J. Cantwell, G. Broster, and P. Davies, “The Influence of Water Immersion on Skin-Core Debonding in GFRP-Balsa Sandwich Structures,” *Journal of Reinforced Plastics and Composites*, vol. 15, no. 11, pp. 1161–1172, Nov. 1996, doi: 10.1177/073168449601501107.

[61] G. Di Bella, L. Calabrese, and C. Borsellino, “Mechanical characterisation of a glass/polyester sandwich structure for marine applications,” *Mater Des*, vol. 42, pp. 486–494, Dec. 2012, doi: 10.1016/j.matdes.2012.06.023.

[62] H. Fang, H. Sun, W. Liu, L. Wang, Y. Bai, and D. Hui, “Mechanical performance of innovative GFRP-bamboo-wood sandwich beams: Experimental and modelling investigation,” *Compos B Eng*, vol. 79, pp. 182–196, Sep. 2015, doi: 10.1016/j.compositesb.2015.04.035.

[63] A. Gargano, R. Das, and A. P. Mouritz, “Comparative experimental study into the explosive blast response of sandwich structures used in naval ships,” *Composites Communications*, vol. 30, p. 101072, Feb. 2022, doi: 10.1016/j.coco.2022.101072.

[64] T. ; S. L. S. ; G. S. C. Castilho, “Impact resistance of marine sandwich composites,” in *Maritime Technology and Engineering*, 1st Edition., London, UK: Taylor & Francis Group, 2015, pp. 607–618.

[65] M. Garrido, R. Teixeira, J. Correia, and L. Sutherland, “Quasi-static indentation and impact in glass-fibre reinforced polymer sandwich panels for civil and ocean engineering applications,” *Journal of Sandwich Structures & Materials*, vol. 23, no. 1, pp. 194–221, Jan. 2021, doi: 10.1177/1099636219830134.

[66] L. S. Sutherland and C. Guedes Soares, “Impact resistance of cork-skinned marine PVC / GRP sandwich laminates,” *Thin-Walled Structures*, vol. 180, p. 109830, Nov. 2022, doi: 10.1016/j.tws.2022.109830.

[67] A. Djele and R. Karakuzu, “An experimental study on quasi-static indentation, low-velocity impact and damage behaviors of laminated

composites at high temperatures," *Polymers and Polymer Composites*, vol. 29, no. 9_suppl, pp. S969–S977, Nov. 2021, doi: 10.1177/09673911211016932.

[68] L. S. Sutherland, M. F. Sá, J. R. Correia, C. Guedes Soares, A. Gomes, and N. Silvestre, "Impact response of pedestrian bridge multicellular pultruded GFRP deck panels," *Compos Struct*, vol. 171, pp. 473–485, Jul. 2017, doi: 10.1016/j.compstruct.2017.03.052.

[69] S. Abrate, "Impact on Laminated Composite Materials," *Appl Mech Rev*, vol. 44, no. 4, pp. 155–190, Apr. 1991, doi: 10.1115/1.3119500.

[70] S. Abrate, "Localized Impact on Sandwich Structures With Laminated Facings," *Appl Mech Rev*, vol. 50, no. 2, pp. 69–82, Feb. 1997, doi: 10.1115/1.3101689.

[71] H. Guo, H. Yuan, J. Zhang, and D. Ruan, "Review of sandwich structures under impact loadings: Experimental, numerical and theoretical analysis," *Thin-Walled Structures*, vol. 196, p. 111541, Mar. 2024, doi: 10.1016/j.tws.2023.111541.

[72] Q. Ma, M. Rejab, J. Siregar, and Z. Guan, "A review of the recent trends on core structures and impact response of sandwich panels," *J Compos Mater*, vol. 55, no. 18, pp. 2513–2555, Aug. 2021, doi: 10.1177/0021998321990734.

[73] H. Yang, B. C. Ng, H. C. Yu, H. H. Liang, C. C. Kwok, and F. W. Lai, "Mechanical properties study on sandwich hybrid metal/(carbon, glass) fiber reinforcement plastic composite sheet," *Adv Compos Hybrid Mater*, vol. 5, no. 1, pp. 83–90, Mar. 2022, doi: 10.1007/s42114-021-00213-4.

[74] V. Crupi, G. Epasto, and E. Guglielmino, "Comparison of aluminium sandwiches for lightweight ship structures: Honeycomb vs. foam," *Marine Structures*, vol. 30, pp. 74–96, Jan. 2013, doi: 10.1016/j.marstruc.2012.11.002.

[75] G. Palomba, V. Crupi, and G. Epasto, “Collapse modes of aluminium honeycomb sandwich structures under fatigue bending loading,” *Thin-Walled Structures*, vol. 145, p. 106363, Dec. 2019, doi: 10.1016/j.tws.2019.106363.

[76] Y. Zhang, Y. Li, K. Guo, and L. Zhu, “Dynamic mechanical behaviour and energy absorption of aluminium honeycomb sandwich panels under repeated impact loads,” *Ocean Engineering*, vol. 219, p. 108344, Jan. 2021, doi: 10.1016/j.oceaneng.2020.108344.

[77] T. R. Neu, P. H. Kamm, N. von der Eltz, H.-W. Seeliger, J. Banhart, and F. García-Moreno, “Correlation between foam structure and mechanical performance of aluminium foam sandwich panels,” *Materials Science and Engineering: A*, vol. 800, p. 140260, Jan. 2021, doi: 10.1016/j.msea.2020.140260.

[78] J. Xiong, Y. Du, D. Mousanezhad, M. Eydani Asl, J. Norato, and A. Vaziri, “Sandwich Structures with Prismatic and Foam Cores: A Review,” *Adv Eng Mater*, vol. 21, no. 1, Jan. 2019, doi: 10.1002/adem.201800036.

[79] Q. Wu *et al.*, “Mechanical properties and failure mechanisms of sandwich panels with ultra-lightweight three-dimensional hierarchical lattice cores,” *Int J Solids Struct*, vol. 132–133, pp. 171–187, Feb. 2018, doi: 10.1016/j.ijsolstr.2017.09.024.

[80] Y. Feng, H. Qiu, Y. Gao, H. Zheng, and J. Tan, “Creative design for sandwich structures: A review,” *Int J Adv Robot Syst*, vol. 17, no. 3, May 2020, doi: 10.1177/1729881420921327.

[81] B. CASTANIE, C. BOUVET, and M. Ginot, “Review of composite sandwich structure in aeronautic applications,” *Composites Part C: Open Access*, vol. 1, p. 100004, Aug. 2020, doi: 10.1016/j.jcomc.2020.100004.

[82] J. Qi, C. Li, Y. Tie, Y. Zheng, and Y. Duan, “Energy absorption characteristics of origami-inspired honeycomb sandwich structures under

low-velocity impact loading," *Mater Des*, vol. 207, p. 109837, Sep. 2021, doi: 10.1016/j.matdes.2021.109837.

[83] C. Sergi *et al.*, "Experimental and numerical analysis of the ballistic response of agglomerated cork and its bio-based sandwich structures," *Eng Fail Anal*, vol. 131, p. 105904, Jan. 2022, doi: 10.1016/j.engfailanal.2021.105904.

[84] N. S. Fatima, G. S. Dhaliwal, and G. Newaz, "Contribution of adhesive-reinforced interface on the performance of light-weight sustainable sandwich composites," *J Compos Mater*, vol. 56, no. 12, pp. 1829–1849, May 2022, doi: 10.1177/00219983211066643.

[85] L. Ávila de Oliveira, G. L. C. Coura, M. L. PassaiaTonatto, T. H. Panzera, V. Placet, and F. Scarpa, "A novel sandwich panel made of prepreg flax skins and bamboo core," *Composites Part C: Open Access*, vol. 3, p. 100048, Nov. 2020, doi: 10.1016/j.jcomc.2020.100048.

[86] A. Meram and M. E. Çetin, "Experimental Investigation on the Effects of Core/Facing Interface Performance on the Low-Velocity Impact Behavior of Honeycomb Sandwich Panels," *J Mater Eng Perform*, vol. 29, no. 11, pp. 7408–7419, Nov. 2020, doi: 10.1007/s11665-020-05181-2.

[87] J. Liu, W. He, D. Xie, and B. Tao, "The effect of impactor shape on the low-velocity impact behavior of hybrid corrugated core sandwich structures," *Compos B Eng*, vol. 111, pp. 315–331, Feb. 2017, doi: 10.1016/j.compositesb.2016.11.060.

[88] B. Aryal, E. V. Morozov, H. Wang, K. Shankar, P. J. Hazell, and J. P. Escobedo-Diaz, "Effects of impact energy, velocity, and impactor mass on the damage induced in composite laminates and sandwich panels," *Compos Struct*, vol. 226, p. 111284, Oct. 2019, doi: 10.1016/j.compstruct.2019.111284.

[89] Z. Wang, “Recent advances in novel metallic honeycomb structure,” *Compos B Eng*, vol. 166, pp. 731–741, Jun. 2019, doi: 10.1016/j.compositesb.2019.02.011.

[90] M. Abbasi and A. Alavi Nia, “High-velocity impact behavior of sandwich structures with AL faces and foam cores—Experimental and numerical study,” *Aerosp Sci Technol*, vol. 105, p. 106039, Oct. 2020, doi: 10.1016/j.ast.2020.106039.

[91] K. Yuan, L. Shen, W. Xiong, S. Yao, J. He, and Z. Wang, “The impact and post-impact flexural behaviors of CFRP/aluminum-honeycomb sandwich,” *Int J Impact Eng*, vol. 174, p. 104507, Apr. 2023, doi: 10.1016/j.ijimpeng.2023.104507.

[92] W. He, J. Liu, S. Wang, and D. Xie, “Low-velocity impact response and post-impact flexural behaviour of composite sandwich structures with corrugated cores,” *Compos Struct*, vol. 189, pp. 37–53, Apr. 2018, doi: 10.1016/j.compstruct.2018.01.024.

[93] A. Pandey, D. Muchhala, R. Kumar, S. S, A. N. C. Venkat, and D. P. Mondal, “Flexural deformation behavior of carbon fiber reinforced aluminium hybrid foam sandwich structure,” *Compos B Eng*, vol. 183, p. 107729, Feb. 2020, doi: 10.1016/j.compositesb.2019.107729.

[94] Z. Sun, X. Hu, S. Sun, and H. Chen, “Energy-absorption enhancement in carbon-fiber aluminum-foam sandwich structures from short aramid-fiber interfacial reinforcement,” *Compos Sci Technol*, vol. 77, pp. 14–21, Mar. 2013, doi: 10.1016/j.compscitech.2013.01.016.

[95] H. Liu *et al.*, “High-impact resistant hybrid sandwich panel filled with shear thickening fluid,” *Compos Struct*, vol. 284, p. 115208, Mar. 2022, doi: 10.1016/j.compstruct.2022.115208.

[96] W. He, S. Lu, K. Yi, S. Wang, G. Sun, and Z. Hu, “Residual flexural properties of CFRP sandwich structures with aluminum honeycomb cores

after low-velocity impact," *Int J Mech Sci*, vol. 161–162, p. 105026, Oct. 2019, doi: 10.1016/j.ijmecsci.2019.105026.

[97] W. He, J. Liu, S. Wang, and D. Xie, "Low-velocity impact behavior of X-Frame core sandwich structures – Experimental and numerical investigation," *Thin-Walled Structures*, vol. 131, pp. 718–735, Oct. 2018, doi: 10.1016/j.tws.2018.07.042.

[98] Md. Akil Hazizan and W. J. Cantwell, "The low velocity impact response of foam-based sandwich structures," *Compos B Eng*, vol. 33, no. 3, pp. 193–204, Apr. 2002, doi: 10.1016/S1359-8368(02)00009-4.

[99] C. Atas and U. Potoğlu, "The effect of face-sheet thickness on low-velocity impact response of sandwich composites with foam cores," *Journal of Sandwich Structures & Materials*, vol. 18, no. 2, pp. 215–228, Mar. 2016, doi: 10.1177/1099636215613775.

[100] P. M. Schubel, J.-J. Luo, and I. M. Daniel, "Low velocity impact behavior of composite sandwich panels," *Compos Part A Appl Sci Manuf*, vol. 36, no. 10, pp. 1389–1396, Oct. 2005, doi: 10.1016/j.compositesa.2004.11.014.

[101] G. Sun, X. Huo, H. Wang, P. J. Hazell, and Q. Li, "On the structural parameters of honeycomb-core sandwich panels against low-velocity impact," *Compos B Eng*, vol. 216, p. 108881, Jul. 2021, doi: 10.1016/j.compositesb.2021.108881.

[102] J. Liu, W. Chen, H. Hao, and Z. Wang, "Numerical study of low-speed impact response of sandwich panel with tube filled honeycomb core," *Compos Struct*, vol. 220, pp. 736–748, Jul. 2019, doi: 10.1016/j.compstruct.2019.04.023.

[103] J. Liu, Z. Wang, and D. Hui, "Blast resistance and parametric study of sandwich structure consisting of honeycomb core filled with circular

metallic tubes," *Compos B Eng*, vol. 145, pp. 261–269, Jul. 2018, doi: 10.1016/j.compositesb.2018.03.005.

[104] M. Elamin, B. Li, and K. T. Tan, "Compression after impact performance of carbon-fiber foam-core sandwich composites in low temperature arctic conditions," *Compos Struct*, vol. 261, p. 113568, Apr. 2021, doi: 10.1016/j.compstruct.2021.113568.

[105] M. Elamin, B. Li, and K. T. Tan, "Impact damage of composite sandwich structures in arctic condition," *Compos Struct*, vol. 192, pp. 422–433, May 2018, doi: 10.1016/j.compstruct.2018.03.015.

[106] Z. Li, Z. Wang, X. Wang, and W. Zhou, "Bending behavior of sandwich beam with tailored hierarchical honeycomb cores," *Thin-Walled Structures*, vol. 157, p. 107001, Dec. 2020, doi: 10.1016/j.tws.2020.107001.

[107] S. Chahardoli, T. N. Tran, S. M. Hossaeini Marashi, F. Masoumi, and S. Tatyana Yu, "Experimental investigation of the crushing characteristics in sandwich panels in the application of light vehicles using three-point bending tests," *Eng Fail Anal*, vol. 129, p. 105725, Nov. 2021, doi: 10.1016/j.engfailanal.2021.105725.

[108] V. Crupi, E. Kara, G. Epasto, E. Guglielmino, and H. Aykul, "Prediction model for the impact response of glass fibre reinforced aluminium foam sandwiches," *Int J Impact Eng*, vol. 77, pp. 97–107, Mar. 2015, doi: 10.1016/j.ijimpeng.2014.11.012.

[109] V. Crupi, E. Kara, G. Epasto, E. Guglielmino, and H. Aykul, "Theoretical and experimental analysis for the impact response of glass fibre reinforced aluminium honeycomb sandwiches," *Journal of Sandwich Structures & Materials*, vol. 20, no. 1, pp. 42–69, Jan. 2018, doi: 10.1177/1099636216629375.

[110] W. Li, D. Atsushi, Y. H. Oh, S. Jirathearanat, Z. A. Wu, and B. W. Chua, "Influences of skin thickness, core topology, depth and direction on flexural deformation and ductile failure of Al honeycomb-based sandwich structures," *Compos B Eng*, vol. 239, p. 109957, Jun. 2022, doi: 10.1016/j.compositesb.2022.109957.

[111] Z. Wang, Z. Li, and W. Xiong, "Experimental investigation on bending behavior of honeycomb sandwich panel with ceramic tile face-sheet," *Compos B Eng*, vol. 164, pp. 280–286, May 2019, doi: 10.1016/j.compositesb.2018.10.077.

[112] C.-X. Liu, Z.-Y. Fu, P. Li, and G. Qi, "Bending and environmental characteristics of an eco-friendly sandwich panel with cork stopper cores," *Developments in the Built Environment*, vol. 15, p. 100206, Oct. 2023, doi: 10.1016/j.dibe.2023.100206.

[113] P. R. Oliveira, M. May, T. H. Panzera, and S. Hiermaier, "Bio-based/green sandwich structures: A review," *Thin-Walled Structures*, vol. 177, p. 109426, Aug. 2022, doi: 10.1016/j.tws.2022.109426.

[114] ISO/ASTM International, "ISO/ASTM 52900:2021(E): Additive manufacturing — General principles — Fundamentals and vocabulary," 2021.

[115] G. Prashar, H. Vasudev, and D. Bhuddhi, "Additive manufacturing: expanding 3D printing horizon in industry 4.0," *International Journal on Interactive Design and Manufacturing (IJIDeM)*, vol. 17, no. 5, pp. 2221–2235, Oct. 2023, doi: 10.1007/s12008-022-00956-4.

[116] ASTM International, "ASTM F2792 − 12a: Standard Terminology for Additive Manufacturing Technologies," 2012.

[117] T. DebRoy *et al.*, "Additive manufacturing of metallic components – Process, structure and properties," *Prog Mater Sci*, vol. 92, pp. 112–224, Mar. 2018, doi: 10.1016/j.pmatsci.2017.10.001.

[118] W. E. Frazier, “Metal Additive Manufacturing: A Review,” *J Mater Eng Perform*, vol. 23, no. 6, pp. 1917–1928, Jun. 2014, doi: 10.1007/s11665-014-0958-z.

[119] D. Herzog, V. Seyda, E. Wycisk, and C. Emmelmann, “Additive manufacturing of metals,” *Acta Mater*, vol. 117, pp. 371–392, Sep. 2016, doi: 10.1016/j.actamat.2016.07.019.

[120] J. P. M. Pragana, R. F. V. Sampaio, I. M. F. Bragança, C. M. A. Silva, and P. A. F. Martins, “Hybrid metal additive manufacturing: A state–of–the-art review,” *Advances in Industrial and Manufacturing Engineering*, vol. 2, p. 100032, May 2021, doi: 10.1016/j.aime.2021.100032.

[121] T. D. Ngo, A. Kashani, G. Imbalzano, K. T. Q. Nguyen, and D. Hui, “Additive manufacturing (3D printing): A review of materials, methods, applications and challenges,” *Compos B Eng*, vol. 143, pp. 172–196, Jun. 2018, doi: 10.1016/j.compositesb.2018.02.012.

[122] B. Esmaeilian, S. Behdad, and B. Wang, “The evolution and future of manufacturing: A review,” *J Manuf Syst*, vol. 39, pp. 79–100, Apr. 2016, doi: 10.1016/j.jmsy.2016.03.001.

[123] J. Plocher and A. Panesar, “Review on design and structural optimisation in additive manufacturing: Towards next-generation lightweight structures,” *Mater Des*, vol. 183, p. 108164, Dec. 2019, doi: 10.1016/j.matdes.2019.108164.

[124] Y. Li, G. Jia, Y. Cheng, and Y. Hu, “Additive manufacturing technology in spare parts supply chain: a comparative study,” *Int J Prod Res*, vol. 55, no. 5, pp. 1498–1515, Mar. 2017, doi: 10.1080/00207543.2016.1231433.

[125] J. Ni *et al.*, “Three-dimensional printing of metals for biomedical applications,” *Mater Today Bio*, vol. 3, p. 100024, Jun. 2019, doi: 10.1016/j.mtbio.2019.100024.

[126] M. Salmi, “Additive Manufacturing Processes in Medical Applications,” *Materials*, vol. 14, no. 1, p. 191, Jan. 2021, doi: 10.3390/ma14010191.

[127] L. J. Kumar and C. G. Krishnadas Nair, “Current Trends of Additive Manufacturing in the Aerospace Industry,” in *Advances in 3D Printing & Additive Manufacturing Technologies*, Singapore: Springer Singapore, 2017, pp. 39–54. doi: 10.1007/978-981-10-0812-2_4.

[128] O. Sigmund and K. Maute, “Topology optimization approaches,” *Structural and Multidisciplinary Optimization*, vol. 48, no. 6, pp. 1031–1055, Dec. 2013, doi: 10.1007/s00158-013-0978-6.

[129] J.-H. Zhu, W.-H. Zhang, and L. Xia, “Topology Optimization in Aircraft and Aerospace Structures Design,” *Archives of Computational Methods in Engineering*, vol. 23, no. 4, pp. 595–622, Dec. 2016, doi: 10.1007/s11831-015-9151-2.

[130] A. Paolini, S. Kollmannsberger, and E. Rank, “Additive manufacturing in construction: A review on processes, applications, and digital planning methods,” *Addit Manuf*, vol. 30, p. 100894, Dec. 2019, doi: 10.1016/j.addma.2019.100894.

[131] S. Lim, R. A. Buswell, T. T. Le, S. A. Austin, A. G. F. Gibb, and T. Thorpe, “Developments in construction-scale additive manufacturing processes,” *Autom Constr*, vol. 21, pp. 262–268, Jan. 2012, doi: 10.1016/j.autcon.2011.06.010.

[132] D. Delgado Camacho *et al.*, “Applications of additive manufacturing in the construction industry – A forward-looking review,” *Autom Constr*, vol. 89, pp. 110–119, May 2018, doi: 10.1016/j.autcon.2017.12.031.

[133] D. Tammaro *et al.*, “Bio-Lightweight Structures by 3D Foam Printing,” in *2021 IEEE 6th International Forum on Research and Technology for Society and Industry (RTSI)*, IEEE, Sep. 2021, pp. 47–51. doi: 10.1109/RTSI50628.2021.9597272.

[134] L. Landolfi, A. L. H. S. Detry, D. Tammaro, M. M. Villone, L. Maffettone, and A. Squillace, “Additive foam manufacturing,” Oct. 2023, pp. 111–117. doi: 10.21741/9781644902714-14.

[135] D. Cuadra-Rodríguez, S. Barroso-Solares, M. A. Rodríguez-Pérez, and J. Pinto, “Production of cellular polymers without solid outer skins by gas dissolution foaming: A long-sought step towards new applications,” *Mater Des*, vol. 217, p. 110648, May 2022, doi: 10.1016/j.matdes.2022.110648.

[136] I. Gibson, D. Rosen, B. Stucker, and M. Khorasani, *Additive Manufacturing Technologies*. Cham: Springer International Publishing, 2021. doi: 10.1007/978-3-030-56127-7.

[137] M. Nofar, J. Utz, N. Geis, V. Altstädt, and H. Ruckdäschel, “Foam 3D Printing of Thermoplastics: A Symbiosis of Additive Manufacturing and Foaming Technology,” *Advanced Science*, vol. 9, no. 11, Apr. 2022, doi: 10.1002/advs.202105701.

[138] D. M. Wirth, A. Jaquez, S. Gandarilla, J. D. Hochberg, D. C. Church, and J. K. Pokorski, “Highly Expandable Foam for Lithographic 3D Printing,” *ACS Appl Mater Interfaces*, vol. 12, no. 16, pp. 19033–19043, Apr. 2020, doi: 10.1021/acsami.0c02683.

[139] K. M. Lichade and Y. Pan, “Continuous printing of bone-inspired hierarchical porous objects using video projection-based stereolithography,” *J Manuf Process*, vol. 107, pp. 144–154, Dec. 2023, doi: 10.1016/j.jmapro.2023.10.032.

[140] X. Wang *et al.*, “Research progress in polylactic acid processing for 3D printing,” *J Manuf Process*, vol. 112, pp. 161–178, Feb. 2024, doi: 10.1016/j.jmapro.2024.01.038.

[141] G. Niu *et al.*, “Toughening of self-reinforced PLA films using PLA nanofiber mats and oriented PLA tapes as interlayers,” *Compos Part A*

Appl Sci Manuf, vol. 185, p. 108267, Oct. 2024, doi: 10.1016/j.compositesa.2024.108267.

[142] Y. J. Sohn *et al.*, "Recent Advances in Sustainable Plastic Upcycling and Biopolymers," *Biotechnol J*, vol. 15, no. 6, Jun. 2020, doi: 10.1002/biot.201900489.

[143] X.-Y. Yu *et al.*, "Integration Design of Toughening Agent for Poly(lactic acid) with Compatibility, Transparency, and Environmental Friendliness," *ACS Appl Polym Mater*, vol. 6, no. 9, pp. 5555–5565, May 2024, doi: 10.1021/acsapm.4c00836.

[144] T. A. Hottle, M. M. Bilec, and A. E. Landis, "Biopolymer production and end of life comparisons using life cycle assessment," *Resour Conserv Recycl*, vol. 122, pp. 295–306, Jul. 2017, doi: 10.1016/j.resconrec.2017.03.002.

[145] A. Rojas *et al.*, "Foaming with scCO2 and Impregnation with Cinnamaldehyde of PLA Nanocomposites for Food Packaging," *Processes*, vol. 10, no. 2, p. 376, Feb. 2022, doi: 10.3390/pr10020376.

[146] R. Scaffaro, E. F. Gulino, M. C. Citarrella, and A. Maio, "Green Composites Based on Hedysarum coronarium with Outstanding FDM Printability and Mechanical Performance," *Polymers (Basel)*, vol. 14, no. 6, p. 1198, Mar. 2022, doi: 10.3390/polym14061198.

[147] Ahmed. M. Youssef, S. M. El-Sayed, H. S. El-Sayed, H. H. Salama, F. M. Assem, and M. H. Abd El-Salam, "Novel bionanocomposite materials used for packaging skimmed milk acid coagulated cheese (Karish)," *Int J Biol Macromol*, vol. 115, pp. 1002–1011, Aug. 2018, doi: 10.1016/j.ijbiomac.2018.04.165.

[148] N. Bumbudsanpharoke and S. Ko, "Nano-Food Packaging: An Overview of Market, Migration Research, and Safety Regulations," *J Food Sci*, vol. 80, no. 5, May 2015, doi: 10.1111/1750-3841.12861.

[149] A. M. Youssef and Samah. M. El-Sayed, "Bionanocomposites materials for food packaging applications: Concepts and future outlook," *Carbohydr Polym*, vol. 193, pp. 19–27, Aug. 2018, doi: 10.1016/j.carbpol.2018.03.088.

[150] A. Rojas *et al.*, "Supercritical fluid and cocrystallization technologies for designing antimicrobial food packaging PLA nanocomposite foams loaded with eugenol cocrystals with prolonged release," *Chemical Engineering Journal*, vol. 481, p. 148407, Feb. 2024, doi: 10.1016/j.cej.2023.148407.

[151] J. Grünewald, P. Parlevliet, and V. Altstädt, "Manufacturing of thermoplastic composite sandwich structures," *Journal of Thermoplastic Composite Materials*, vol. 30, no. 4, pp. 437–464, Apr. 2017, doi: 10.1177/0892705715604681.

[152] B. ALCOCK, N. CABRERA, N. BARKOULA, and T. PEIJS, "Low velocity impact performance of recyclable all-polypropylene composites," *Compos Sci Technol*, vol. 66, no. 11–12, pp. 1724–1737, Sep. 2006, doi: 10.1016/j.compscitech.2005.11.010.

[153] S. Brischetto and R. Torre, "Honeycomb Sandwich Specimens Made of PLA and Produced Via 3D FDM Printing Process: An Experimental Study," *Journal of Aircraft and Spacecraft Technology*, vol. 4, no. 1, pp. 54–69, Jan. 2020, doi: 10.3844/jastsp.2020.54.69.

[154] G. Palomba, T. Hone, D. Taylor, and V. Crupi, "Bio-inspired protective structures for marine applications," *Bioinspir Biomim*, vol. 15, no. 5, p. 056016, Aug. 2020, doi: 10.1088/1748-3190/aba1d1.

[155] J. Svatík *et al.*, "PLA toughening via bamboo-inspired 3D printed structural design," *Polym Test*, vol. 104, p. 107405, Dec. 2021, doi: 10.1016/j.polymertesting.2021.107405.

[156] J. Yang *et al.*, “Experimental and numerical analysis of bubble nucleation in foaming polymer,” *Mater Des*, vol. 203, p. 109577, May 2021, doi: 10.1016/j.matdes.2021.109577.

[157] L. Zhu, G. Wang, Z. Xu, X. Li, C. Yang, and G. Zhao, “A new microcellular foaming strategy to develop structure-gradient thermoplastic polyurethane foams with enhanced elasticity,” *Mater Des*, vol. 234, p. 112325, Oct. 2023, doi: 10.1016/j.matdes.2023.112325.

[158] M. Rimašauskas, T. Kuncius, and R. Rimašauskienė, “Processing of carbon fiber for 3D printed continuous composite structures,” *Materials and Manufacturing Processes*, vol. 34, no. 13, pp. 1528–1536, Oct. 2019, doi: 10.1080/10426914.2019.1655152.

[159] R. S. Ambekar *et al.*, “Topologically engineered 3D printed architectures with superior mechanical strength,” *Materials Today*, vol. 48, pp. 72–94, Sep. 2021, doi: 10.1016/j.mattod.2021.03.014.

[160] R. Lakes, “Materials with structural hierarchy,” *Nature*, vol. 361, no. 6412, pp. 511–515, Feb. 1993, doi: 10.1038/361511a0.

[161] V. Perricone *et al.*, “Hexagonal Voronoi pattern detected in the microstructural design of the echinoid skeleton,” *J R Soc Interface*, vol. 19, no. 193, Aug. 2022, doi: 10.1098/rsif.2022.0226.

[162] O. Eren, H. K. Sezer, and N. Yalçın, “Effect of lattice design on mechanical response of PolyJet additively manufactured cellular structures,” *J Manuf Process*, vol. 75, pp. 1175–1188, Mar. 2022, doi: 10.1016/j.jmapro.2022.01.063.

[163] K.-M. Park, K.-S. Min, and Y.-S. Roh, “Design Optimization of Lattice Structures under Compression: Study of Unit Cell Types and Cell Arrangements,” *Materials*, vol. 15, no. 1, p. 97, Dec. 2021, doi: 10.3390/ma15010097.

[164] C. W. Visser, D. N. Amato, J. Mueller, and J. A. Lewis, “Architected Polymer Foams via Direct Bubble Writing,” *Advanced Materials*, vol. 31, no. 46, Nov. 2019, doi: 10.1002/adma.201904668.

[165] D. Rizzo, L. S. Sutherland, G. Palomba, and G. Epasto, “Evaluation of Dynamic Scaling Factor by Correlating Quasi-static and Impact Behavior of Sandwich Structures,” *J Mater Eng Perform*, vol. 34, no. 15, pp. 15376–15388, Aug. 2025, doi: 10.1007/s11665-025-11428-7.

[166] N. Kharghani and C. Guedes Soares, “Experimental and numerical study of hybrid steel-FRP balcony overhang of ships under shear and bending,” *Marine Structures*, vol. 60, pp. 15–33, Jul. 2018, doi: 10.1016/j.marstruc.2018.03.003.

[167] “7500-1 I. ISO 7500-1, metallic materials – verification of static uniaxial testing machines – part 1: tension/compression testing machines - verification and calibration of the force-measuring system. 2004”.

[168] D. Rizzo, G. Epasto, A. L. H. S. Detry, L. Landolfi, I. Papa, and A. Squillace, “Mono-material sandwich structures design produced by Foam Additive Manufacturing: study of performances under dynamic conditions,” *Progress in Additive Manufacturing*, Apr. 2025, doi: 10.1007/s40964-025-01057-w.

[169] D. Rizzo, G. Palomba, L. S. Sutherland, and G. Epasto, “Correlation Between Quasi-Static and Impact Behaviour of Sandwich Structures,” 2025, pp. 333–344. doi: 10.1007/978-3-031-77697-7_38.

[170] D. Rizzo, G. Epasto, T. Valente, and P. Russo, “Mechanical behaviour of hybrid FFRP/aluminium honeycomb sandwich structures,” *Eng Fail Anal*, vol. 154, p. 107655, Dec. 2023, doi: 10.1016/j.engfailanal.2023.107655.

[171] F. Ciampa, P. Mahmoodi, F. Pinto, and M. Meo, “Recent Advances in Active Infrared Thermography for Non-Destructive Testing of Aerospace

Components," *Sensors*, vol. 18, no. 2, p. 609, Feb. 2018, doi: 10.3390/s18020609.

[172] V. P. Vavilov and S. S. Pawar, "A novel approach for one-sided thermal nondestructive testing of composites by using infrared thermography," *Polym Test*, vol. 44, pp. 224–233, Jul. 2015, doi: 10.1016/j.polymertesting.2015.04.013.

[173] R. Yang and Y. He, "Optically and non-optically excited thermography for composites: A review," *Infrared Phys Technol*, vol. 75, pp. 26–50, Mar. 2016, doi: 10.1016/j.infrared.2015.12.026.

[174] E. D'Accardi, R. De Finis, G. Dell'Avvocato, G. Masciopinto, D. Palumbo, and U. Galietti, "Conduction thermography for non-destructive assessment of fatigue cracks in metallic materials," *Infrared Phys Technol*, vol. 140, p. 105394, Aug. 2024, doi: 10.1016/j.infrared.2024.105394.

[175] C. Militello, G. Epasto, F. Bongiorno, and B. Zuccarello, "First lamina hybridization of high performance CFRP with Kevlar fibers: Effect on impact behavior and nondestructive evaluation," *Mechanics of Advanced Materials and Structures*, vol. 30, no. 6, pp. 1207–1222, Mar. 2023, doi: 10.1080/15376494.2022.2029639.

[176] I. Papa, E. Manco, G. Epasto, V. Lopresto, and A. Squillace, "Impact behaviour and non destructive evaluation of 3D printed reinforced composites," *Compos Struct*, vol. 281, p. 115112, Feb. 2022, doi: 10.1016/j.compstruct.2021.115112.

[177] Y. Wu, Q. Liu, J. Fu, Q. Li, and D. Hui, "Dynamic crash responses of bio-inspired aluminum honeycomb sandwich structures with CFRP panels," *Compos B Eng*, vol. 121, pp. 122–133, Jul. 2017, doi: 10.1016/j.compositesb.2017.03.030.

[178] S. Liang, L. Guillaumat, and P.-B. Gning, "Impact behaviour of flax/epoxy composite plates," *Int J Impact Eng*, vol. 80, pp. 56–64, Jun. 2015, doi: 10.1016/j.ijimpeng.2015.01.006.

[179] K. R. Ramakrishnan, S. Corn, N. Le Moigne, P. Ienny, and P. Slangen, "Experimental assessment of low velocity impact damage in flax fabrics reinforced biocomposites by coupled high-speed imaging and DIC analysis," *Compos Part A Appl Sci Manuf*, vol. 140, p. 106137, Jan. 2021, doi: 10.1016/j.compositesa.2020.106137.

[180] E. Oterkus, C. Diyaroglu, D. De Meo, and G. Allegri, "Fracture modes, damage tolerance and failure mitigation in marine composites," in *Marine Applications of Advanced Fibre-Reinforced Composites*, Elsevier, 2016, pp. 79–102. doi: 10.1016/B978-1-78242-250-1.00004-1.

[181] D. Gama Caetano, D. Scandiuzzi Valença de Castro, C. Giron Camerini, H. G. Kotik, and A. Alho, "Failure analysis of a CFRP mast of a racing sailboat," *Eng Fail Anal*, vol. 149, p. 107263, Jul. 2023, doi: 10.1016/j.engfailanal.2023.107263.

[182] C. Baley, "Analysis of the flax fibres tensile behaviour and analysis of the tensile stiffness increase," *Compos Part A Appl Sci Manuf*, vol. 33, no. 7, pp. 939–948, Jul. 2002, doi: 10.1016/S1359-835X(02)00040-4.

[183] D. B. Rocha, J. Souza de Carvalho, S. A. de Oliveira, and D. dos Santos Rosa, "A new approach for flexible PBAT/PLA/$CaCO_3$ films into agriculture," *J Appl Polym Sci*, vol. 135, no. 35, Sep. 2018, doi: 10.1002/app.46660.

[184] C. Baley, A. Kervoëlen, A. Le Duigou, C. Goudenhooft, and A. Bourmaud, "Is the low shear modulus of flax fibres an advantage for polymer reinforcement?," *Mater Lett*, vol. 185, pp. 534–536, Dec. 2016, doi: 10.1016/j.matlet.2016.09.067.

[185] H. Zhao, S. Yu, Y. Zhang, and G. Zhao, “Mechanical properties and structure of injection molded poly(hydroxybutyrate-co-hydroxyvalerate)/poly(butylene adipate-co-terephthalate) (<scp>PHBV</scp> / <scp>PBAT</scp>) blends,” *J Appl Polym Sci*, vol. 140, no. 21, Jun. 2023, doi: 10.1002/app.53880.

[186] S. Farah, D. G. Anderson, and R. Langer, “Physical and mechanical properties of PLA, and their functions in widespread applications — A comprehensive review,” *Adv Drug Deliv Rev*, vol. 107, pp. 367–392, Dec. 2016, doi: 10.1016/j.addr.2016.06.012.

[187] G. Palomba, G. Epasto, V. Crupi, and E. Guglielmino, “Single and double-layer honeycomb sandwich panels under impact loading,” *Int J Impact Eng*, vol. 121, pp. 77–90, Nov. 2018, doi: 10.1016/j.ijimpeng.2018.07.013.

[188] A. A. F. Ogaili *et al.*, “The Effect of Chopped Carbon Fibers on the Mechanical Properties and Fracture Toughness of 3D-Printed PLA Parts: An Experimental and Simulation Study,” *Journal of Composites Science*, vol. 8, no. 7, p. 273, Jul. 2024, doi: 10.3390/jcs8070273.

[189] G. Epasto, D. Rizzo, L. Landolfi, A. L. H. S. Detry, I. Papa, and A. Squillace, “Design of monomaterial sandwich structures made with foam additive manufacturing,” *J Manuf Process*, vol. 121, pp. 323–332, Jul. 2024, doi: 10.1016/j.jmapro.2024.05.033.

[190] J. Butt, R. Bhaskar, and V. Mohaghegh, “Analysing the effects of layer heights and line widths on FFF-printed thermoplastics,” *The International Journal of Advanced Manufacturing Technology*, vol. 121, no. 11–12, pp. 7383–7411, Aug. 2022, doi: 10.1007/s00170-022-09810-z.

[191] S. De Rosa, D. Tammaro, and G. D’Avino, “Experimental and Numerical Investigation of the Die Swell in 3D Printing Processes,” *Micromachines (Basel)*, vol. 14, no. 2, p. 329, Jan. 2023, doi: 10.3390/mi14020329.

[192] R. Morgan, R. Reid, A. Baker, B. Lucero, and J. Bernardin, "Emissivity Measurements of Additively Manufactured Materials," Los Alamos, NM (United States), Jan. 2017. doi: 10.2172/1341825.

[193] S. Z. Gebrehiwot, L. Espinosa Leal, J. N. Eickhoff, and L. Rechenberg, "The influence of stiffener geometry on flexural properties of 3D printed polylactic acid (PLA) beams," *Progress in Additive Manufacturing*, vol. 6, no. 1, pp. 71–81, Feb. 2021, doi: 10.1007/s40964-020-00146-2.

[194] V. Santhanakrishnan Balakrishnan, K. Wartig, N. Tsombanis, and H. Seidlitz, "Influence of processing parameters on the impact behaviour of glass/polyamide-6 composite," *Compos B Eng*, vol. 159, pp. 292–299, Feb. 2019, doi: 10.1016/j.compositesb.2018.09.064.

[195] V. Crupi, G. Epasto, and E. Guglielmino, "Internal Damage Investigation of Composites Subjected to Low-Velocity Impact," *Exp Tech*, vol. 40, no. 2, pp. 555–568, Apr. 2016, doi: 10.1007/s40799-016-0057-1.

[196] S. Xie, C. Wang, and W. Deng, "Experimental study on collision acceleration and damage characteristics of potato," *J Food Process Eng*, vol. 43, no. 9, Sep. 2020, doi: 10.1111/jfpe.13457.

[197] N. K. Naik, R. Ramasimha, H. Arya, S. V. Prabhu, and N. ShamaRao, "Impact response and damage tolerance characteristics of glass–carbon/epoxy hybrid composite plates," *Compos B Eng*, vol. 32, no. 7, pp. 565–574, Oct. 2001, doi: 10.1016/S1359-8368(01)00036-1.

[198] Q. Jiang *et al.*, "Sustainable Sandwich Composites Manufactured from Recycled Carbon Fibers, Flax Fibers/PP Skins, and Recycled PET Core," *Journal of Composites Science*, vol. 5, no. 1, p. 2, Dec. 2020, doi: 10.3390/jcs5010002.

[199] P. R. Oliveira *et al.*, "Eco-friendly panels made of autoclaved flax composites and upcycled bottle caps core: experimental and numerical

analysis," *Composites Part C: Open Access*, vol. 4, p. 100114, Mar. 2021, doi: 10.1016/j.jcomc.2021.100114.

[200] N. Ayrilmis, R. Nagarajan, and M. K. Kuzman, "Effects of the Face/Core Layer Ratio on the Mechanical Properties of 3D Printed Wood/Polylactic Acid (PLA) Green Biocomposite Panels with a Gyroid Core," *Polymers (Basel)*, vol. 12, no. 12, p. 2929, Dec. 2020, doi: 10.3390/polym12122929.

[201] Y. Du, N. Yan, and M. T. Kortschot, "Novel lightweight sandwich-structured bio-fiber-reinforced poly(lactic acid) composites," *J Mater Sci*, vol. 49, no. 5, pp. 2018–2026, Mar. 2014, doi: 10.1007/s10853-013-7889-1.

[202] D. Lascano *et al.*, "Manufacturing and Characterization of Highly Environmentally Friendly Sandwich Composites from Polylactide Cores and Flax-Polylactide Faces," *Polymers (Basel)*, vol. 13, no. 3, p. 342, Jan. 2021, doi: 10.3390/polym13030342.

[203] S. Song, C. Xiong, J. Yin, and X. Kang, "Fabrication and mechanical behavior of an all-composite interlocked triangular honeycomb sandwich structure: Experimental investigation and numerical analysis," *Polym Compos*, vol. 44, no. 2, pp. 833–849, Feb. 2023, doi: 10.1002/pc.27135.

[204] B. Kiyak and M. O. Kaman, "Mechanical properties of new-manufactured sandwich composite having carbon fiber core," *J Compos Mater*, vol. 53, no. 22, pp. 3093–3109, Sep. 2019, doi: 10.1177/0021998318810899.

[205] J. Fořt, J. Kočí, and R. Černý, "Environmental Efficiency Aspects of Basalt Fibers Reinforcement in Concrete Mixtures," *Energies (Basel)*, vol. 14, no. 22, p. 7736, Nov. 2021, doi: 10.3390/en14227736.